Alma Mater Studiorum - Università di Bologna

DOTTORATO DI RICERCA IN

IL FUTURO DELLA TERRA, CAMBIAMENTI CLIMATICI E SFIDE SOCIALI

Ciclo 35

Settore Concorsuale: 04/A4 - GEOFISICA

Settore Scientifico Disciplinare: GEO/12 - OCEANOGRAFIA E FISICA DELL'ATMOSFERA

A COUPLED OCEAN-ATMOSPHERE SYSTEM FOR SHORT TERM FORECASTING IN THE SOUTHERN EUROPEAN SEAS

Presentata da: Francesco Maicu

Coordinatore Dottorato

Silvana Di Sabatino

Supervisore

Silvio Gualdi

Co-supervisore

Nadia Pinardi

Emanuela Clementi

Joseph J. Tribbia

Esame finale anno 2023

Acknowledgments

Believe it or not, this is the most exciting part of the thesis I've been eager to write.

The reason is not only that I am at the end of this story, but also that I've the opportunity to wrap up my thoughts and share my joy with the people who helped me in this challenge.

There is no other way than to start by citing the person with whom this story began: Dr. Albert Zirino, who first triggered my curiosity for oceanography and remains a constant reference to this day.

Dr. Georg Umgiesser has supported my growth in the science of mathematical modelling, for which I'd like to thank him.

Prof. Nadia Pinardi has a great responsibility in this story, and I'd like to thank her very much. Her enthusiasm and support pushed me to the topic of coupled models. I have learned a lot from her. You can't imagine how amazed and ashamed at the same time I was, when I realized that this topic originated from the Nobel Prize Syukuro Manabe, the year I was born.

Dr. Silvio Gualdi also gave me this opportunity, thank you very much for that.

I'd like to thank Dr. Francesco Trotta, who was so often a friend and a valuable technical and scientific support, as well as Dr. Emanuela Clementi, Dr. Antonio Navarra, and Dr. Giovanni Liguori, with whom I had interesting scientific discussions.

I cannot forget the time with Dr. Joe Tribbia and the discussions we had while watching the Flatirons and drinking coffee, really a great personal support.

I'm very grateful to my parents for always supporting my decisions, I'm proud of that.

Last but not least Manuela, who always stood by me during this challenge and surrounded me with her love; this work is dedicated to her!

Table of Contents

Index of Figures

Abstract

This thesis shows the development of a regional coupled ocean-atmosphere model for the Southern European Seas, which is realistically expected to become a forecasting system for the short term.

The implemented coupled ocean-atmosphere model considers all air-sea interaction fluxes in different pseudo-empirical formulations and tries to find the most suitable solutions for short- term forecasting. This coupled model combines two state-of-the-art numerical models, NEMO for the oceanic component and WRF for the atmospheric component and implements them at an appropriate resolution.

The oceanic model has been implemented starting from the Mediterranean Forecasting System with a resolution of 1/24° and the domain was extended to exactly match the grid of a newly implemented atmospheric model for the same area. The uncoupled ocean model has been validated against SST observed data, both in the simulation of an extreme event (medicane IANOS) and in the short-term forecast of two seasonal periods. In the coupling perspective, a new setup of the model was successfully tested in which the downward radiative fluxes were prescribed from atmospheric forecasts instead of being computed internally. The prescribed downward longwave radiation was found to be larger than that calculated using the MFS bulk formulae, so its operational use in ocean forecasting should be carefully evaluated.

Various physical schemes, domain, boundary, and initial conditions were tested with the atmospheric model to obtain the best representation of medicane Ianos, compared to ECMWF analyses, remote sensed and observed data. The heat fluxes calculated by the uncoupled models when simulating the medicane were compared to determine which setup gave the best energy balance between the components of the coupled model.

The coupling strategy used is the traditional one, where the ocean is driven by the surface stress, heat fluxes, and radiative fluxes, which are computed in the atmospheric

component with the boundary layer parametrizations, which in turn receives the SST and surface currents.

As expected, the overall skills of the coupled model are slightly degraded compared to the uncoupled models, even though the positioning and timing of the cyclone at the time of the landfall is enhanced.

The SST update in the coupled model does not change the mean heat fluxes compared to the uncoupled model, but it does change the pattern of the two principal components, shortwave radiation and latent heat. Moreover, the two energy fluxes are larger in absolute values than those calculated with the MFS formulas. The fact that they have opposite signs give raise to a compensation error that limits the overall degradation of the coupled simulation. Nevertheless, this problem needs to be further investigated before the coupled prediction system is put into operation, e.g., by changing the coupling strategy with the heat fluxes calculated in the oceanic model.

Introduction

The ocean, with its SST mean state and anomalies, influences atmospheric dynamics in a wide range of spatial and temporal scales. This occurs because it is the main source of energy to the atmosphere, 453 Wm^{-2} according to Trenberth et al. (2009), while the solar radiation contributes only for 78 Wm^{-2}. In turn, atmospheric perturbations are generated, and latent and sensible heat are extracted from the ocean. In a few words, the ocean acts as an energy converter and supplier, so that the atmosphere is mainly heated from the bottom.

The ocean and atmosphere interact by exchanging energy, mass, and momentum. The energy source of Earth system is the solar radiation, which is transformed into fluxes by several processes at the interface.

Over the ocean, the most important of these is evaporation, which first removes latent heat from the ocean (80 Wm^{-2}, Trenberth et al., 2009) and then releases water vapor to the atmosphere. For this reason, it is very important for the energy budget of the ocean.

The temperature difference between the ocean and the atmosphere is another important factor in energy exchange, as it determines the sensible heat flux and the balance between upward and downward thermal radiation (17 Wm^{-2} and 63 Wm^{-2}, respectively, Trenberth et al., 2009).

Finally, the wind, with its relative velocity to the ocean surface, generates shear stresses that transfer momentum downward into the ocean, and enhances evaporation having a major effect on the energy balance via latent heat.

Overall, the ocean has a strong influence on atmospheric dynamics as it stores energy, transports it across the globe, and converts it into different types determining anomalies that lead to weather and climate variability. A comprehensive and

exhaustive review of the major ocean-atmosphere interactions is provided by Miller et al. (2017), along with a critical analysis of the modelling tools that attempt to reproduce such interactions at different temporal and spatial scales.

ENSO is the most relevant coupled ocean-atmosphere interaction that determines the variability of global climate through a variety of teleconnections. Briefly, small perturbations of SST associated with anomalies in wind stress increase in the tropical Pacific and produce a well-defined SST anomaly that is then dissipated by sensible and latent heat, so that it tends to return to its climatological state until the onset of the following perturbed state.

The so-called Pacific Decadal Oscillation (PDO, Mantua et al., 1997) also refers to anomalies in SST that affects the climate of the continental regions around the Northern Pacific. Newman et al. (2016) demonstrated using the Hasselmann (1976) stochastic theory of the climate, that the PDO arises from the continuous integration of random atmospheric perturbations in the ocean. Therefore, PDO itself is a blend of ocean-atmosphere interacting processes, rather than a dynamical variability of the Pacific Ocean.

The Atlantic Meridional Overturning Circulation (AMOC) is another key element of the global thermohaline conveyor belt and thus of the climate system. The AMOC releases large amounts of heat from the tropics into the high latitudes of the North Atlantic, resulting in the formation of the North Atlantic Deep Waters. Delworth and Zeng (2016) demonstrated the impact on the climate change from a possible slowing of the AMOC. The corresponding atmospheric index is the North Atlantic Oscillation (NAO) that is teleconnected with ENSO. NAO-related anomalies of the heat fluxes determine perturbations in the SST, referred to as Atlantic Meridional Oscillations (AMO).

In general, oceanic inertia and heat capacity determine a circulation whose temporal and spatial scales are related to the balance of surface fluxes of mass, heat and momentum rather than to an immediate response to atmospheric weather. There are exceptions however, for example, over the continental shelf and in the turbulent surface layer where the time and space scales are a blend between the atmosphere and the ocean.

The climate variability of the Mediterranean region turns out from the interaction of the large-scale atmospheric variability with the local small-scale of the complex orography and coastline shape. NAO gives rise to decadal and multidecadal variations in precipitation and surface air temperature, mainly by means of modification of the sea level pressure. The Mediterranean Sea converts these atmospheric anomalies into circulation anomalies, which in turn have a feedback on the atmosphere and determine the local weather in the short-term. Mediterranean SST anomalies are known to release heat and moisture into the atmosphere, developing cyclonic features.

Petterssen (1956) first defined the Mediterranean Sea a favourable area for the development of cyclonic storms due to its basin shape, orography, and presence of generally warm ocean waters. The tropical-like characteristics of these cyclones suggested the definition of "Medicane", i.e., Mediterranean hurricane.

The cyclones develop through an intense air-sea interaction, mainly by strong latent heat and convection that redistributes heat and saturated air in the upper layers. An additional positive feedback occurs during the strengthening of the cyclones: the increase of the surface heat fluxes due to the wind intensification (WISHE effect, Emanuel, 1986; Rotunno & Emanuel, 1987). In recent years, several studies have used coupled models to investigate the evolution of Mediterranean cyclones development and to give some perspectives on their future occurrence and intensity: Cavicchia & von Storch, (2012); Cavicchia et al., (2014); (Ricchi et al., 2017, 2019) and Bouin & Lebeaupin Brossier, (2020a, 2020b).

Regional ocean-atmosphere coupled models have also been used in the recent past to assess current climate variability in relation to intense events in the Mediterranean region and to provide insight into future trends: Somot et al., (2008); Artale et al., (2010); Drobinski et al., (2012); Dubois et al., (2012); Gualdi et al., (2013); Sanna et al., (2013); Sevault et al., (2014); Rainaud et al., (2017); Strajnar et al., (2019); Ricchi et al., (2021) and Sauvage et al., (2021).

Another important air-sea interaction occurs in the Mediterranean Sea: the formation dense water in the Gulf of Lion, in the Northern Adriatic Sea, in the North Western Leventine basin and in the Aegean Sea. This process is triggered by the intense and cold atmospheric circulation in winter, which leads to a large loss of heat in the ocean through evaporation, which in turn leads to a loss of upwelling of the surface

water, which sinks. Here is a list of recent papers that have used a coupled modelling approach to this process: Pullen et al., (2003); Loglisci et al., (2004); Pullen et al., (2006, 2007); Brossier and Drobinski, (2009); Carniel et al., (2016); Licer et al., (2016) and Seyfried et al., (2017).

In such a complex area like the one of the Southern European Seas with variable and multiple atmospheric regimes, the surface boundary conditions play an important role in determining the intrinsic predictability of the ocean dynamics in the short term. This constitutes the so called second type predictability (Lorenz, 1975) of the oceanic system, while the first type of predictability is determined by the initial condition, which is also particularly important for the ocean because of its slow evolving dynamics.

Furthermore, the forecasting uncertainty of the atmospheric forcing must be considered along with the uncertainties of the parametrizations of the surface processes at the ocean-atmosphere interface. The goal of coupling the oceanic and atmospheric models is to reduce these uncertainties and exploit the second type predictability to increase the forecast skills of the coupled ocean-atmosphere system.

Literature review of regional coupled models

It is worth to mention that Syukuro Manabe and Kirk Bryan were the pioneers in developing coupled atmospheric and oceanic models. Their first coupled global circulation model is documented in Manabe et al. (1975) and Bryan et al. (1975), where they had the intuition to replace slab ocean models with fully coupled ocean-atmosphere models. This was undoubtedly the most significant step forward in understanding and modelling climate variability, leading the way for the development of comprehensive Earth-system models.

The history of the regional coupled models began in the 1990s with the paper by Hodur, (1997) describing the COAMPS forecasting system (Coupled Ocean Atmosphere Mesoscale Prediction System, from the Naval Research Laboratory of Monterey, CA). The coupled system consisted in a triple model nesting to downscale both components from 45 to 5 km resolution, using data assimilation for the atmospheric component, and provided two daily forecasts for the 1995 America's Cup race held in San Diego

(CA). The evolution of COAMS using the NCOM (Navy Coastal Ocean Model) has been used extensively used in several studies at very high resolution (2-4 km) regarding the onset of Bora events on the Northern Adriatic Sea and the impact of the oceanic circulation (Pullen et al., 2006, 2007).

The Scripps Coupled Ocean Atmosphere Regional Model (SCOAR) was originally developed and published by Seo et al., (2007) and was based on ROMS ocean model (Shchepetkin & McWilliams, 2005) and RSM atmospheric model, which was updated later with the WRF model (Skamarock et al., 2019). Interestingly the system differed from the others since the turbulent heat fluxes are calculated with the oceanic COARE bulk formulae (Fairall et al., 1996). Two relevant applications of SCOAR have been, first, the regional downscaling of a global warming scenario to the tropical Atlantic dynamics (Seo & Xie, 2011) and, second, the analysis of the oceanic eddy-wind interaction in the California Current System (Seo et al., 2016).

The Coupled Ocean–Atmosphere–Wave–Sediment Transport model (COAWST, Warner et al., 2010) added the SWAN wave model (Booij et al., 1999) to WRF and ROMS to reproduce typical coastal processes. It has been successfully used to simulate the effects of multiple hurricanes on coastal ocean dynamics and was shown to improve the trajectories of the hurricanes due to a more precise computation of the diurnal cycle of the surface net heat fluxes (Olabarrieta et al., 2012; Zambon et al., 2014, 2021; Vázquez Proveyer et al., 2022). COAWST has also been used in the Mediterranean to simulate the generation and evolution of intense meteorological events (Ricchi et al., 2017, 2019, 2021).

The European community of oceanographers and meteorologists bases their coupled models on the ocean model NEMO (Madec, 2017) and the OASIS3 coupler (Valcke, 2013) with various atmospheric models. The UK Met Office forecasts are produced by the UKC3 regional coupled environment (H. Lewis et al., 2019), which uses the MetUM atmospheric model (Brown et al., 2012) along with the Wave Watch III model (Tolman et al., 2002).

The coupled model developed at CNRS/Meteo France is based on the AROME (Seity et al., 2011) atmospheric model adapted for the Mediterranean area (AROME-WMED) used in the work of Rainaud et al. (2016, 2017), Lebeaupin Brossier et al. (2017) and Sauvage et al. (2021), with a recent switch to the non-hydrostatic French

research model Meso-NH for the high-resolution simulation of medicanes in Bouin & Lebeaupin Brossier, 2020a, 2020b.

Finally, the regional coupled ocean-atmosphere model NOW is closest to the coupled model developed in this thesis. It was developed by Samson et al. (2015) using NEMO, OASIS and WRF codes and applied in Lengaigne et al. (2019) and Jullien et al. (2020).

Thesis objectives and outline

The main objective of this thesis is to implement a regional coupled ocean-atmosphere model for short-term forecasting of the Southern European Seas (SEAS), which includes the Mediterranean Sea, the Sea of Marmara, and the Black Sea.

Coupling the models does not always improve the forecasts because it introduces feedbacks between the components that may eventually propagate and increase errors in the system as the forecast range increases.

Considering this point, special attention was given in this thesis to understanding the heat fluxes balance in the Mediterranean Sea, since the Mediterranean Sea is an evaporation basin with a slightly negative net heat flux in the range -3 to -7 Wm^{-2} according to the estimates of Pettenuzzo et al., (2010) and Sanchez-Gomez et al., (2011), which is balanced by the net water inflow at the Strait of Gibraltar.

The first step toward the coupled model was to evaluate the performance of the newly developed uncoupled ocean model with prescribed downward radiative fluxes instead of the fluxes calculated with the MFS bulk formulae. This was done both in the simulation of an extreme event such as the medicane Ianos (Ionian Sea, September 15-18, 2020) and in the short-term forecast of two seasonal periods.

The medicane Ianos was also simulated with the uncoupled atmospheric model and the heat fluxes were compared with those calculated with the uncoupled oceanic model.

These two steps made it possible to find the configurations of the oceanic and atmospheric models that best matched in terms of the net heat budget over the Mediterranean Sea. This established the coupling strategy and for the coupled simulation of medicane Ianos.

The thesis is organised as follow.

Chapter 1 contains the description of the oceanic and atmospheric models and the coupling library. The implementation of the SEAS domain is discussed along with the domain, boundary, and initial conditions sensitivity tests.

Chapter 2 shows the results of the uncoupled simulations of oceanic and atmospheric dynamics with seven different setups, along with the discussion of the simulation's skills and the comparison of the heat fluxes.

Chapter 3 shows the validation of the uncoupled ocean model of SEAS with two different radiative forcings along with a discussion of the heat fluxes trends.

Chapter 4. The coupling strategy is presented, and the results of the coupled ocean-atmosphere simulation of medicane Ianos are discussed. The skills of the simulation are discussed, and the heat fluxes are compared with those calculated in the uncoupled atmospheric experiments.

Chapter 5 summarizes the most important results of the thesis and points out the open questions, not fully investigated.

Chapter 1

The Southern European Seas coupled forecasting system

The coupled forecast system for the European Southern Oceans (hereafter SEAS) is based on two general atmospheric and oceanic models that exchange data through a coupling software infrastructure. Given the complexity of the processes resulting from the interaction of the two model components, some simplifications were chosen. No sea ice model is included in the coupled system developed in this work because the study area (Figure 1.1) has an ice-covered sea surface only in the Sea of Azov, which is excluded from our domain. For simplicity, river discharge is not actively coupled with the ocean, but the runoff is prescribed as a surface boundary condition. Finally, surface wind waves are not considered.

The complex shape of the Mediterranean coast, together with the orography of the surrounding areas, can cause local and small-scale atmospheric phenomena such as katabatic winds and sea breezes that affect the ocean circulation and heat exchange of the coastal ocean. These findings led to the design of this coupled system with a unique computational grid and land-sea mask shared by the ocean and atmospheric models, which have the same domain extent and horizontal resolution. This means that no data interpolation with loss of accuracy is required to exchange fields between the atmospheric and oceanic model components. The drawback of this choice is that the size of the domain is mainly determined by the atmospheric flow regimes, so an extended domain of the Atlantic Ocean is needed, including the North Sea. It is well known that the North Atlantic westerly winds dominate the atmospheric variability in winter, and they must be adequately included in the area. The uncoupled ocean system,

called the Mediterranean Forecasting System (Clementi et al., 2021), uses a smaller connection to the Atlantic instead. However, cyclones develop in the southern part of the Mediterranean, so the southern boundary should also be sufficiently large so as not to negatively affect the flow field in the interior. This aspect is discussed in more detail in section 1.2.1.

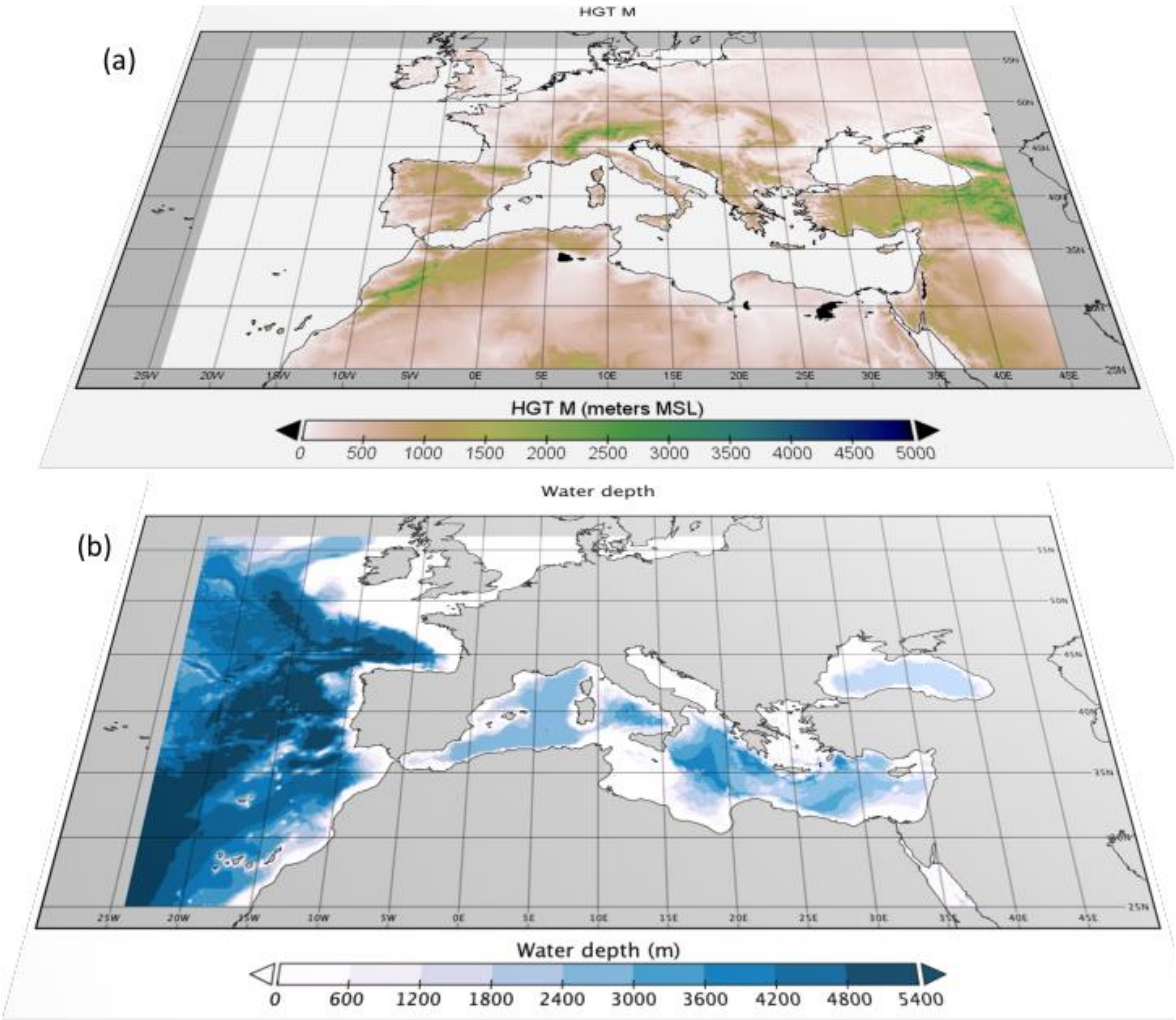

Figure 1.1: orography (a) and bathymetry (b) of the atmospheric and oceanic components of the SEAS coupled forecasting system.

1.1 The model components

1.1.1 The ocean general circulation model

The ocean component is based on the code NEMO (Nucleus for European Modelling of the Ocean, Madec, 2017), developed by the European NEMO Consortium. The code solves the primitive equations for the prognostic variables with nonlinear sea surface height, three dimensional velocities, temperature and salinity, with the incompressible, hydrostatic, and Boussinesq approximations. The variables are solved on a staggered 3D Arakawa-C grid (Arakawa & Lamb, 1977). Horizontally the grid is curvilinear and orthogonal, and vertically, several configurations are available: full or partial z-coordinate, s-coordinate, or a mixture of both. Different physical schemes are available to describe the ocean dynamics, and different bulk formulae are available to calculate the fluxes exchanged with the atmosphere and sea ice.

The implementation of the ocean model benefits from the knowledge of the Mediterranean Forecasting System and relies upon the same physical parametrizations and setup of the so-called version EAS5 (Clementi et al., 2017), as well as on the procedure to generate the lateral and surface boundary conditions. The specific bulk formulation for heat, momentum, and water fluxes implemented in the Mediterranean Sea (Pettenuzzo et al., 2010) has been operative since the beginning of the MFS activity and is described in section 1.1.1.1. A new procedure for generating initial conditions was developed, merging the analyses of the CMEMS Global Ocean Forecasting System (CMEMS-GLO), the Mediterranean Forecasting System (MFS) and the Black Sea Physical Forecast System (BS-PHY NRT).

The preprocessing of the lateral open boundary conditions (LOBC), the surface boundary conditions (SBC) and the model runs, are managed through the SURF platform (Trotta et al., 2016).

The river runoff is prescribed with climatological values: in the Mediterranean MFS considers 39 river inputs (Clementi et al., 2021) and in the Black Sea the forecasting system considers 72 rivers (Ciliberti et al., 2021). They were merged into a new dataset to force the ocean model. No river inputs are considered in the Marmara Sea and along the coastline outside the Gibraltar Strait.

The details of the numerical schemes and constants are summarized in Table 1.1.

Table 1.1: ocean model setup

Item	values
Numerical code	NEMO Version 3.6
Compilation options (keys)	MFS bulk formulae, unstructured open boundary conditions, non-linear free surface with variable volume, time splitting for the free surface, vertical diffusion dependent on the Richardson number
Horizontal grid	Curvilinear orthogonal (lat, lon)
Horizontal resolution	1/24° (2.6-4.2 km)
Vertical grid	$z*$ coordinate with partial step to better adjust to the bottom topography
Vertical resolution (layer depth, m)	141 levels: 1.0, 3.2, 5.5, 7.9, 10.5, 13.3, 16.3, 19.4, 22.7, 26.2, 29.9, 33.8, 37.9, 42.1, 46.7, 51.4, 56.3, 61.5, 66.9, 72.6, 78.6, 84.7, 91.2, 97.9, 104.9, 112.3, 119.9, 127.8, 136.0, 144.5, 153.4, 162.7, 172.2, 182.2, 192.5, 203.2, 214.2, 225.7, 237.6, 249.9, 262.7, 275.8, 289.5, 303.6, 318.1, 333.2, 348.8, 364.8, 381.4, 398.5, 416.2, 434.5, 453.3, 472.7, 492.7, 513.3, 534.5, 556.4, 578.9, 602.1, 626.0, 650.6, 675.9, 701.9, 728.7, 756.2, 784.5, 813.5, 843.4, 874.1, 905.6, 937.9, 971.1, 1005.1, 1040.1, 1075.9, 1112.7, 1150.3, 1189.0, 1228.5, 1269.1, 1310.6, 1353.1, 1396.6, 1441.1, 1486.7, 1533.3, 1580.9, 1629.6, 1679.4, 1730.3, 1782.3, 1835.4, 1889.6, 1944.9, 2001.4, 2059.0, 2117.8, 2177.7, 2238.8, 2301.1, 2364.5, 2429.1, 2494.9, 2561.9, 2630.1, 2699.5, 2770.1, 2841.8, 2914.8, 2989.0, 3064.4, 3141.0, 3218.8, 3297.8, 3378.0, 3459.4, 3541.9, 3625.7, 3710.6, 3796.8, 3884.1, 3972.5, 4062.1, 4152.9, 4244.8, 4337.8, 4432.0, 4527.3, 4623.7, 4721.2, 4819.8, 4919.4, 5020.1, 5121.9, 5224.7, 5328.6, 5433.5, 5539.3, 5646.2, 5754.0
Time step	180 sec ; time step splitting (fraction) for the barotropic terms: 1/100
Lateral Open Boundary Conditions	Flather radiation scheme for the barotropic velocities Orlansky radiation scheme for baroclinic velocities and tracers. No gradient boundary condition for sea level. Relaxation for baroclinic velocities and tracers: 1 grid cell relaxation zone, 1 day damping time scale
Momentum Lateral Boundary	No slip

Condition at sea-land interface	
Bottom Boundary Conditions	Non-linear (quadratic) bottom friction formulation with 1e-05 bottom drag coefficient and 0.0025 (m^2s^{-2}) bottom turbulent kinetic energy background
Surface Boundary Conditions	MFS bulk formulae provide heat fluxes, evaporation and wind stresses Atmospheric fields are taken from ECMWF-IFS HRES 0.1° forecasts and analysis Runoff is specified at 85 river mouths
Momentum Advection	Vector invariant form plus energy and enstrophy conservation scheme
Tracers Advection	Monotone Upstream Scheme for Conservative Laws scheme (MUSCL)
Tracers Diffusion	Bilaplacian operator, horizontal eddy diffusivity -1.2e+08 m^2s^{-1}
Vertical dynamics	Richardson Number dependant (Pacanowski & Philander, 1981) Background eddy viscosity for momentum 1.2e-06 (m^2s^{-1}) Background eddy diffusivity for tracers 1.0e-07 (m^2s^{-1})
Tidal forcing	No

1.1.1.1 The MFS bulk formulae

The air-sea fluxes of heat and mass (evaporation) and wind stresses are computed in the uncoupled version of the ocean model with bulk formulae developed by Pettenuzzo et al., 2010.

The net heat flux at the ocean surface is given by the following balance:

$$Q_t = Q_{SW} + Q_{LW} - Q_H - Q_E \qquad (1\text{-}1)$$

The total heat flux in (1-1) follows the convention of positive (negative) values if heat is gained (lost) by the ocean.

The net downward shortwave solar radiation is calculated from the total clear sky solar radiation Q_{tot} with the astronomical formulae by (Reed 1977) considering the attenuation due to the cloud cover C, the solar zenith angle β (Rosati and Miyakoda

1988) and then furtherly reduced by the monthly values of the monthly varying albedo α (Payne, 1972):

$$Q_{SW} = \left(Q_{tot}(1 - 0.62C + 0.0019\beta)\right)(1 - \alpha) \quad (1\text{-}2)$$

The net longwave terrestrial radiation is given by the difference between the downward longwave radiation emitted by the atmosphere and the upward longwave radiation emitted by the ocean:

$$Q_{LW} = Q_{LWD} - Q_{LWU} \quad (1\text{-}3)$$

The atmosphere emits a longwave radiation according to the Stefan-Boltzmann law for a grey body and here we use the empirical formula of Bignami et al. (1995):

$$Q_{LWD} = [\sigma T_A^4(0.653 + 0.0053\, e_A)](1 + 0.1762C^2) \quad (1\text{-}4)$$

The water vapour pressure e_A is function of the mean sea level pressure and the specific humidity, that in turns is calculated from the 2m dew point temperature with an empirical formula or introduced as input from atmospheric forecasts. Similarly, the ocean surface at temperature SST emits longwave radiation as a black body (ε = 1)

$$Q_{LWU} = \sigma SST^4 \quad (1\text{-}5)$$

The sensible heat flux tends to decrease the temperature difference of the atmosphere T_A and the ocean SST because of heat conduction processes between the two ideal surfaces at a distance approximately 10 m, and is calculated with the following bulk formula:

$$Q_S = \rho_A C_P C_H \left|\vec{V}\right| (T_A - SST) \quad (1\text{-}6)$$

with $\left|\vec{V}\right|$ the wind speed at 10 m, ρ_A the moist air density, C_P the specific heat capacity (1005 cal/kg K) and C_H the turbulent exchange coefficient for the sensible heat.

The latent heat is transferred to the atmosphere through the evaporation of the sea water, and is calculated with the following bulk formula:

$$Q_E = \rho_A L_E C_E \left|\vec{V}\right| (q_A - q_s) \quad (1\text{-}7)$$

The latent heat of vaporization L_E is 2.501·106 J/Kg, q_A and q_S are respectively the specific humidity of the moist air at temperature T_A and saturated at the sea surface temperature, and C_E is the latent heat turbulent exchange coefficient. The evaporation rate is obtained with (1-7) divided by the latent heat of vaporization L_E.

The turbulent exchange coefficients and C_H and C_E are calculated at 10m height as non-linear functions of the wind speed following the Kondo (1975) formulae in case of neutral stability ($T_A = \mathrm{SST}$).

Momentum is transferred to the ocean by the wind stress, which is calculated with the following bulk aerodynamic formula, where the wind is always considered relative to the ocean surficial current:

$$\tau_x = \rho_m C_D \left|\overrightarrow{V_r}\right| U_r \qquad \tau_y = \rho_m C_D \left|\overrightarrow{V_r}\right| V_r \tag{1-8}$$

where ρ_m is the density of the moist air and C_D is the drag coefficient, $\left|\overrightarrow{V_r}\right|$ is the relative wind speed, defined as:

$$\overrightarrow{V_r} = (U_A - U_O, V_A - V_O) \tag{1-9}$$

and $\overrightarrow{\mathrm{V_A}}$ and $\overrightarrow{\mathrm{V_O}}$ are the atmospheric wind at 10 m and surface ocean velocity respectively. The drag coefficient C_D is calculated with the Hellerman & Rosenstein (1983) formula:

$$\mathrm{C_D} = 0.934 \cdot 10^{-3} + 0.788 \cdot 10^{-4} \left|\overrightarrow{V_A}\right| + 0.868 \cdot 10^{-4}\Delta\mathrm{T} +$$

$$-0.616 \cdot 10^{-6}\left|\overrightarrow{V_A}\right|^2 - 0.120 \cdot 10^{-5}\Delta\mathrm{T}^2 - 0.214 \cdot 10^{-5}\left|\overrightarrow{V_A}\right|\Delta\mathrm{T} \tag{1-10}$$

where $\Delta\mathrm{T} = \mathrm{T_A} - \mathrm{SST}$

1.1.2 The atmospheric general circulation model

The atmospheric model is based on the open-source code WRF-ARW (Weather Research and Forecasting model, Skamarock et al., 2019) developed at the National Center for Atmospheric Research (Boulder, CO, U.S.A.).

WRF is a mesoscale numerical weather prediction system designed for both atmospheric research and operational forecasting applications. WRF relies on two dynamical cores, the Advanced Research version of WRF (ARW) and the NCEP Non-hydrostatic Mesoscale Model (NMM), both of which are based on the flux form of the Boussinesq, non-hydrostatic Navier-Stokes equations that resolve advection, viscosity, pressure gradients and Coriolis acceleration. To the dynamical momentum equations, WRF uses the fully compressible continuity and thermodynamic equations with an equation of state for moist air.

The equations are solved using a generalized vertical coordinate scheme that allows the influence of orography on the coordinate surfaces to be removed with increasing height above the surface. This scheme is a hybrid vertical coordinate system, terrain following and hydrostatic pressure ($\sigma - p$), referred to as vertical mass coordinates. It allows a smooth transition from σ coordinates at the ground to hydrostatic pressure p coordinates at the top of the atmosphere, which is typically set at 50 mbars. The spatial discretization follows the Arakawa C grid (Arakawa & Lamb, 1977), which is staggered for the scalar and vectorial variables, and the physical grid changes due to various projections onto the sphere.

The ARW time solver uses a time-split integration scheme. Low-frequency (meteorologically significant) modes are integrated over the model time step using a third-order Runge- Kutta time integration scheme (Wicker & Skamarock, 2002), while the high-frequency acoustic modes are integrated over smaller time steps to maintain numerical stability.

At the land/ocean/atmosphere interface the exchange coefficients for heat, moisture, and momentum are calculated using the Monin-Obukov similarity theory which integrates the empirical stability functions considering the stability regime of the air column. The details of the model developed for the atmospheric component of this coupled system are listed in Table 1.2.

Table 1.2: atmospheric model setup

item	Values
Numerical code	WRF-ARW Version 4.2
Architecture	Distributed and shared memory, INTEL Xeon Phi (MIC architecture)
Horizontal resolution	1/24° (2.6-4.2 km) regular lat-lon projection
Vertical grid	$\sigma - p$ hybrid: terrain following and hydrostatic pressure surfaces
Vertical resolution (layers boundaries, m)	40 levels up to the 50 mbar pressure surface: 0.0, 50.0, 113.9, 195.2, 298.0, 427.2, 587.8, 785.5, 1025.6, 1312.6, 1649.6, 2037.7, 2475.6, 2959.3, 3485.1, 4056.1, 4675, 5344.9, 6068.4, 6841.5, 7598.1, 8338.2, 9061.9, 9769.1, 10459.8, 11134.1, 11791.8, 12433.1, 13057.9, 13678.6,

	14299.3, 14919.9, 15540.6, 16161.3, 16782, 17402.6, 18023.3, 18644, 19264.7, 19885.3
Time step	15 secs
Momentum and scalars advection	5th order in the horizontal, 3rd order in the vertical
Diffusion	2nd order diffusion on coordinate surfaces, PBL scheme in the vertical
Viscosity	Horizontal Smagorinsky 1st order closure scheme
Gravity waves	Additional orographic gravity waves drag scheme
Lateral Open Boundary Conditions	Boundary values on 5 grid cells, specified on 1 grid cell values, relaxed on 4 grid cells
Bottom Boundary Conditions	Prescribed SST
Microphysics	6 classes Thompson scheme (Thompson et al., 2008; Thompson & Eidhammer, 2014)
Cumulus parametrization	Tiedtke scheme (Tiedtke, 1989; Zhang et al., 2011) The scheme is called every time step
Radiative transfer	RRTMG scheme (Iacono et al. 2008) The calculation is performed every 5 mins / 15mins (when coupled)
PBL	• Yonsei University scheme (Hong et al., 2006) • Mellor Yamada Janic scheme, Eta model scheme (Mellor & Yamada, 1982; Janjic, 2001) The scheme is called every time step and passes to the radiation scheme the subgrid-scale clouds
Surface layer	• Revised MM5 similarity theory scheme (Jiménez et al., 2012) • Mellor Yamada Janic scheme, Eta model (Janjic, 2001)
Land surface	Noah Land Surface model (Chen & Dudhia, 2001; Li et al., 2013)
Urban physics	No urban canopy model active
Static datasets	• Topography: GMTED2010 at ≈1km • Land Use: Noah 21-category IGBP-MODIS at ≈0.5km • Soil layers: 16-category soil type at ≈1km • Surface albedo: Monthly MODIS surface albedo at ≈5km • Green fraction: MODIS FPAR monthly green frac. at ≈1km • Leaf area index: MODIS LAI monthly values at ≈20km

1.1.3 The coupling framework

The ocean and atmosphere components exchange variables through the OASIS3-MCT coupling infrastructure (Valcke, 2013; Craig et al., 2017). The OASIS coupler is a software that enables the synchronized exchange of information between numerical codes representing different components of the climate system. The current developers of OASIS are CERFACS (Toulouse, France) and Centre National de la Recherche Scientifique (Paris, France). OASIS3-MCT supports coupling of 2D and 3D fields and 1D fields on both unstructured and structured grids.

The coupling frequency is the time interval at the end of which (the coupling time step) the data exchange between the components occurs. When a model time step is a coupling time step, the model sends the required variables to the coupler and the model component is put on hold until the other model reaches the same coupling time step and sends other required variables to the coupler, which performs the interpolation between the different grids. In our implementation, no interpolation is carried out because the ocean and atmospheric models share the same horizontal grid. The exchanged quantities are represented in Figure 1.2. Typically, it is the atmospheric model that directly exchanges the total heat flux (1-1) with the ocean model, thus using different bulk formulae than the ones calibrated/validated for the Mediterranean Sea over the past 20 years. Coupling 1 is the traditional coupling between ocean and atmosphere used in this thesis, while coupling 2 and 3 are different coupling strategies to be tested in future experiments.

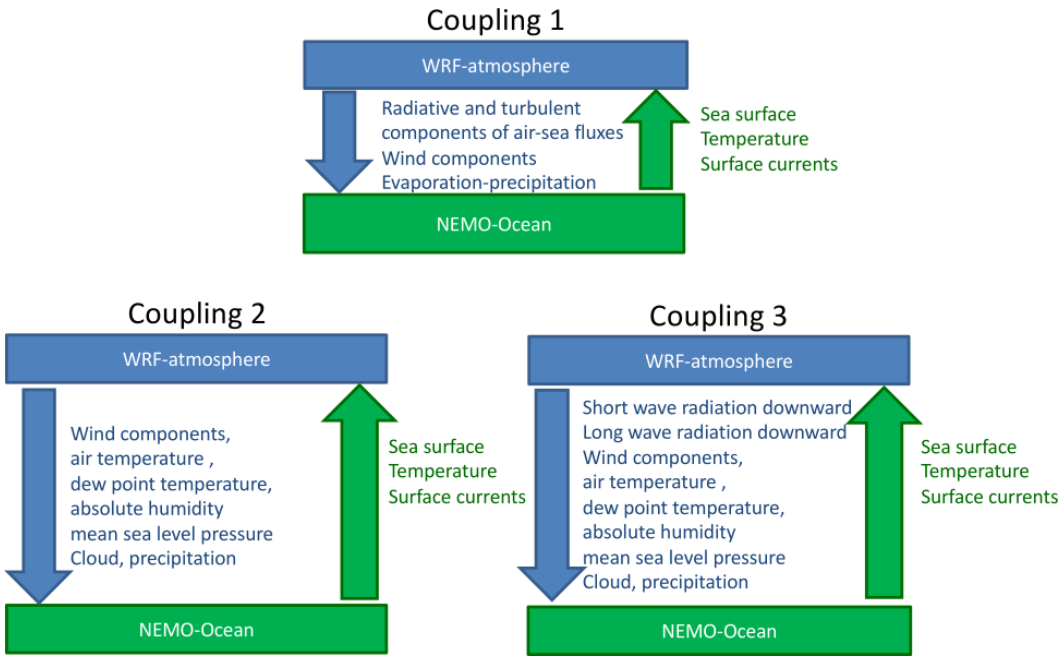

Figure 1.2: Variables exchanged in three different coupling strategies.

1.2 The coupled system domain

Two basic ideas were used in defining the domain of the coupled system.

First, the components must cover the same area. This is necessary to simplify the coupling procedure and avoid merging of the computed fields with external datasets or modeled data with different resolution to fill the non-overlapping areas. This also reduces the sources of uncertainty and error due to mismatched lateral boundary conditions.

Second, the two models must share the same computational grid, i.e., is the same horizontal resolution. The advantage is that no interpolation with loss of accuracy is required for the fields exchanged as shown in Figure 1.2. This approach is proposed in the review paper of Pullen et al. (2017a), which also strongly emphasize the need to use the same land-sea mask. Some recent works using this approach are: Samson et al., (2015); Pullen et al., (2017b); H. Lewis et al., (2019); and Jullien et al., (2020).

The MFS resolution of 1/24° was chosen as the regular latitude and longitude grid for the domain that is shown in Figure 1.1b. The domain includes part of the Eastern Atlantic, the Mediterranean Sea, the Sea of Marmara, and the Black Sea.

The parent models that provide the initial and boundary conditions for the ocean component are CMEMS-GLO (1/12° res.) in the Atlantic Ocean and Sea of Marmara, MFS in the Mediterranean Sea, and the CMEMS Black Sea model. For the atmosphere, the operational analyses of ECMWF (1/10° res.) are used. Therefore, the atmospheric model has the largest ratio of the grid size to the parent model, i.e., 2.4, a value that is acceptable and below the recommendations for a correct transfer of the boundary conditions without relevant damping of atmospheric signals (Skamarock et al., 2019).

The final domain has 1657 x 751 grid points. The nominal resolution of 1/24° corresponds to ≈4.6 km at the equator, and due to the regular lat-lon projection used, the geographic grid resolution varies from ≈4 km at the southern boundary to ≈2.6 km at the northern boundary. This is shown in Figure 1.3, where the MAPFAC_M variable computed by WPS (the WRF preprocessor) is used in the governing equations of the code to scale the distances between the nominal and the geographic.

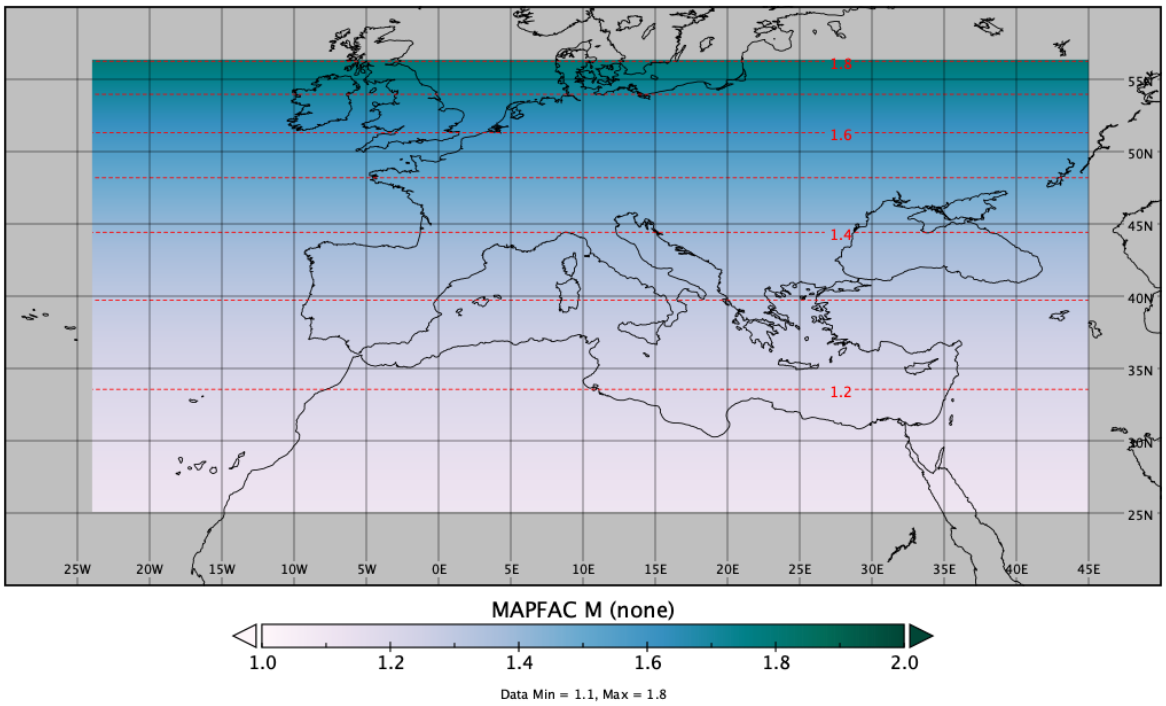

Figure 1.3: map factor M (Δx nominal/ Δx geographical) for the computational grid.

1.2.1 Sensitivity test for the atmospheric component

The positions of the western, northern, and southern boundaries of the domain were determined according to the atmospheric component, considering that the most intense and frequent perturbations develop on the Atlantic Ocean at midlatitudes and then propagate in the Euro-Mediterranean area. For this reason, the western and northern boundaries were set at -24°E and 56.3125°N, where the relevant atmospheric signals can be imposed at the boundaries without relevant orographic structures.

The position of the southern boundary was set after three uncoupled WRF test experiments simulating the Mediterranean cyclone Janos with a downscaling of the ECMWF 1/10° analysis. This intense, tropical-like Mediterranean cyclone developed in the Ionian Sea during the period 15-19 September 2020 and is described in more detail in the next chapter. The first run was the control case, in the second run the model domain was enlarged by moving the boundary southward, and in the third run a different physical parametrization was tested. The physical parametrizations used for the experiments are listed in Table 1.3.

Table 1.3: sensitivity tests for the domain and the physical parametrizations

Experiment name	South. bound. lat.(°N)	Physics parametrizations
Control Experiment 1	25	microphysics: Thomson scheme; radiative fluxes: RRTMG scheme; cumulus parametrization: Tiedtke scheme; surface layer and PBL: MYJ scheme; land surface: Noah model
Experiment 2	29	
Experiment 3	25	microphysics: WSM 6-class scheme; radiative fluxes: RRTMG scheme; no cumulus parametrization; surface layer and PBL: MM5 with additional hurricane parameterization, scheme; land surface: Noah model

The results of the experiments were compared with the ERA5 reanalysis data set, which is considered the best estimate of the real state of the atmosphere. A qualitative comparison of the surface pressure is shown in Figure 1.4 for day 2020-09-18, when the cyclone was near the Ionian Islands of Greece and the pressure reached its minimum in the core of the cyclone. In the control experiment, Figure 1.4b, there is essentially no minimum in surface pressure, while Figure 1.4c shows a deeper local minimum in surface pressure with respect to the control experiment and closer to the value of the reanalysis, although of smaller extent. Interestingly, experiment 3, Figure 1.4d, develops the deepest and wider surface pressure minimum, which is even lower than in the reanalysis. In this case, the physical parametrization of the surface boundary layer recommended for the tropical cyclones (Donelan et al., 2004; Garratt, 1992) was used.

Figure 1.5 shows the qualitative comparison of the scatterometer winds (elaborated in the framework of the HIMIOFOTS project) and the simulated 10m wind fields. In the control experiment 1, the cyclonic wind field is not closed and formed (Figure 1.5b), in the experiment 2 is formed but weaker and smaller compared to the observation (Figure 1.5c). Finally, the experiment 3 with the hurricane parametrization shows the results closest to the observations although with a slightly larger intensity of the wind field and a southern positioning of the eye of the cyclone. The reason of the large intensification of the cyclone lies both in the different surface

layer scheme and in the additional parametrization of the enthalpy exchange coefficient for the hurricanes. Over the water the Garratt formulation increases the thermal and moisture exchange coefficients by relating their typical length scales to the momentum roughness length via the roughness Reynods number. The consequence is an increase of the latent heat extraction from the ocean (Figure 1.6) and the intensification of the cyclone.

Although the experiment 3 performs better than the others, the Garratt parametrization for the enthalpy exchange coefficients is particularly suited for the tropical storms and hurricanes simulation as reported in the WRF Users Guide. The Ianos medicane is a particular test case in the implementation of the SEAS coupled model for a severe event. Keeping in mind the perspective of SEAS to become a coupled forecasting system for the ocean dynamics, we believe that this specific setup cannot be considered in such a standard application in the Mediterranean area, where Cavicchia et al. (2014) demonstrated that the medicanes occurrence is about 1.5 events per year and is not going to increase with the climate change. Experiment 2 seems to provide a reasonable prediction of the cyclone, thus positioning of the southern boundary at the 25°N latitude is an important improvement for defining the coupled model domain.

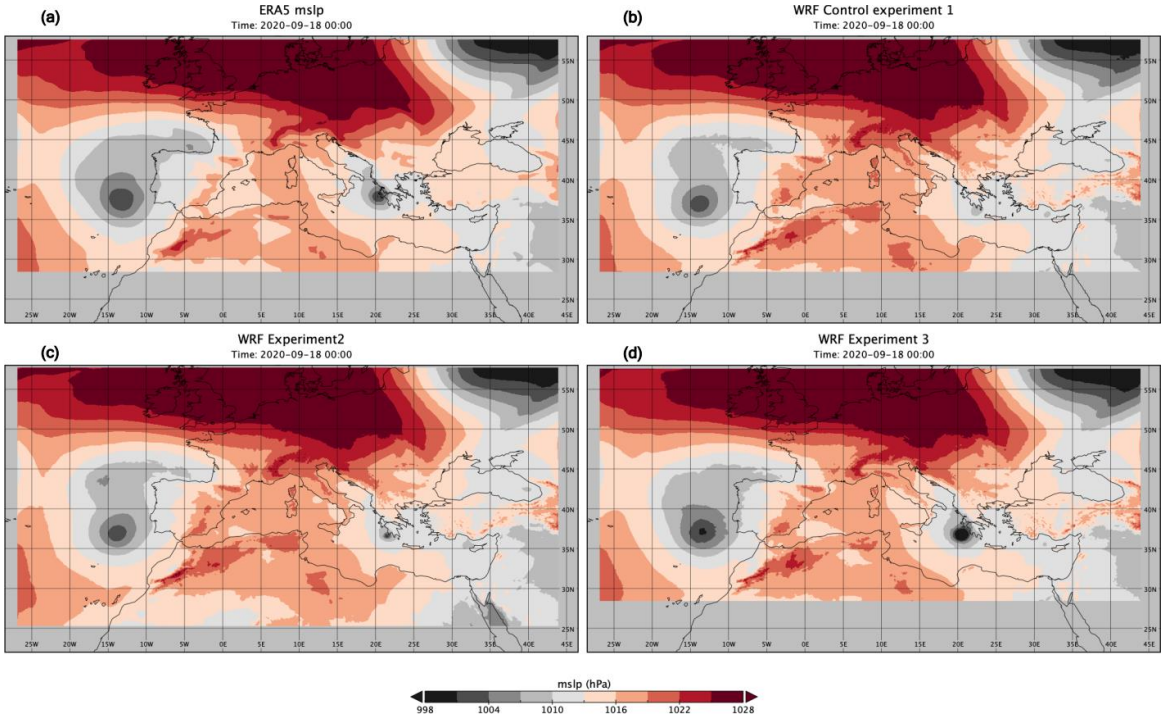

Figure 1.4: mean sea level pressure at the time 2020-09-18 00:00 UTC from ERA5 reanalysis (a) and simulated in the uncoupled atmosphere experiments: control experiment1 (b), experiment2 (c), and experiment3 (d).

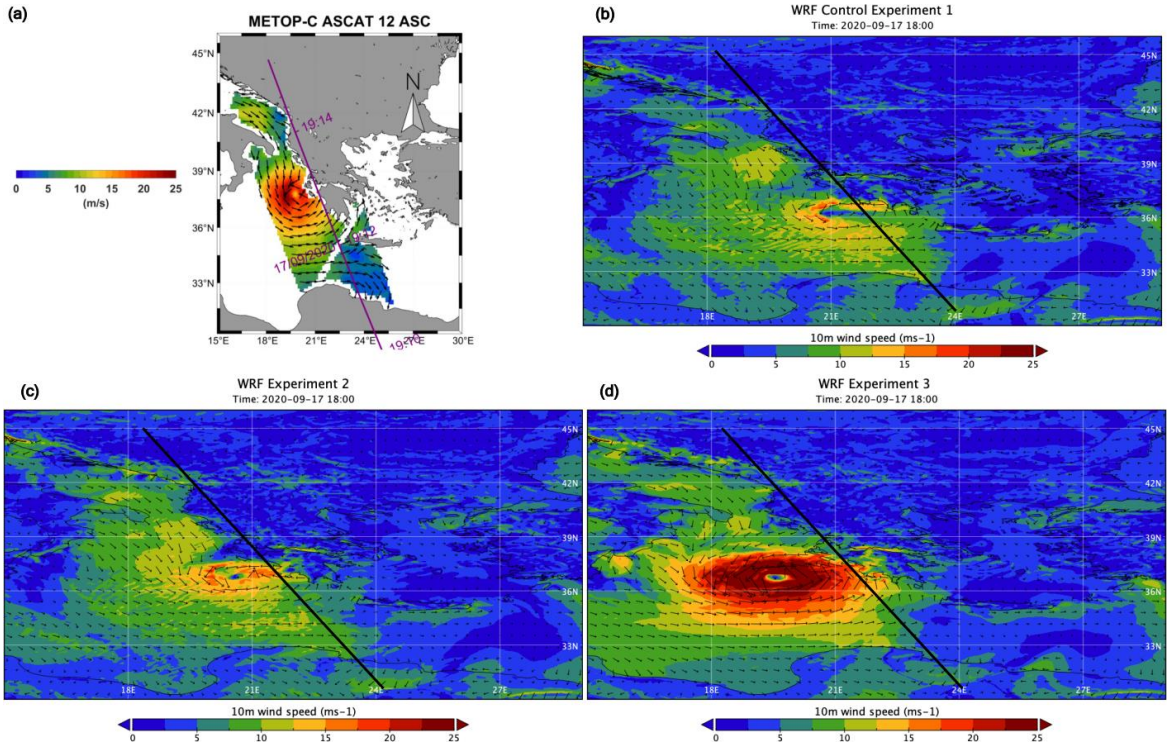

Figure 1.5: surface winds at the time 2020-09-17 19:14 from METOP-C scatterometer (a) and simulated 10m wind field at 2020-09-17 18:00 in the uncoupled atmosphere experiments: control experiment1 (b), experiment2 (c), experiment3 (d). The black lines correspond to the satellite track in (a).

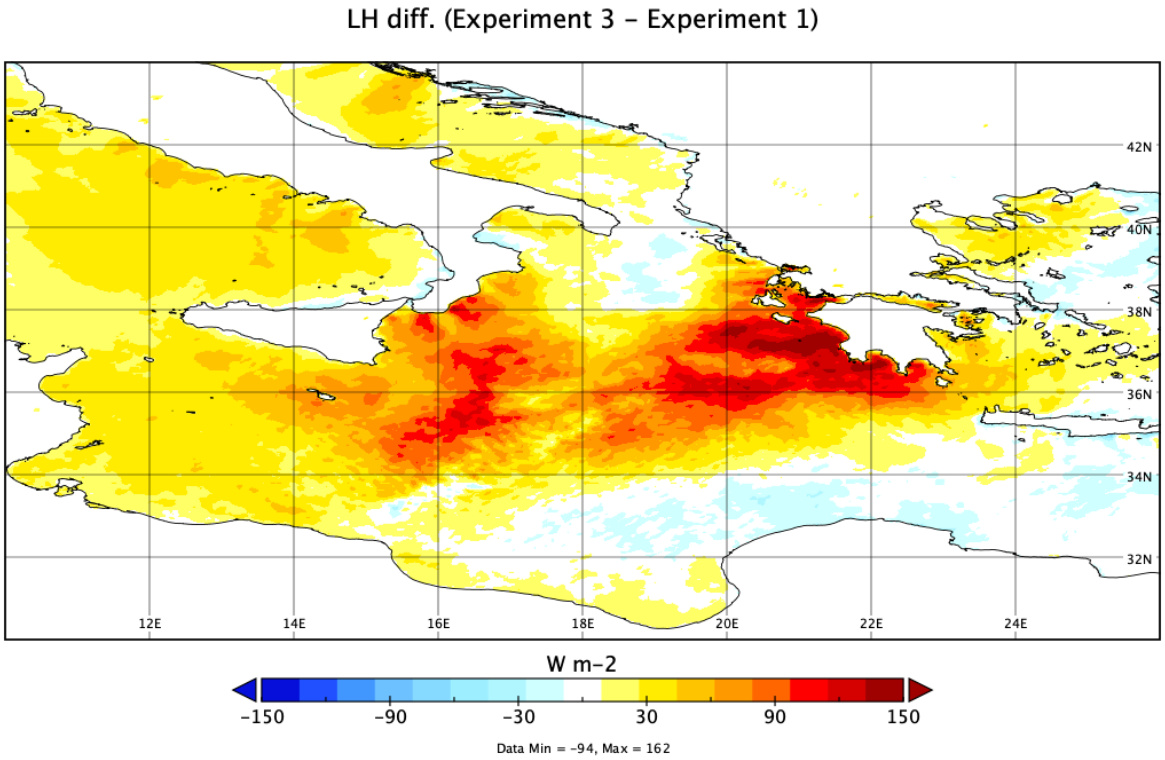

Figure 1.6: Time averaged latent heat difference between Experiment 3 and Experiment1.

1.2.2 Bathymetry blending for the oceanic component

The MFS domain is smaller than the SEAS model domain, thus it is necessary to blend the information from different datasets. In particular, it was used:

- MFS 1/24° regular grid bathymetry;
- Black Sea 1/36° regular grid bathymetry regridded at 1/24°;
- Raw bathymetric data of the Unstructured Turkish Straits System (UTSS, Ilicak et al., 2021) interpolated to the target grid in the Sea of Marmara and Dardanelles Strait;
- GEBCO one-minute arc grid version 2.0 (November 2008) regridded to the target grid in the Atlantic and North Sea.

The last two datasets before the merging were smoothed using a second-order Shapiro filter (Shapiro, 1970). The regridded datasets are then merged with an overlap of 10 grid points, taking a linearly weighted average of the two bathymetric values to avoid abrupt changes in bottom topography (Figure 1.7).

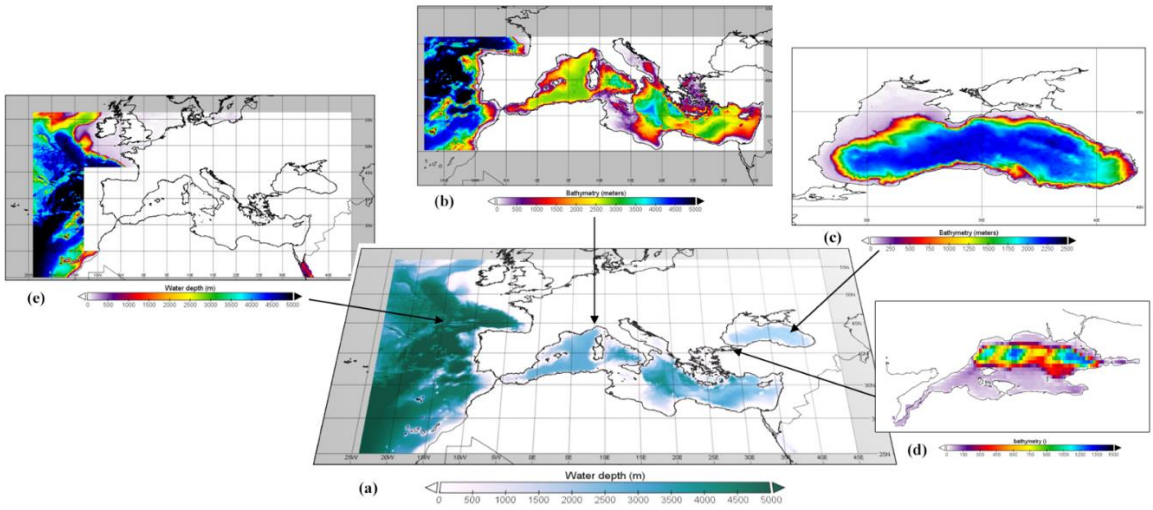

Figure 1.7: (a) final blended bathymetry of the ocean model from MFS bathymetry (b), BS_PHY NRT regridded bathymetry (c), UTSS interpolated bathymetric dataset (d) and GEBCO One regridded dataset (e).

1.3 Initialization

1.3.1 Atmospheric model

WRF requires the following initialization fields:

- Three-dimensional: temperature, wind components, geopotential height, and relative humidity
- Two-dimensional: surface and mean sea level pressure, skin temperature and SST, 2m temperature and relative humidity, 10m wind components, soil moisture and temperature for each available level.

First, a horizontal calculation is performed for each pressure and soil level. Depending on the number of valid source grid points around the target grid point, interpolation is performed sequentially using a sixteen-points overlapping parabolic method, a four-points bilinear method or four-points average method that requires at least one valid source point. Vertical interpolation is then performed from the source pressure levels to the target hybrid $\sigma - p$ vertical coordinates along with the calculation of the reference (hydrostatic component) and perturbed state for the geopotential, potential temperature, dry air mass and density.

The Medicane Janos simulation (15-19 September 2020) is driven and initialized by the six-hourly ECMWF analysis with a resolution of 1/10°. A sensitivity experiment was conducted for the IC to determine which is the best start date for a run to produce a reliable simulation of the Medicane. The control experiment is now the experiment 2 listed in Table 1.3, starting at 2020-09-15 00:00. Now we consider an experiment 2+1d starting at 2020-09-16 00:00 and experiment 2-1d starting at 2020-09-14 00:00. The surface pressure calculated on 2020-09-18 00:00 (+72h simulation for experiment 2, +48h for experiment 2+1d, and +96h for experiment 2-1d) was qualitatively compared with the ERA5 reanalysis.

Figure 1.8c shows that experiment 2-1d is not able to simulate the surface pressure deepening. Figure 1.8d shows that experiment 2+1d calculates a largely deeper minimum of the surface pressure at 48 hours, which is also shifted southward with respect to the best estimates. Experiment 2+1d appears to correctly reproduce the low-pressure area around the cyclone in the Ionian Sea and southern Adriatic. The

Experiment 2 (Figure 1.8b) simulates well the minimum surface pressure and its position after 72 hours, but slightly underestimates the extension of the low-pressure area in the Ionian Sea.

Since this is an explorative work, these experiments do not allow to speculate about the predictability for such extreme events. Regarding the test case of the medicane Ianos the experiments conducted show that 3 days forecast lead time is appropriate for determining a reasonably good forecast for this intense event.

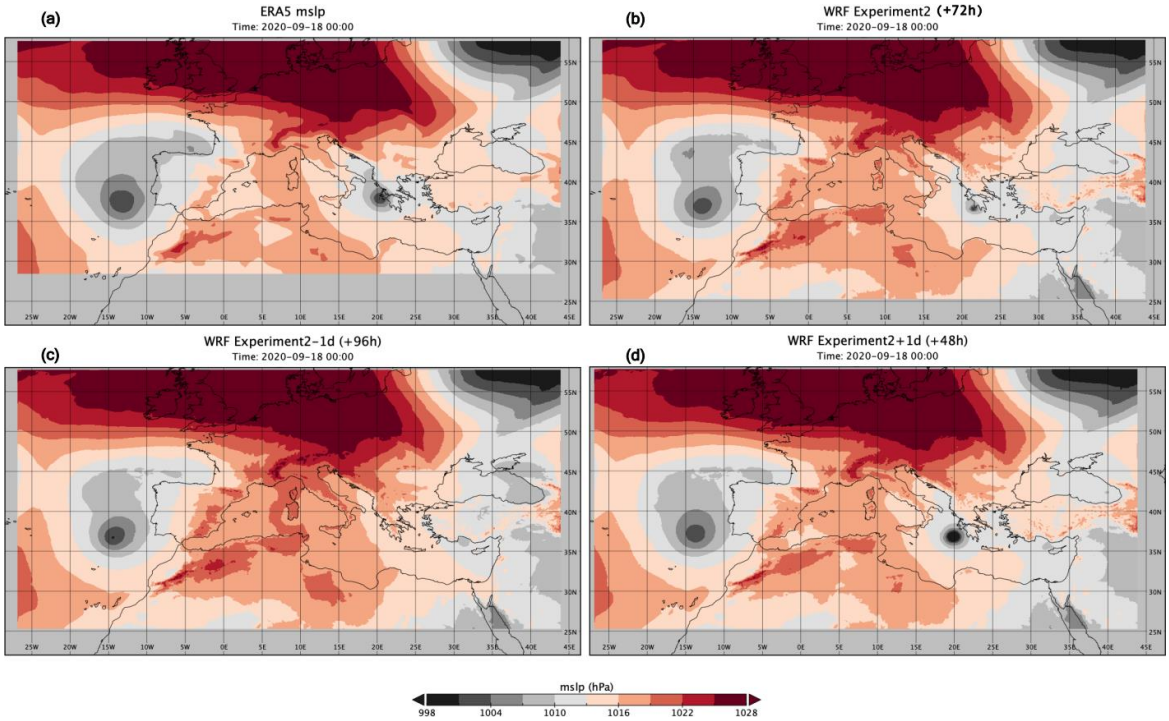

Figure 1.8: Initialization date tests. (a) ERA5 mean sea level pressure field for 2020-09-18 00:00 is taken as reference, and the uncoupled atmosphere experiments are: (b) Experiment2 (control experiment), Experiment 2-1d (c) and Experiment 2+1d (d).

1.3.2 Ocean model

It is well known that the physical processes in the open ocean are driven by the so-called energy cascade (Aluie et al., 2018; Demirov & Pinardi, 2007; Vallis, 2006) which occurs on different temporal and spatial scales, so the structures contained in the initial and lateral boundary conditions are of great importance (von Storch & Zorita, 2019). Two experiments are conducted here, one using initialization fields from CMEMS-GLO

1/12° model interpolated, hereafter referred to as *UO_I_Glo,* and the second using makes use of the high-resolution MFS and Black Sea fields as initial conditions .

The first ocean model experiment was the simulation of the dynamics induced by Medicane Janos in the Ionian Sea during the period 2020-09-15 – 2020-09-19, driven and initialized on day 2020-09-12 by CMEMS-GLO analysis. The half resolution of the parent global ocean model (1/12°) requires an adjustment period, where the model can develop its own dynamical scales from a coarser scale initial condition. This adjustment period has been estimated to be about three days for the Mediterranean Sea in Trotta et al., 2016 and Federico et al., 2017.

We use the SST from the MFS to evaluate the results of the *UO_I_Glo* experiment after three days from initialization. The differences after three days of simulation (Figure 1.9) show that *UO_I_Glo* is warmer in the Atlantic, slightly colder in the western and central Mediterranean, and largely warmer in the Aegean. In the Medicane area, the SST differences range from 1°C - 1.5°C.

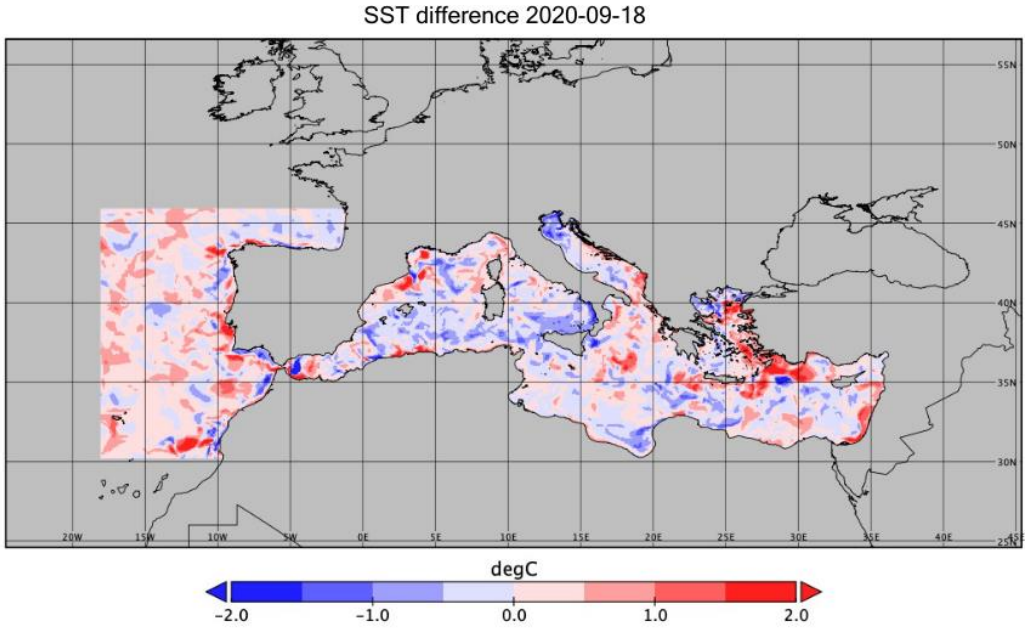

Figure 1.9: SST difference UO_I_Glob – MFS an. For the day 2020-09-18 (+6 days).

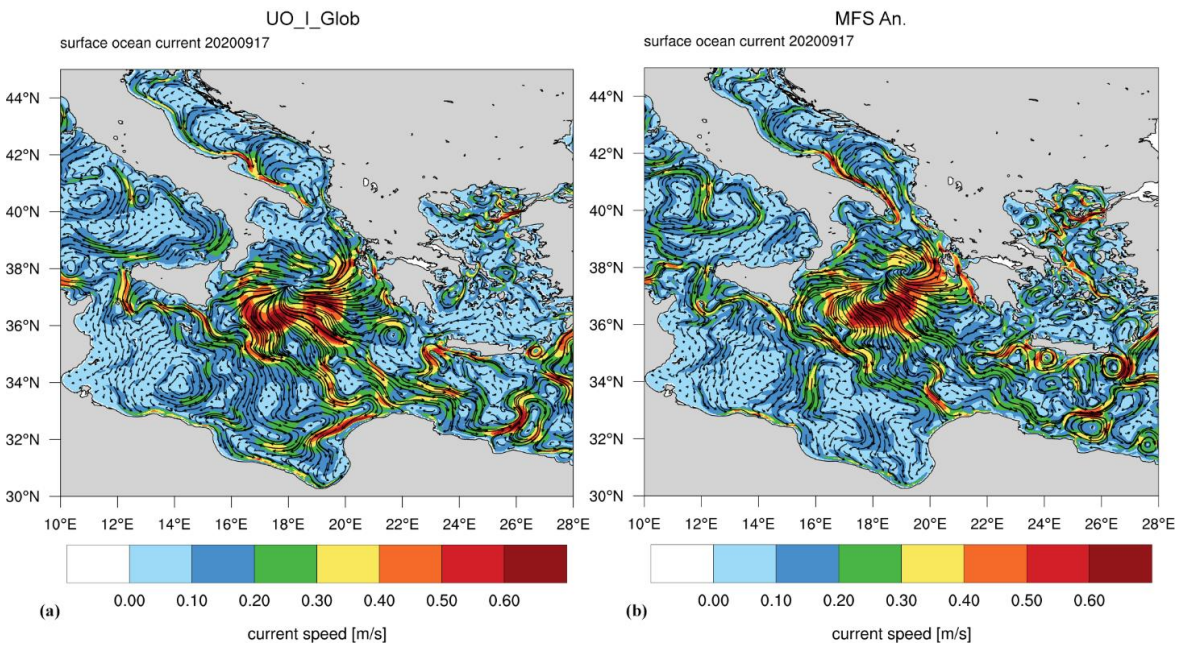

Figure 1.10: ocean surface currents during the day 2020-09-17.

A qualitative difference in the surface currents of day 2020-09-17 is shown in Figure 1.10. The two fields are clearly similar in the Medicane area, being driven mainly by the same intense atmospheric forcing, but may differ significantly in other areas where wind forcing is not as strong (central Tirrenian Sea, Gulf of Sydra, eastern Mediterranean Sea, and Aegean Sea).

The second experiment instead uses the initial conditions of the MFS model and the merging of the Black Sea and CMEMS-GLO and is the definitive configuration for initializing the forecasting system. The same approach of the bathymetric blending described in section 1.2.2, is used with the following datasets:

- MFS Analysis for the Mediterranean Sea and Strait of Gibraltar;
- BS_PHY Analysis at 1/36° regridded at 1/24° on the target grid in the Black Sea and Bosphorus Strait;
- CMEMS-GLO Analysis at 1/12° regridded at 1/24° in the Sea of Marmara and Atlantic Ocean.

The merging of the different datasets is done in the Atlantic side of the Strait of Gibraltar and along the Bosphorus Strait with a linear weighted average of the two datasets along a band of 10 grid points, where the weights are the values between 0 and 1 of each modified land-sea mask (t-point or mass-point mask, Figure 1.11a,b).

Since the Dardanelles Strait is relatively shallow (55 m average depth) and narrow, the merging of the MFS and CMEMS-GLO analysis can be limited to only 5 horizontal grid points.

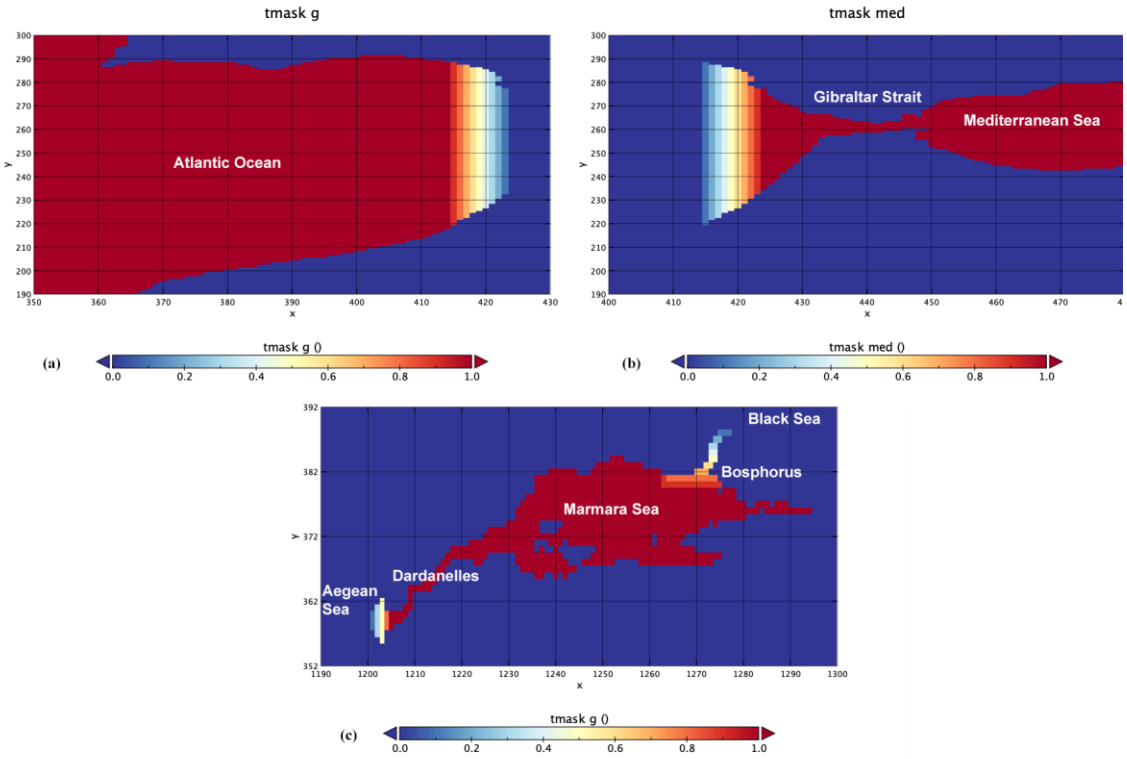

Figure 1.11: Focus of the modified t-point masks for the CMEMS-GLO An. (a) and for the MFS An. (b) used for the merging of the IC at the Gibraltar Strait; same for the CMEMS-GLO An. (c) at the Bosphorus and Dardanelles.

Prior to merging, the regridded CMEMS-GLO and BS_PHY datasets must be vertically interpolated on the 141 levels of the SEAS ocean domain. This procedure generally applies to all scalar fields computed on the *t* grid, such as, temperature, salinity, and SSH. Since U and V are computed on the *u* and *v* staggered grids, the mentioned *t*-point masks cannot be used, hence specific *u* and *v* masks for the three datasets were elaborated to merge the velocity fields.

A problem occurred during the initialization, related to the sea surface height (SSH). Aydoğdu et al. (2018) showed that the climatological average SSH difference between the Black Sea and the Aegean Sea is about 30 cm. The SSH difference of the

day 2020-09-12 is about 70 cm and sea level drops at the Marmara side of the Bosphorus (Figure 1.12). This large, probably unrealistic, drop may be due to the coarse resolution of the global model used to initialize the Sea of Marmara Sea, which unrealistically resolves the Dardanelles and the Bosphorus Straits. It may also be due to the open boundary conditions of the different models. For this reason, the initialization of SEAS SSH is the null field. The results show that the fast propagation of the gravity waves is responsible of the adjustment of the SSH at the level imposed at the Atlantic boundary throughout the Mediterranean basin.

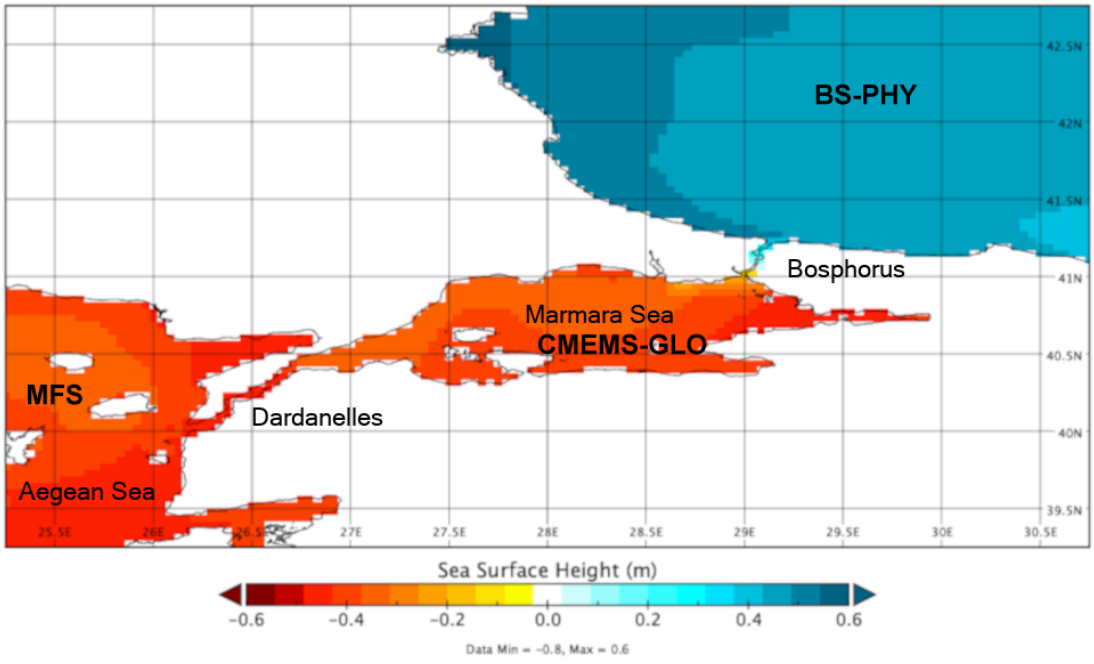

Figure 1.12: merged SSH for the 2020-09-12 and name of the original datasets

Chapter 2

Uncoupled air-sea interaction during an extreme event

The Mediterranean Sea was described by Petterssen (1956) as a favourable area for the development of cyclonic storms because of its basin conformation, orography, and presence of generally warm ocean waters. Cyclones in the Mediterranean Sea have been documented since the early 1980s by Billing et al. (1983) and Ernst & Matson (1983), and thanks to satellite imagery, characteristics similar to those of tropical cyclones have been identified, suggesting the definition of the term "Medicane", i.e. Mediterranean hurricane or tropical cyclone. Their characteristics (Lagouvardos et al., 1999) are a well-defined circular “eye” with a warm core surrounded by spiralling and asymmetrically distributed cloud bands, but with a shorter duration (≈3 days) and smaller dimensions (≈150 km radius) than tropical ones.

An early definition of these phenomena was given by Businger & Reed (1989) as "cold-low type polar lows" on the synoptic scale that occur when cold air masses are advanced over a warm ocean. This means that the cyclone is triggered by a baroclinic instability between an upper deep cold air low and a warm sea and develops through an intense air-sea interaction, mainly by strong latent heat and convection that redistributes heat and saturated air in the upper layers. A common process that strengthens and sustains the cyclone is Wind Intensification Surface Heat Exchange, also known as WISHE (Emanuel, 1986; Rotunno & Emanuel, 1987), a positive feedback between the ocean and atmosphere that counteracts the dissipation of the cyclone that generally occurs with the landfall. In addition to baroclinic triggering, other processes

may be responsible for the development of medicanes, and an appropriate classification was made by Miglietta & Rotunno (2019).

The fact that medicanes develop and spend most of their lifetime at sea poses a potential risk to coastal areas, as they can turn out in destructive landfalls due to the strong winds, heavy rains that lead to storm surges and flooding. It is evident that SST warming in terms of climate change may increase the intensity of such phenomena, while recent works (Cavicchia et al., 2014; Romera et al., 2017; González-Alemán et al., 2019) indicate a decrease in their occurrence.

2.1 The Medicane IANOS

Medicane Janos developed in the Ionian Sea and the eastern Mediterranean between September 15 and 20 2020, and had a strong impact on the Ionian Islands and Thessaly. It caused severe damage in Kefalonia and Zakynthos due to strong winds, storm surges and heavy rains, and in central Greece the torrential precipitations caused severe flooding, landslides and four fatalities. Two detailed descriptions of Ianos are given in the papers of Zimbo et al. (2022) and Lagouvardos et al. (2022).

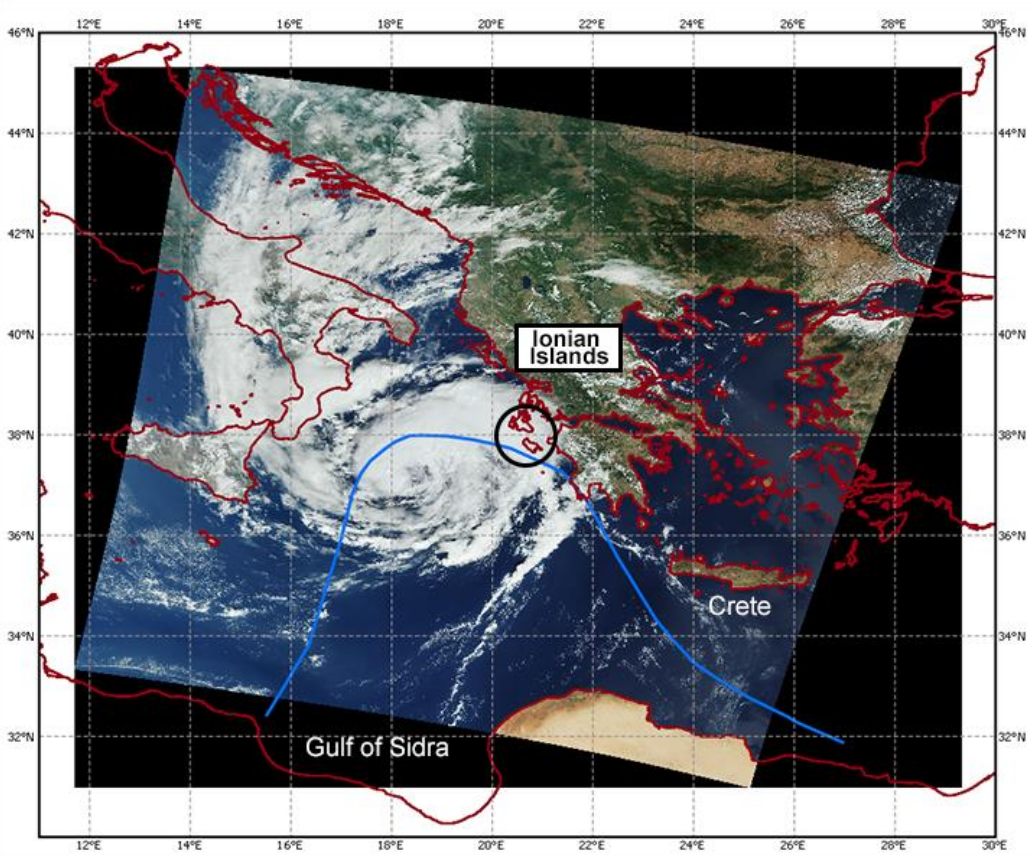

Figure 2.1: Image from Copernicus Sentinel-3 satellite on 2020-09-17 8.48 UTC. Ianos track (light blue line) is derived from Lagouvardos et al. (2022).

Briefly, Ianos initially developed as a surface cyclone near a thunderstorm in the Gulf of Sydra (Figure 2.1) where the cutoff of an upper-level Atlantic flow appeared with a trough of cold air over a warm sea. The associated baroclinic instability triggered

the convective activity and the Medicane developed in the Ionian Sea on 17 September when the surface pressure low and the upper-level trough aligned vertically, and the warm core appeared in the eye of the cyclone. On 18 September, Ianos hit the Ionian Islands with observed low pressure of about 984 hPa, wind gusts up to 55 m/s and a cumulated rainfall of 645 mm. After landfall, Ianos lost intensity and moved southward over warm waters, strengthening again, reaching Crete, and dissipating with the final landfall on the Egyptian coast.

The SST data and its anomaly are retrieved from the Mediterranean Sea High Resolution and Ultra High Resolution Sea Surface Temperature Analysis dataset (, Buongiorno Nardelli et al., 2013), and are shown in Figure 2.2. The SST anomaly is calculated with respect to CNR-ISMAR-GOS daily pentad climatology, built from 21 years of AVHRR Pathfinder data (Product User Manual, https://doi.org/10.48670/moi-00172).

In the early phase of the medicane formation, the SST had the largest values (>28°C) in the Gulf of Sidra (a) with a moderate positive anomaly, while it was relevant (2°-2.5°C) in the Ionian Sea where the Medicane gained intensity in the next days (b). After the transit of this extreme event the SST in the area decreased considerably with values up to 4°C along the path (c), causing the SST anomaly to change to negative values (d). Both Figure 2.2c,d show that the largest changes in SST were restricted to the path itself.

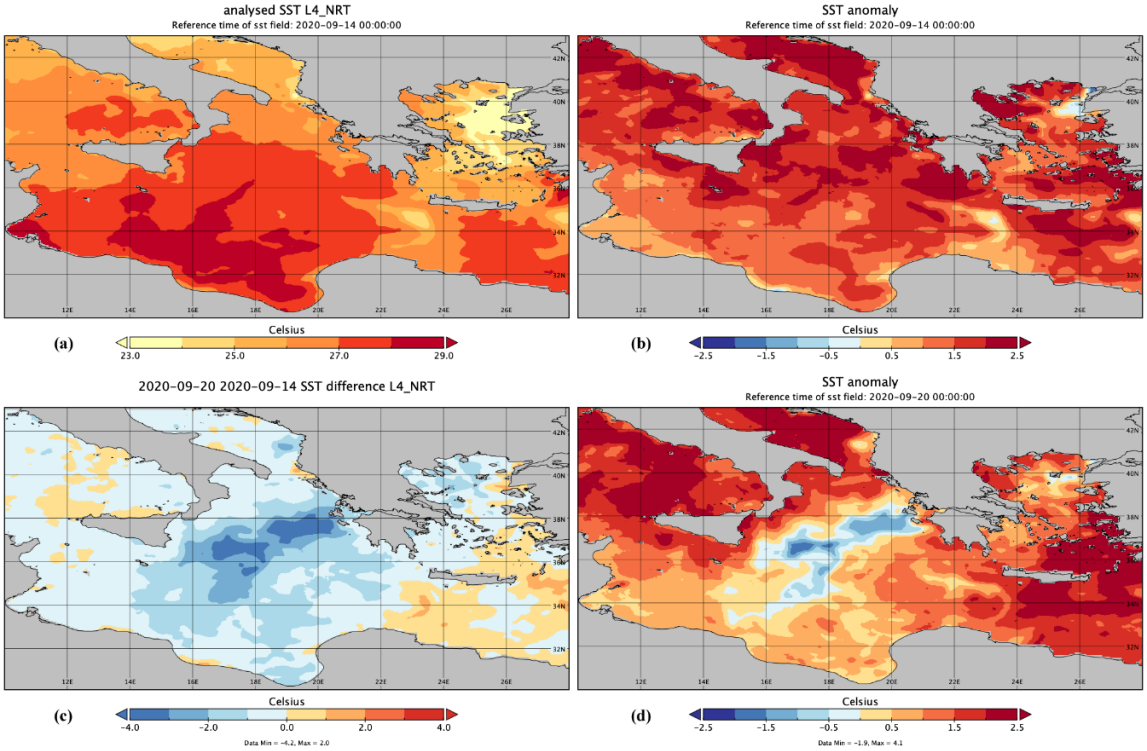

Figure 2.2: 2020-09-14 satellite observed SST (a) and its anomaly (b). 2020-09-20 observed SST difference(c) with respect to (a) and SST anomaly (d).

2.2 Uncoupled experiments

The uncoupled experiments in this chapter are used to calculate the control experiments for ocean and atmosphere, which are compared with the fully coupled experiment in Chapter 4. In addition, various sensitivity tests were performed to determine the uncoupled ocean and atmosphere model configurations that better fit the Ianos observations. This is helpful because full model coupling may introduce unexpected feedbacks among components that degrade the skill with respect to well-consolidated and long-term tested uncoupled air-sea interaction parametrizations.

The atmosphere dynamics during the development of the Medicane Ianos was simulated using the uncoupled model providing the ECMWF-HRES atmospheric analysis fields as initial and boundary conditions along with the remotely sensed and interpolated SST (OSTIA dataset, UKMO, Good et al., 2020). The simulation of the uncoupled ocean model was performed with different radiative flux formulations and with the atmospheric forcing from the uncoupled atmospheric fields.

The names of the experiments are as follows: ***UO*** for *Uncoupled Ocean* and ***as*** air-sea indicates different atmospheric forcings.

2.2.1 Ocean

Table 2.1 summarizes the uncoupled ocean experiments.

Table 2.1: Summary of the uncoupled runs for initial conditions (IC), lateral open boundary conditions (LOBC) and input atmospheric fields for the air-sea physics. The start and end days refer to September 2020.

Run name	IC	LOBC	Input atmospheric data	start day	end day
UO_as1	Merged Analyses MFS+BS+GLO	CMEMS-GLOBAL Analyses	ECMWF Analyses	12	18
UO_as2			ECMWF Analyses + Radiative fluxes		
UO_as3	UO_as1 restart		uncoupled WRF simulation	15	

In detail:

- ***UO_as1***. This is a 7 days-long control simulation for the ocean model, set same as the MFS (Table 1.1). It is initialized the 2020-09-12 with the blended analysis of MFS, BS_PHY and CMEMS-GLO as discussed in section 1.3.2 and laterally forced with daily CMEMS-GLO analyses and 6-hourly ECMWF analyses at 1/10° for the surface input forcing.
- ***UO_as2***. Same as above except that the downward radiative fluxes are prescribed from ECMWF analyses instead of using the MFS bulk formulae reported in section 1.1.1.1 .
- ***UO_as3***. This is a 4 days-long simulation initialized the 2020-09-15 from a restart of *UO_as1*, with atmospheric forcing and downward radiative fluxes (Q_{SW_ua}, Q_{LW_ua}) calculated in *UA_as0_UO* an uncoupled WRF experiment described 2.2.2. The net shortwave and longwave radiative fluxes are calculated in the ocean model as follow:

$$Q_{SW} = Q_{SW\_ua}(1-\alpha) \quad (2\text{-}1)$$

$$Q_{LW} = Q_{LW\_ua} - \varepsilon\sigma SST^4 \quad (2\text{-}2)$$

considering the climatological albedo α values according to Payne (1972) as it is in the MFS bulk formulae, and the emissivity of the ocean of a black body (ε = 1).

The evolution of the remotely sensed SST during the transit of the medicane Ianos has already been presented in Figure 2.2. Therefore, here the results of the three uncoupled experiments are analyzed to speculate how the different setups perform in terms of surface heat balance. Figure 2.3 compares the simulated SST values as time averages for the common period of the three runs (15-18 September 2020) and the relative differences with satellite observations in the central Mediterranean. The footprint of Ianos is visible in its developing area south of Sicily and in the offshore area of the Ionian Islands, where the SST is lower than in the surrounding areas. The pattern of SST is similar in experiments *UO_as1* and *UO_as2* since the experiments have the same atmospheric forcing except for the downward radiative fluxes. The average SST calculated in *UO_as3* (Figure 2.3c) is close to *UO_as1* by ±0.2 °C, except for the Ianos area. This time, as expected, the higher resolution of the atmospheric WRF model makes a difference.

In the central Mediterranean, the three experiments show an overall positive BIAS with the largest differences in the range between 1 and to 1.5 °C. The *UO_as3* experiment shows a BIAS which is slightly warmer than the other experiments. Apart from the model error, these differences could be due to a lower SST estimated with the postprocessing algorithm for the remote sensed data under the clouds.

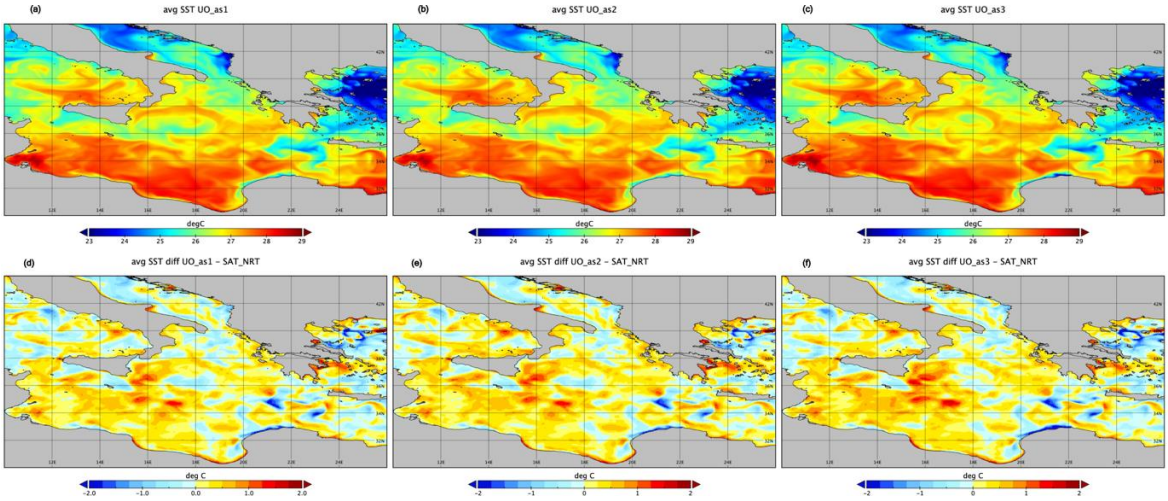

Figure 2.3: Average SST during September 15-18, 2020, for the three uncoupled experiments (first row) and difference with the satellite observations in the medicane area (second row).

In order to understand the SST differences just discussed we now describe the four components of the surface heat budget in the three experiments in Table 2.2 and Figure 2.4 .

Table 2.2: Mediterranean basin averaged heat fluxes, positive downward.

Variable description (Wm^{-2})	**UO_as1**	**UO_as2**	**UO_as3**
Net short wave radiation	205	201	227
Net long wave radiation	-87	-74	-70
Latent Heat	-95	-96	-108
Sensible Heat	-7	-7	-5
Net heat flux	16	24	44

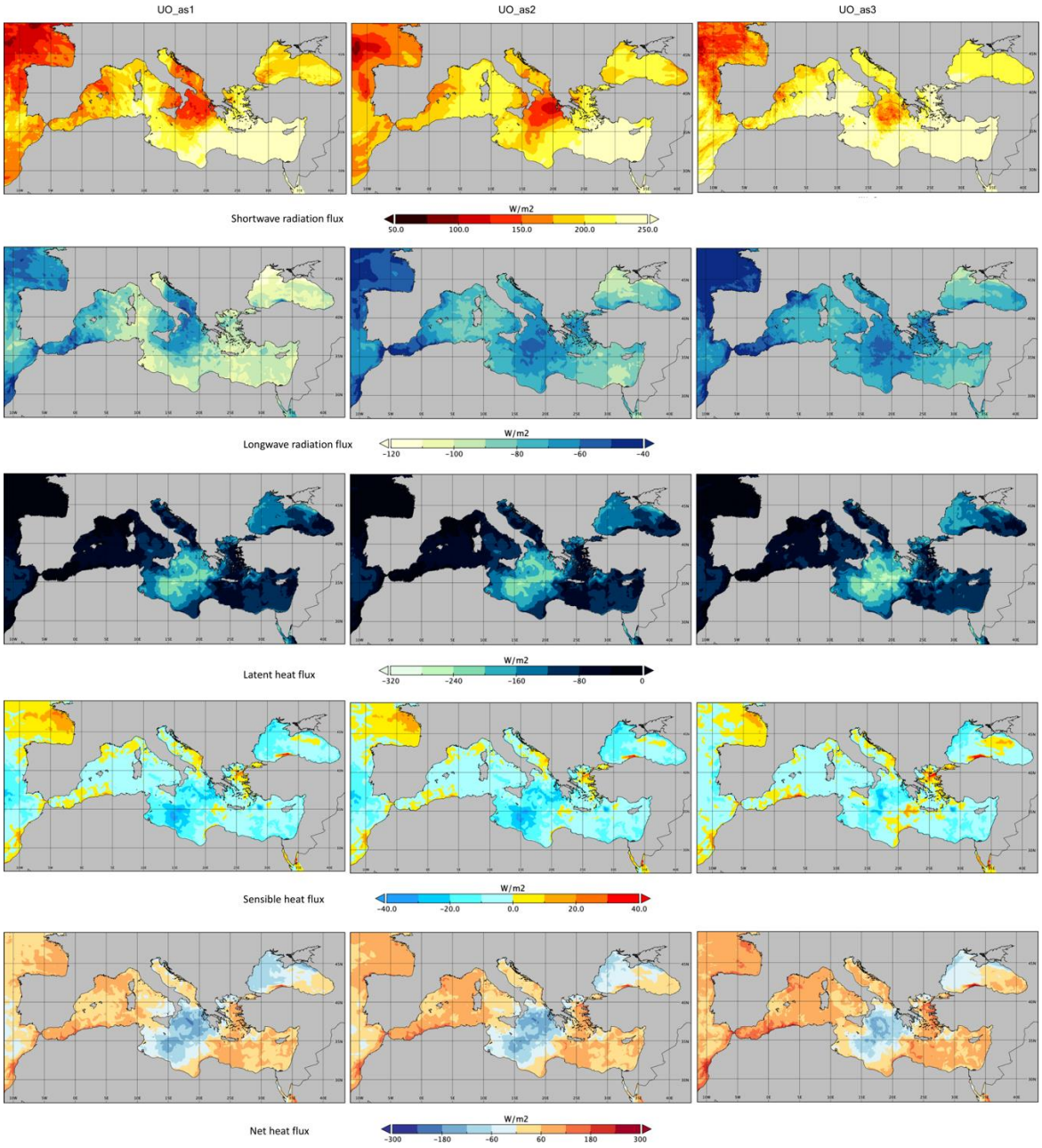

Figure 2.4: Average heat fluxes during September 15-19, 2020, for each uncoupled experiment. Values are the spatial average of the Mediterranean Sea from Dardanelles to the Strait of Gibraltar.

For *UO_as2* the main difference from *UO_as1* is associated with the net longwave radiation budget. This is due to the downward thermal radiation Q_{LWD} estimated in *UO_as1* with Bignami et al. (1995) (eq. 1-4, section 1.1.1.1) and not calculated by the ECMWF analysis system.

For *UO_as3,* there are three main differences in the components of the surface heat budget compared to *UO_as1 and UO_as2*. First, the downward net solar radiative flux

calculated by the atmospheric component is 26 Wm^{-2} and 22 Wm^{-2} larger than that calculated by ECMWF (*UO_as2*) and by MFS bulk formulae (*UO_as1*), respectively. Second, the net longwave upward flux is 4 Wm^{-2} and 17 Wm^{-2} smaller in absolute value than in *UO_as2* and *UO_as1,* respectively. Third, the latent heat is the largest heat flux and is ≈13 Wm^{-2} larger in absolute value than in *UO_as1* and *UO_as2*, because the calculated larger wind speed increases the turbulent exchange coefficients C_E estimated with Kondo, (1975). In *UO_as3,* the latent heat extracted from the ocean is considerably larger than in the other runs, with values up to -280 Wm^{-2} in the central Mediterranean where Ianos developed. The lower sensible heat flux results from the smaller temperature difference between the SST and the 2m air temperature compared to the other experiments.

Since the best SST comes from *UO_as1*, we conclude that the best parametrizations of the heat flux surface for the medicane is that of the MFS bulk formulae (section 1.1.1.1).

Finally, the average net heat balance of the Mediterranean is: *UO_as1*, 16 Wm^{-2}; *UO_as2*, 24 Wm^{-2}; *UO_as3*, 44 Wm^{-2} which is a large difference if compared with the values of the individual components. We argue that the uncertainty of these surface boundary conditions is one of the sources of the SST predictability error in the uncoupled ocean simulations.

The SSH difference at day +6 of experiment *UO_as1* with the MFS analysis is on the order of +5 cm everywhere (Figure 2.5a), which is higher than the estimated error in the MFS analysis (Clementi et al., 2021) which is to +3.3 cm. This is likely due to the initialization procedure used here which sets the SSH to zero. The *UO_as3* SSH differences with MFS (Figure 2.5b) are smaller in the basin while they are large along the Ianos path and they follow the SST difference pattern shown in Figure 2.2. Thus, we conclude that the initialization of the SSH should be inserted in future experiments such as *UO_as1* since the basin is large and deep and it will take long time to reconstruct the SSH from temperature and salinity and lateral boundary conditions.

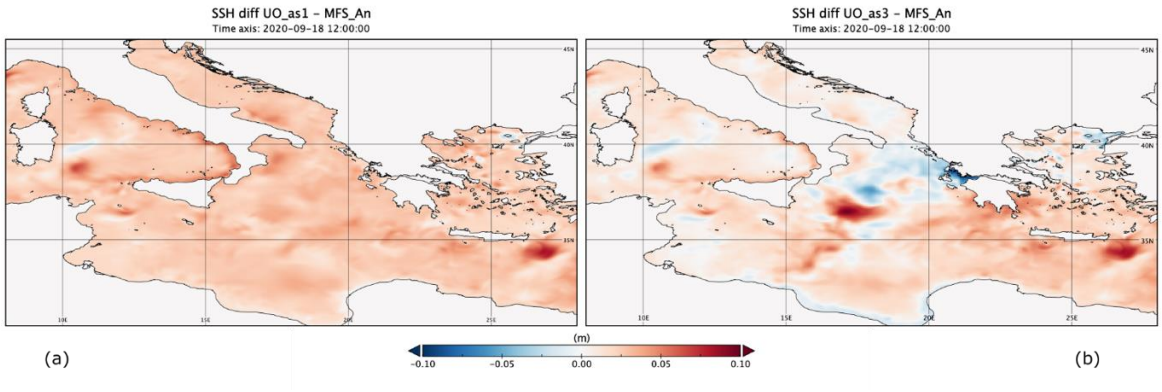

Figure 2.5: SSH differences at +6days with the MFS analysis.

2.2.2 Atmosphere

The goal of the uncoupled atmospheric runs is to test different configurations of the model by changing the prescribed SST and the physics schemes for the surface and planetary boundary layer, and to determine the heat budget at the ocean-atmosphere interface and compare it with the uncoupled ocean simulations.

The name of each atmospheric experiment is composed of: ***UA*** uncoupled atmospheric model, ***as*** is the atmospheric setup and ***UO*** denotes the source of the prescribed SST. In each experiment, the atmospheric model is initialized and laterally forced with 6-hourly ECMWF analyses. Specifically:

- ***UA_as0***. The atmospheric model is set as suggested in the WRF User's Guide for models with similar resolution: six classes Thompson scheme for the microphysics with explicit cloud resolving (no activation of any cumulus scheme, i.e. no sub-grid convection parametrization), RRTMG scheme for the radiative fluxes, MYJ scheme for the surface and planetary boundary layers, Noah model for the land-surface layers (Table 1.2). The prescribed SST is the daily SST from OSTIA (Good et al., 2020).
- ***UA_as0_UO***. As above, but the prescribed SST was simulated in the uncoupled ocean run *UO_as1*.
- ***UA_as5_U0***. This setup corresponds to a widely used configuration of WRF with the MM5 scheme for the surface and planetary boundary layers and the addition of the Tiedtke cumulus parametrization scheme and the six classes Thomson microphysics scheme (Table 1.2).
- ***UA_as5h_U0***. As above with an additional parametrization recommended for the tropical cyclones that modifies the surface drag coefficient (Donelan et al., 2004) and the exchange coefficients for heat and moisture (Garratt, 1994).

The experiments are compared in terms of surface pressure, 10-m wind field and cumulated precipitation, at the time of highest intensity of Ianos that was observed in the first hours of September 18, 2020 as shown in Lagouvardos et al. (2022). For sake of simplicity, the *UA_as0_UO* experiment is not shown in Figure 2.6 because the results are similar to the control run *UA_as0*.

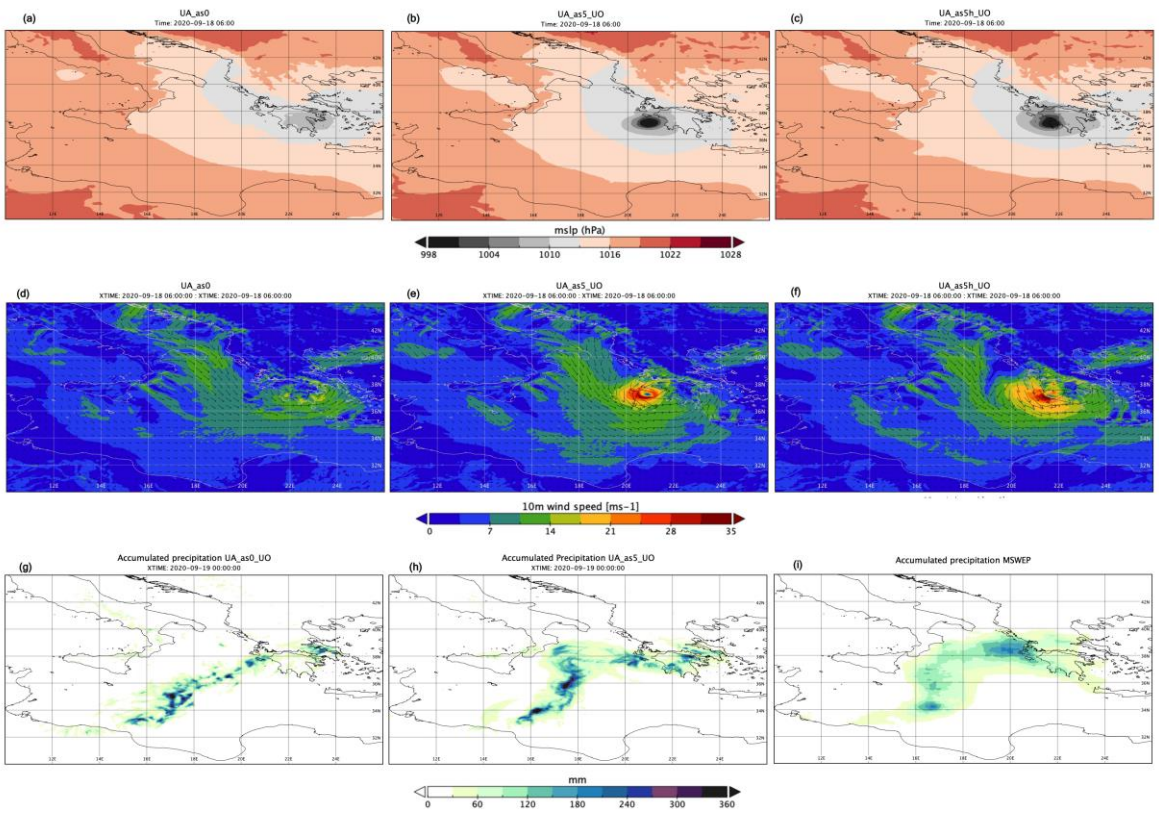

Figure 2.6: Uncoupled atmosphere experiments. 2020-09-18 06 UTC, surface pressure (a), (b), (c), 10-m wind field (d), (e), (f). Accumulated precipitation (g), (h) on 2020-09-19 00 UTC and MSWEP-V2 reference dataset(i)

According to the IANOS path derived from NCEP-FNL Analyses in Lagouvardos et al. (2022) on 18 September 00 UTC, the experiments show a fairly good agreement in the positioning of the surface pressure minimum, with an overall shift of about 1 degree to the south. The transit of the minimum surface pressure near to the Ionian Islands is advanced by 6 hours in the *UA_as0* and *UA_as0_UO* experiments, and at 06 UTC, the time near the maximum intensity of the event, the minimum surface pressure on the ocean is almost absent (Figure 2.6a). We conclude that the use of the ECMWF or *UO_as1* SST is not sufficient to properly capture the timing and magnitude of the Ianos pressure anomalies. However, the SST is not the only reason for the incorrect surface pressure simulation by the uncoupled atmospheric model because as pointed out in Miglietta et al. (2015), surface processes are less important than others in determining the correct evolution of the cyclone. In this case the surface and planetary boundary layer parametrizations are important: in fact, the *UA_as5_UO* and *UA_as5h_UO* experiments

are capable to capture minimum values of surface pressure (990 hPa) that are close to the observed values.

The wind fields at the same time are plotted in Figure 2.6d,e,f. It is evident that the UA_*as0* simulation does not reproduce a cyclonic wind pattern while the *UA_as5/as5h_UO* experiments produce maximum wind speeds of about 35 ms^{-1}, which is a realistic representation of the observed data showed in Lagouvardos et al. (2022).

Regarding the precipitation, it is helpful to use a reference dataset to speculate on the model outputs related to the different experiments. The MSWEP-V2 dataset (Beck et al., 2019) merges satellites observations, atmospheric reanalyses, and rain gauges data to elaborate a precipitation gridded field over the land and the ocean. Thus, it can be used for comparison with the model outputs, keeping in mind that its 0.1 degree resolution is about half the model one. The rainfall pattern of Figure 2.6h is very similar to the reference dataset in of Figure 2.6i and shows clearly that the cyclone track calculated in UA_as5_UO (and also in UA_as5h_UO, not shown) is closer to the reality with respect to UA_as0_UO. The accumulated precipitation seems to be overestimated in all the experiments over the ocean. The reason can be either the coarser resolution of the merged dataset (atmospheric reanalyses at 0.25 deg. do not properly resolve convection) and the lack of observed data to be merged. According to the Ianos simulated trajectory, the largest values of the cumulated precipitation on the land are themselves shifted southward over the Peloponnese peninsula instead over the Central Greece (Figure 3 in Lagouvardos et al., 2022) even though the maximum values are comparable. It is worth to notice that the MSWEP-V2 dataset underestimates the largest observed values over the Central Greece probably because those rain gauges were not merged into the dataset. Despite the analysis so far conducted is mainly qualitative, the comparison with the mentioned datasets shows that the resolution of the model is not fine enough to be fully convection permitting (*as0* experiments, Figure 2.6g), so that a cumulus parametrizations is needed (*as5/as5h* experiments, Figure 2.6h) to resolve the vertical dynamics associated to this intense event. This topic should be further investigated in the future through more detailed comparison with satellite precipitation data.

The analysis of heat fluxes is based on the average values during the simulated period from September 15 to September 18, 2020, calculated from the three-hour instantaneous model outputs.

Table 2.3:Time mean (15-18 Sept. 2020) and Mediterranean Sea averaged values for air-sea heat fluxes from the uncoupled atmospheric models (fluxes are considered positive downward).

Variable description (Wm^{-2})	**UA_as0**	**UA_as0_UO**	**UA_as5_UO**	**UA_as5h_UO**
Net shortwave radiation flux	222	221	224	224
Net longwave. radiation flux	-72	-73	-72	-72
Latent heat flux	-101	-103	-133	-128
Sensible heat flux	-7	-7	-5	-5
Net surface heat flux	42	38	14	19

The average surface heat fluxes of the Mediterranean basin are shown in Table 2.3 for the different experiments. The radiative fluxes do not differ significantly between experiments because they were calculated using the same WRF radiative scheme. Therefore, the small differences in the shortwave radiative fluxes result from the difference in cloud cover and water vapor content of the atmosphere due to the cumulus parametrization and the PBL scheme. Comparing the values of the surface heat fluxes between the uncoupled ocean (Table 2.2) and the atmospheric experiments (Table 2.3), we find that the main differences are in the shortwave radiation and latent heat fluxes, leading to several differences in the net heat fluxes depending on which experiment is being compared.

Figure 2.7 shows the radiative fluxes for experiment *UA_as5_UO* only, where the influence of the Ianos clouds and the water vapor content of the air on the radiative fluxes is evident.

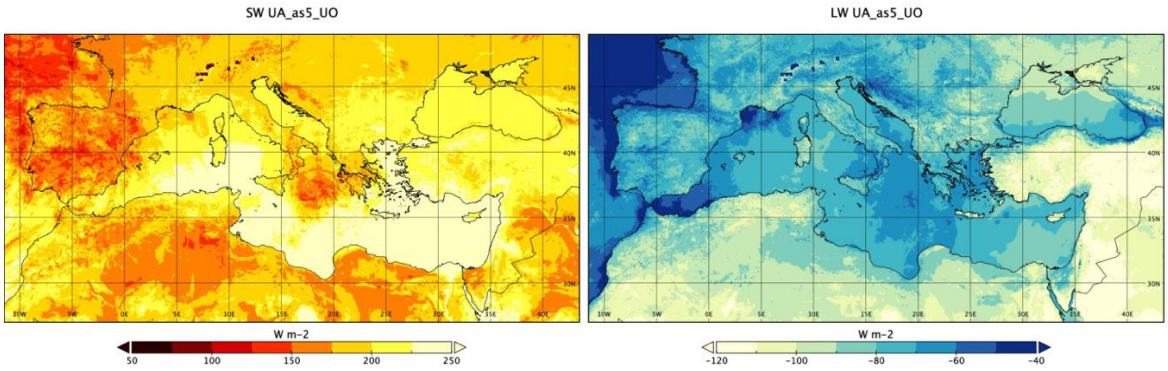

Figure 2.7: Average net shortwave and longwave radiative fluxes for UA_as5_UO during the period 15-18 September 2020.

Figure 2.8 shows the fields for the turbulent and net surface heat fluxes. *UA_as0* and *UA_as0_UO* share the MYJ schemes, so only the latter is shown, whereas *UA_as5_UO* and *UA_as5h_UO* use the MM5 schemes with the hurricane parametrization added in the latter.

The MM5 scheme calculates larger latent heat values of about 30 Wm^{-2} compared to the MYJ scheme (Table 2.3), but this difference in the Ionian Sea is about 80 Wm^{-2} with the largest latent heat values calculated in the *as5/as5h* experiments up to 360 Wm^{-2} (Figure 2.8, first row). In the *as5h* experiment, the latent heat is not larger than in the *as5* experiment because the increased wave drag coefficient used in *as5h* (Donelan et al., 2004) has a negative feedback on the wind speed that reduces the latent heat estimate. Referring to the feedback of heat exchange at the wind amplification surface (Emanuel, 1986), we argue that the differences in latent heat are responsible for the lower intensity of the cyclone in *as0* experiments.

The amount of sensible heat released to the atmosphere is similar in all experiments, and the largest values in the Ionian Sea are about 45 W/m^2 (Figure 2.8, second row).

The sum of the above quantities and the radiative fluxes gives the net heat flux, which is shown in Figure 2.8, third row. Table 2.3 shows that the Mediterranean Sea is

still gaining heat in mid-September due to the contribution of solar radiation, while in the Ionian Sea the heat loss is very high with values exceeding 250 W/m^2.

Looking at the maps and the values averaged over the basin, the difference between the two schemes MYJ and MM5 in terms of heat loss from the sea in the Ionian Sea is clear. The total heat gain at the basin scale is more than halved in the *as5/as5h* experiment due to the larger latent heat fluxes.

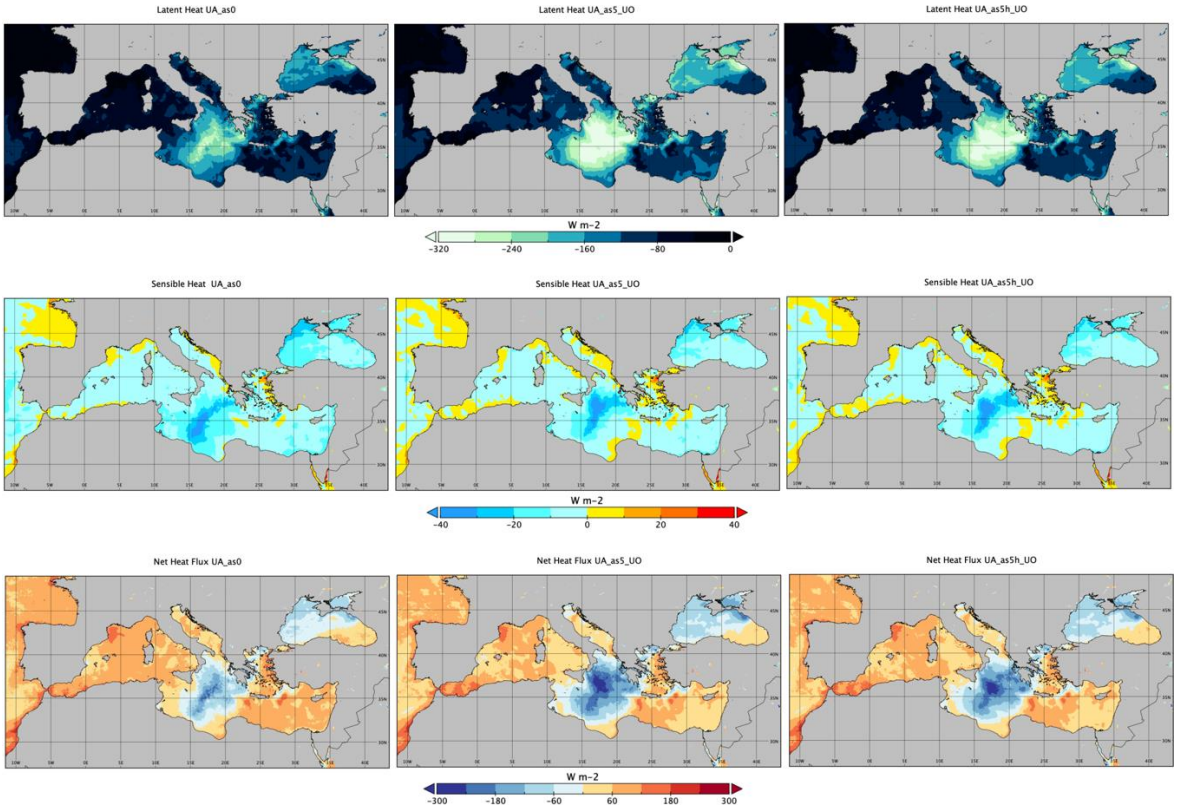

Figure 2.8: Average latent, sensible, and net heat fluxes in the UA_as0 control run, UA_as5_UO and UA_as5h_UO, during September 15-18, 2020.

2.3 Skills of the uncoupled simulations

2.3.1 Uncoupled ocean simulations

We divide our analysis of simulation skills into a consistency check and a comparison with observational data. The consistency check consists of comparing the surface currents with the reference MFS analyses (Clementi et al., 2021). The MFS currents cannot be considered the best estimate of reality in this case, since we know that the ECMWF forcing underestimates the Ianos winds. However, the comparison gives an idea of the "consistency" between the results. Figure 2.9 shows the UO simulation for day 2020-09-17 (+6 days from the initial condition) and the MFS analyses. As expected, the uncoupled runs *UO_as1* and *UO_as2* show no significant differences in the surface currents compared to the MFS analyses so the comparison is made only for the experiment *UO_as3*. The pattern of surface currents is different in the divergent region under the Ianos path in the Ionian Sea. To confirm these two different patterns, the data from the ARGO floats should be used to verify the different stratification that occurs in the upwelling region under Ianos. This comparison will be carried out in the next future.

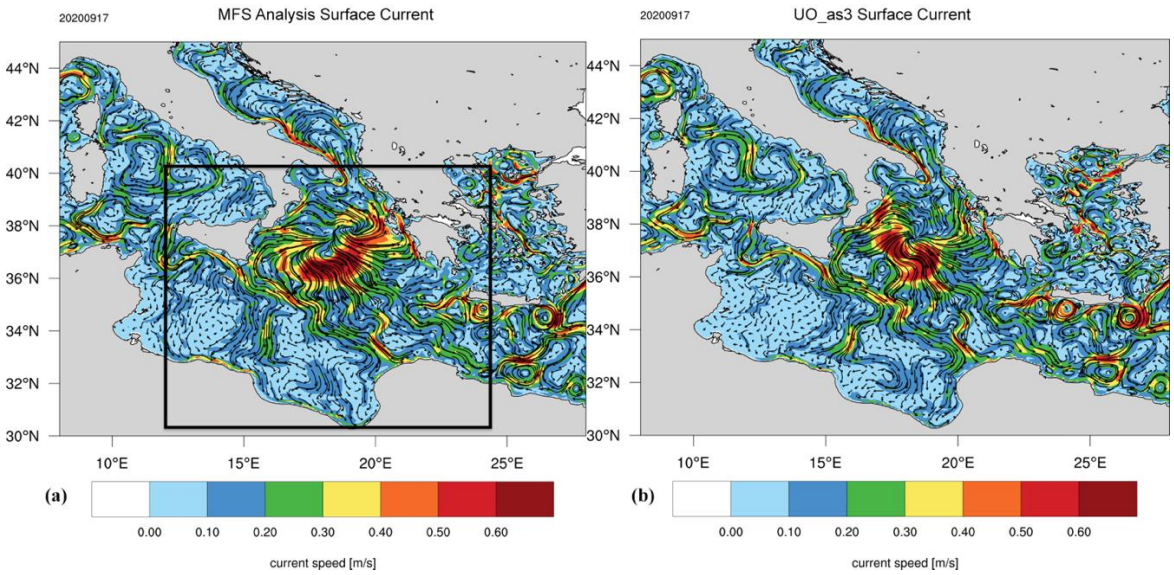

Figure 2.9: surface current of the day 2020-09-17 from the MFS Analysis (a) and UO_as3 (+3days) run (b). the black box delimitates the Central Mediterranean Sea.

An objective assessment of the simulation skills can be made by calculating two statistical indices basin-averaged for the generic variable X, given the total number of valid grid points N:

$$BIAS = \frac{\sum_{i=1}^{N}(X_{mod,i} - X_{obs,i})}{N} \qquad RMSD = \sqrt{\frac{\sum_{i=1}^{N}(X_{mod,i} - X_{obs,i})^2}{N}} \qquad (2\text{-}3)$$

Figure 2.10 shows the indices for the surface current components in the *UO_as1* and *UO_as3* experiments in the Mediterranean Sea (a,b) and in the specific area of Ianos development (c,d). The deviation of the surface current in *UO_as1* from the MFS Analyses is negligible, while in *UO_as3* the surface current is larger than in the analyses and the difference is more evident in the Ionian Sea is more significant (c,d). In the case of the currents, as mentioned earlier, these indices are not really an assessment of the quality of the uncoupled simulation, but rather a consistency check, since the MFS analysis is produced with weaker winds than in reality, as shown in section 2.2 of this chapter.

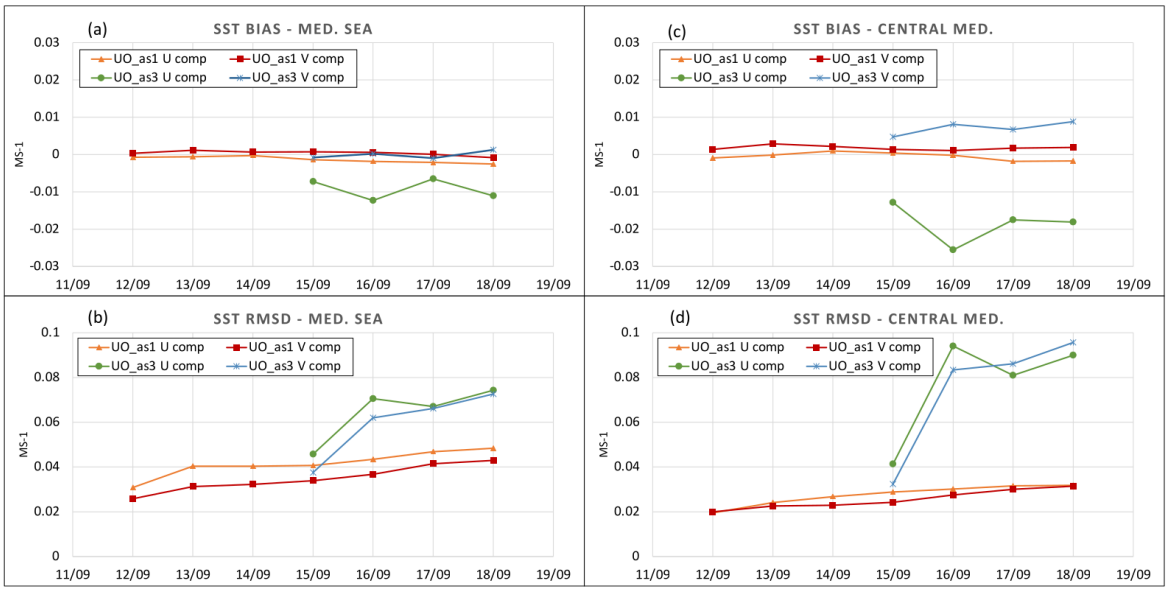

Figure 2.10: Statistical indices BIAS and RMSD for the surface current of experiments UO_as1 and UO_as3, in the Mediterranean Sea (a, b) and in the central Mediterranean Sea (c, d) delimited by the black box in Figure 2.9.

A quantitative assessment of the simulation skills was performed by comparing the simulated SST with the remotely sensed SST from the Mediterranean Sea High Resolution and Ultra High Resolution Sea Surface Temperature Analysis dataset (Buongiorno Nardelli et al., 2013a). This dataset contains the nighttime foundation ocean temperature observed from different satellites and it has been processed to remove the cloud cover and fill the gaps. For this porpoise, a time window around the nominal time of the field is considered to be estimated and the information from the past and future satellite data is merged. This can lead to a bias in SST especially for high intensity events where clouds play a role, such as medicane events. In the future L3 SST products that do not account for cloud gap filling should be used to better evaluate the performance.

The SST BIAS and RMSD were calculated for the Mediterranean Sea from the Dardanelles to Straits of Gibraltar and for the central Mediterranean Sea in the black box in Figure 2.11. The latter also shows the complicated pattern of differences that lie on the scales of the Mediterranean eddies that populate the area.

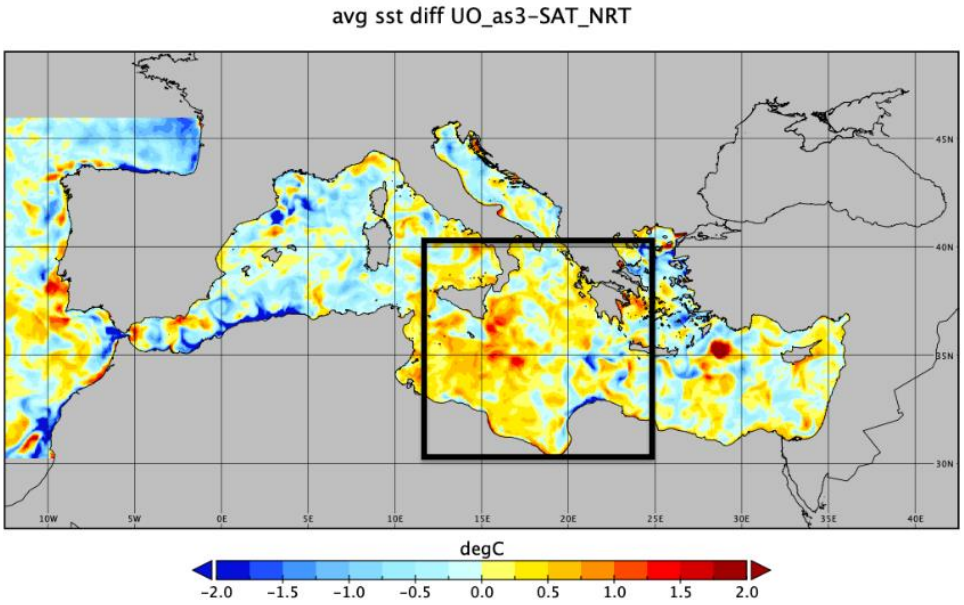

Figure 2.11: Average SST difference (model-observed). The black box delimits the area of the central Mediterranean where the statistical indices are calculated.

In Figure 2.12 we show the RMSD and BIAS for the three uncoupled ocean experiments. On the basin scale, *UO_as2* is the experiment that performs better, while *UO_as1* in the central Mediterranean has the lowest values of BIAS and RMSD. The SST BIAS in the central Mediterranean is positive in all three experiments, which is likely due to the lack of cooling due to the insufficiently resolved medicane in *UO_as2* and the large radiative fluxes in *UO_as3.* Part of this warm bias could come from SST processing to fill in the gaps due to cloud cover. As expected, the RMSD increases during the development of Ianos in the central Mediterranean and likely converges to climatological error values (~0.5 C when we consider the long-term RMSD in MFS) at the end of the simulation.

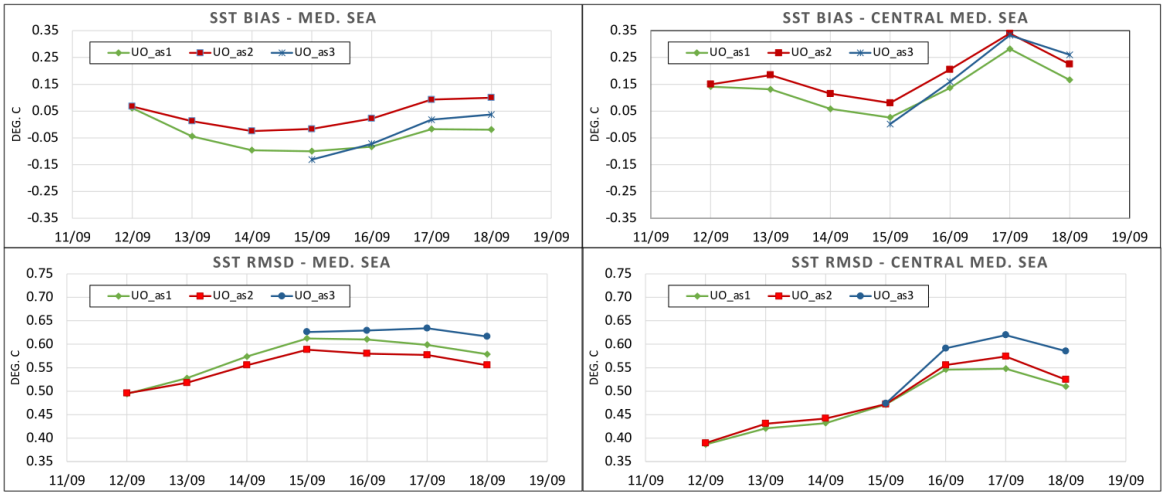

Figure 2.12: BIAS and RMSD of the calculated versus remotely sensed SST in the Mediterranean and central Mediterranean (black box in Figure 2.11).

2.3.2 Uncoupled Atmosphere

In this section, the same statistics used for the ocean component are presented for the 10m wind field components. This is not actually a proper validation of the atmospheric component, which would require a more detailed analysis of the results involving multiple variables at different heights. Nevertheless, it is worthwhile to

understand the overall reliability of the wind field affecting the latent heat flux, which is the largest heat flux component in extreme events such as medicanes.

The dataset used for the comparison is the Global Ocean Hourly Sea Surface Wind and Stress from Scatterometer and Model from the CMEMS Service. This dataset is particularly useful because it provides a high temporal and spatial resolution wind field with stress equivalent over the ocean, and the scatterometer data are used to rectify the ECMWF predicted wind field. For comparison, the data set was resampled to the model grid.

Figure 2.13 shows a qualitative comparison of the 10 m wind field of each experiment with the satellite wind field at the time of maximum intensity of the medicane before hitting the Ionian Islands. This comparison confirms the results shown in Figure 2.6: in the *as0* experiments the cyclone is shifted about 1 degree southward resulting in an earlier landfall of about 6 hours on the central Greece. The location of the cyclone in the *as5* experiments is the closest to the observations, while the hurricane parametrization in *UA_as5h_UO* produces a stronger cyclone than the observed one.

The quantitative assessment of the simulation's skill is summarized in Figure 2.14. The metric is the same as the SST (2-3) which is calculated every 3 hours for each ocean grid point and spatially averaged. At the scale of the medicane and during its maximum intensity day *as5* has the lowest bias (Figure 2.14b). The MYJ physics scheme in the *as0* experiments yields almost zero BIAS at the basin scale, but large negative values in the central Mediterranean, confirming that the simulation produces a weaker cyclone, and the addition of the *UO_as1* SST does not improve the results. Interestingly, the *UA_as5_UO* experiment is the one that has the lowest RMSD both at the basin scale and in the Ianos development area (Figure 2.14c,d). It can be concluded that the experiment *UA_as5_UO* gives better overall results than the other experiments for this extreme and localized event.

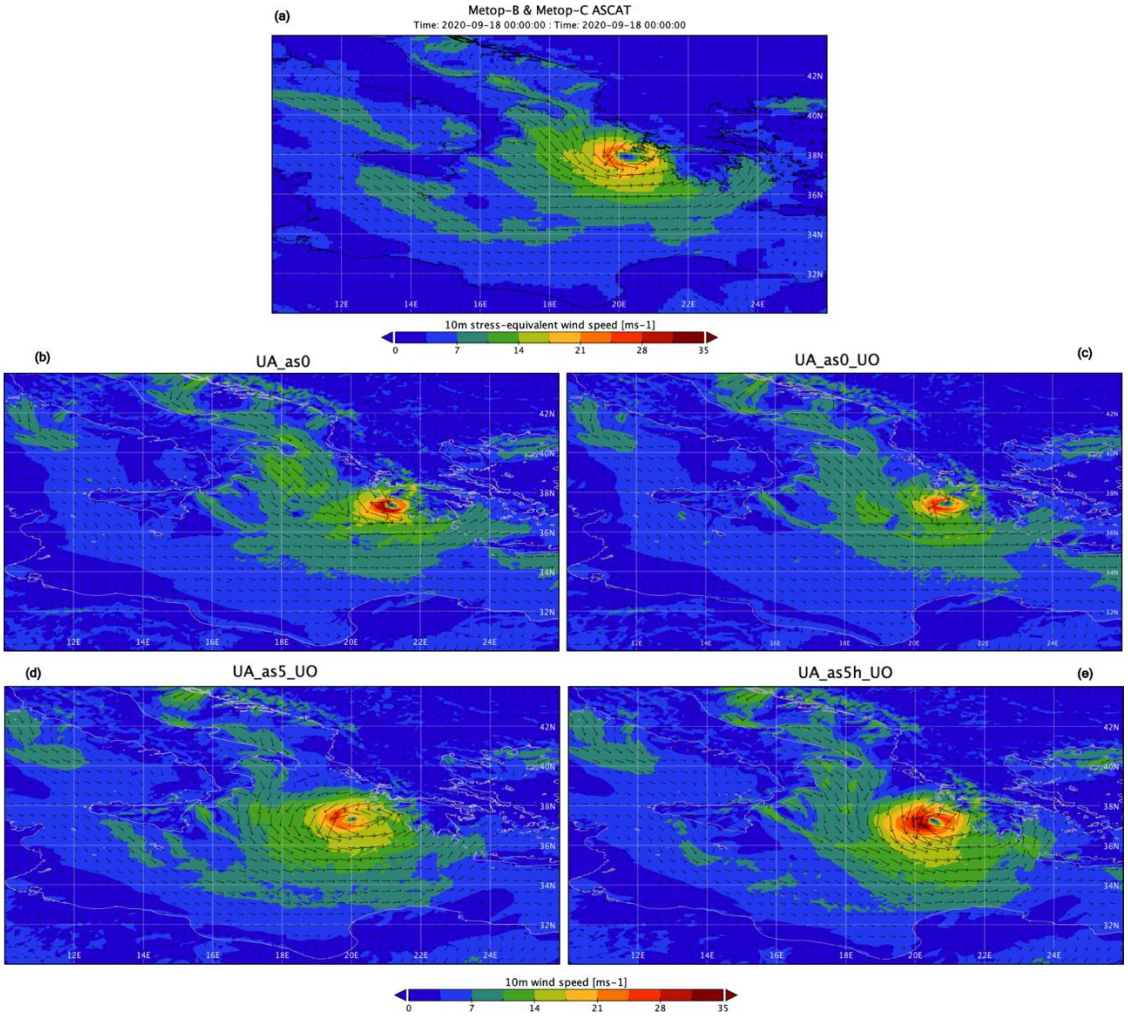

Figure 2.13: 10m wind fields at 2020-09-18 00UTC (+3days) elaborated from scatterometers ASCAT Metop-B and Metop-C (a) compared with the experiment's outputs (b, c, d, e).

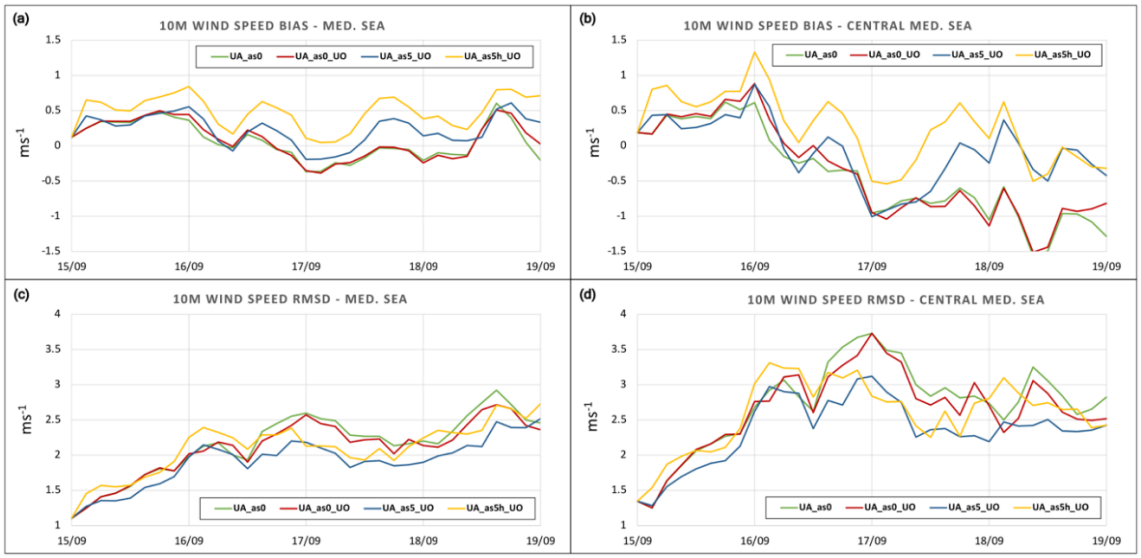

Figure 2.14: BIAS and RMSD for the 10m wind speed calculated in the experiments, compared with the remote sensed dataset for the Mediterranean Sea (a,c) and Central Mediterranean Sea (b,d).

2.4 Conclusions

The formation and evolution of a Mediterranean tropical-like cyclone in the Ionian Sea was simulated by downscaling ECMWF analyses with a regional uncoupled atmospheric model at 1/24° resolution. The effects of Medicane Ianos on the dynamics of the Mediterranean Sea were also studied using an uncoupled ocean model with the same resolution. These uncoupled models are the two components of the coupled model SEAS.

A total of seven uncoupled experiments were performed, three for the ocean and four for the atmosphere, changing the model setup and the surface and planetary boundary layer parametrizations. A qualitative comparison is made with the currents of the operational MFS system for the same event. A quantitative comparison with satellite data was performed for both components to assess which model configuration performs best in the Medicane simulation. This cannot be considered a complete validation, as it would require more variables at different heights and depths, as well as longer and more robust statistical time series.

The main focus was on the variables at the air-sea interface, such as SST, 10m winds, and especially the heat fluxes responsible for the energy exchange between the two components.

The comparison of the UO_as1 experiment with UO_as2, where the downward radiative fluxes are given by ECMWF analyses, shows that the MFS bulk formulae for the radiative fluxes (Reed 1977; Rosati and Miyakoda 1988; Bignami et al., 1995) still give good results despite the parametrizations of the effect of the cloud cover and the moist content in the atmosphere. The SST comparison between the model and remote sensing shows that at the basin scale, *UO_as2* performs slightly better, while *UO_as1* performs slightly better in the medicane evolution domain. The difference in net heat flux in the two experiments is mainly due to the larger downward longwave radiation in *UO_as2*. In the *UO_as3* experiment, the atmospheric variables and downward radiative fluxes from the uncoupled WRF simulation are used to force the uncoupled ocean experiment, and the BIAS and RMSD are largest in the Ionian Sea, suggesting that this air-sea exchange is too simple to take advantage of the WRF downscaling of atmospheric conditions.

The largest differences between the uncoupled atmospheric simulations arise from the different physics schemes used: MYJ (Janjic, 2001) or MM5 (Jiménez et al., 2012). *UA_as0* and *UA_as0_UO,* using the MYJ scheme, calculated a smaller surface pressure minimum with a southward-shifted Ianos path and an anticipated landfall. The addition of the SST of *UO_as1* in *UA_as0_UO* does not significantly improve the simulation. The MM5 scheme used in *UA_as5_UO* improves the simulation of the medicane by calculating a deeper low pressure and better positioning and timing, while the addition of the hurricane parametrization in *UA_as5h_UO* results in a cyclone slightly more intense than in reality. At the end of section 1.2.1 and in Figure 1.6 it was shown how the hurricane parametrization in the MM5 surface layer scheme acts on the estimation of the exchange coefficients for the enthalpy fluxes, generating an intensification of the cyclone. The comparison of the experiments *UA_as5_UO* and *UA_as5h_UO* (same surface layer scheme) shows that the latent heat extracted is larger in *UA_as5_UO* (Table 2.3) even at the scale of the Ionian Sea (not shown). Nevertheless, comparing the instantaneous latent heat fields, large differences can be found at smaller scale in different areas and at different time (**Error! Reference source not found.**). These generate differences in the convergence of air masses between the two experiments that might determine the overall intensification of the cyclone in *UA_as5h_UO*.

In summary, for the uncoupled atmospheric experiments, the *UA_as5_UO* simulation is the best compromise.

The differences in the net heat fluxes between the uncoupled atmospheric experiments arises from the different surface layer scheme, with the MM5 calculating a latent heat flux ≈30 W/m^2 larger than that of MYJ scheme. All the other heat fluxes are very similar in the experiments.

Previous studies (Miglietta et al. 2015, Pytharoulis et al. 2018, Mylonas et al. 2019) pointed out that it is not possible to determine an optimal combination of physical parametrizations in the atmospheric model that is able to capture all the characteristics of the medicane, and considering that each cyclone can have different characteristics, the number of the uncoupled experiment was limited to only four. The reason is that in the perspective of the coupled ocean-atmosphere predictions, the balance of heat fluxes between the components was considered of major importance.

The net heat flux at the interface in *UA_as5_UO* and *UA_as5h_UO* is closer to *UO_as1*, which performs well in predicting the ocean dynamics. Therefore, it makes sense to use the setup of the *UA_as5_UO* experiment for the atmospheric component. Then, in the last chapter of the thesis, the first coupled experiment using this air-sea interaction physics will be introduced.

Chapter 3

Uncoupled ocean forecasting

SEAS is a prototypal regional atmosphere-ocean coupled model that aims to become a coupled forecasting system for the ocean dynamics of the Southern European Seas. The roadmap to this goal includes a preliminary evaluation of the forecasting skills of the uncoupled oceanic model. In particular, since the oceanic component was developed starting from the setup of the MedFS, its forecasting skills should be examined in the uncoupled configuration and compare to those of the state-of-the-art Mediterranean Forecasting System. Thus, the short-term ocean forecast capabilities of the uncoupled model SEAS for one winter and one summer season are examined in this chapter.

In the coupling perspective it is also necessary to test a different configuration of the surface boundary conditions. In the MedFS setup discussed in 1.1.1.1 empirical formulae are used to calculate the attenuation of the radiative fluxes due to clouds and water vapor. The input atmospheric fields are the cloud cover, the 2 meters dew point temperature and the mean sea level pressure that have about half the spatial resolution. The idea is to avoid using the bulk formulae and provide more accurate short and long wave radiative fluxes as surface boundary conditions. The reason is that in the ECMWF-IFS the radiative fluxes are calculated along the atmospheric column considering the vertical extension of the clouds, the calculated water vapor content of each grid cell and the sub-grid approximations. Moreover, the ECMWF-IFS radiative transfer module (Hogan and Bozzo, 2016) is very similar the same as RRTMG used in WRF in this work, both in the uncoupled and coupled configuration.

Whatever it is the coupling strategy chosen (Coupling 1 or 3 in Figure 1.2), the radiative fluxes will be always provided by the atmospheric component. Thus, a preliminary test of the oceanic forecasting skills of the uncoupled SEAS model with this new configuration is valuable in the coupling perspective.

Furthermore, the objective of this chapter is to perform a statistical evaluation of the performance of the forecast model with two air-sea parametrizations using the ECMWF forcing, while the previous chapter was a single event simulation without considering the atmospheric forecast forcing and the lateral boundary conditions. The result of this forecast forms the reference basis for the next coupled ocean forecast of the system SEAS.

3.1 The forecasts setup

The ocean model was run in forecast mode testing the *UO_as1* setup (MFS bulk formulae) and the *UO_as2* setup (MFS bulk formulae with prescribed radiative fluxes from the atmospheric model) to assess whether the ECMWF radiative fluxes performed better than those calculated using Reed (1977), Rosati and Miyakoda (1988) and Bignami et al. (1995) expressions in the MFS bulk formulae (section 1.1.1.1).

The forecast range was set to 5 days, which is an arbitrary choice considered to be a compromise between the current forecast range of the MFS (10 days) and that of most of the regional high-resolution atmospheric models (3 days). The spin-up period was set to 1 day because the SEAS ocean model is initialised in the Mediterranean and Black Seas whit the merged analyses from the MFS (section 1.3.2), so no time is required to adjust the energy/vorticity to a higher horizontal resolution. In the Atlantic, a longer spin-up time would be preferable to correctly downscale the dynamics of the parent model (CMEMS-GLO, 1/12° resolution) to the 1/24° resolution. In addition, Oddo et al. (2009) have shown that the dynamic connection between the Atlantic Ocean and the Mediterranean Sea through the Strait of Gibraltar (width ≈ 7 km, depth max 300 m) occur on monthly time scales for certain variables. Considering that the merging of the Global and MFS analyses occurs outside the Strait of Gibraltar between 7° - 6.5° W, one day spin-up time may be considered adequate to resolve anti-estuarine two-layers flow at the strait. These considerations suggest that the initial error associated with one day of spin-up may be considered acceptable, but this point should be further investigated prior to operational activity of SEAS forecasting system.

The ECMWF forecasts (1/10° resolution) are used for the atmospheric forcing and also provide the downward radiative fluxes for the *SEAS_UO_as2* setup. Atmospheric forecasts are hourly for the first 3 days and 3-hourly for the other days.

The ocean forecast is initialized every 5 days from the merged analyses of different ocean models (section 1.3.2) so that the spin-up period overlaps with the last day of the previous forecast, and the seasonal short-term forecast is the concatenation of several 5-day forecasts. This is shown in Table 3.1 for a generic month.

Table 3.1: Schematic of the short-time scale ocean forecast. The bold black lines represent the analysed IC.

day 01	day 02	day 03	day 04	day 05	day 06	day 07	day 08	day 09	day 10	day 11
1h ECMWF forec.			1h ECMWF forec.		1h ECMWF forec.			1h ECMWF forec.		1h
spin-up	day +1	day +2	day +3	day +4	day +5					
					spin-up	day +1	day +2	day +3	day +4	day +5

3.2 The target periods

Two periods of three months were chosen to evaluate the short-term uncoupled forecast system: January to March 2021 for winter time and July to September 2021 for summer time. The winter and summer periods were chosen to test the performance of the model during dense water formation in winter and during marine heat waves in summer.

According to the remotely sensed SST dataset L4-SAT (Buongiorno Nardelli et al., 2013) , the Mediterranean Sea exhibited a positive SST anomaly during both winter and summer (Figure 3.1a,b). The anomaly was calculated in comparison to the daily pentad climatology CNR-ISMAR-GOS created from 21 years of AVHRR Pathfinder data. In the winter season, the anomaly increased eastward from values below 0.5°C in the west to values above 2°C in the northern Aegean. In the summer, the SST anomaly was still largest in the northern Aegean, while large areas of the central Mediterranean were above 1.5°C. The pattern of the SST anomaly almost coincides in extent and magnitude with that of the 2m air temperature (Figure 3.1c,d) computed by the CMCC coupled seasonal forecasts model (Gualdi et al., 2020).

The average seasonal wind speed is shown in Figure 3.1e,f and is the mean of the wind intensity calculated from the ECMWF dataset at each forecast time. In winter, surface winds are more intense than in summer, with the well-known wind regimes of the Gulf of Lions (mistral) and the Aegean Sea (etesian).

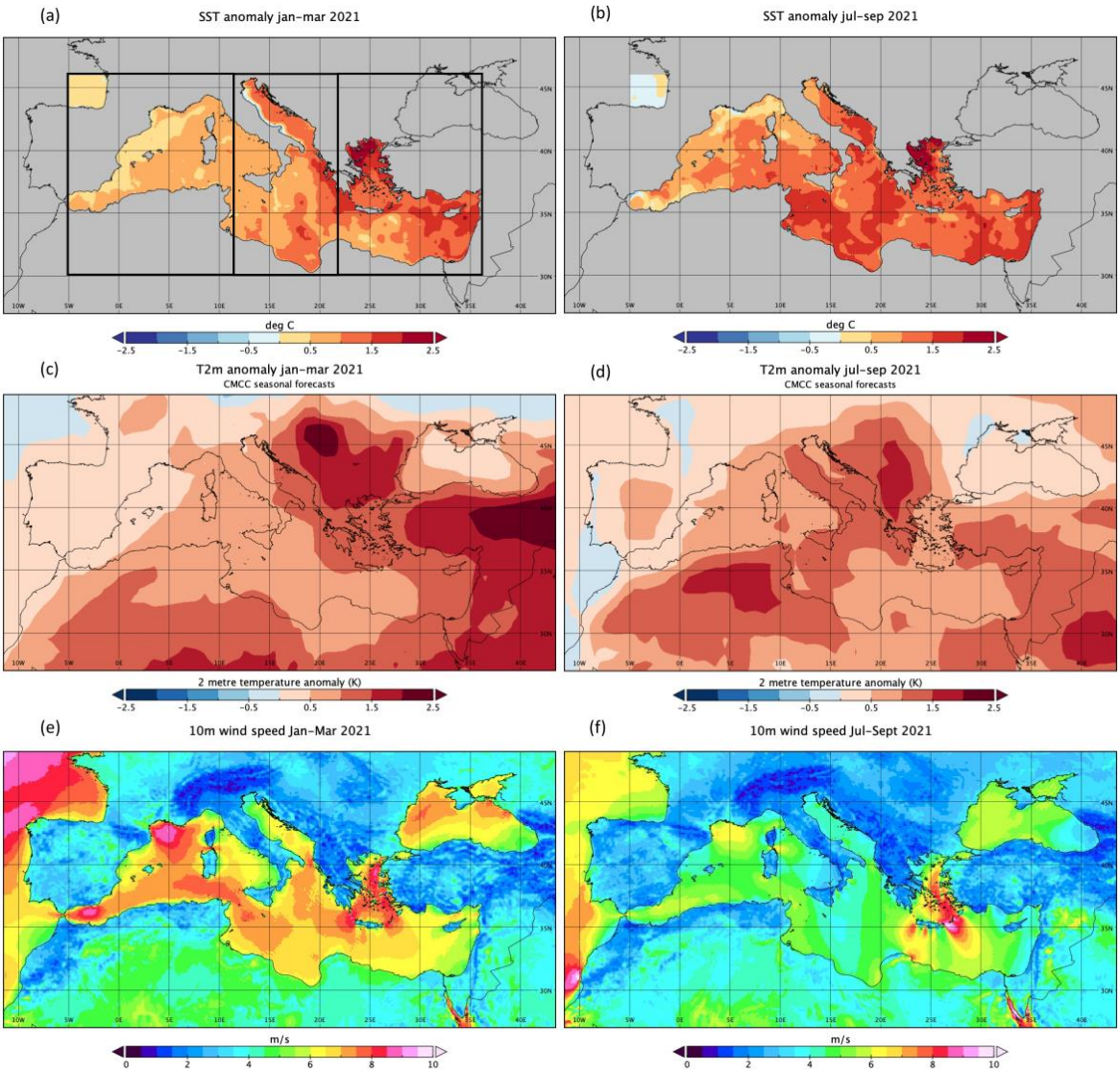

Figure 3.1: SST anomaly (a,b) from the SST_MED_SST_L4_NRT dataset, 2m air temperature anomaly from CMCC seasonal forecasting model (c,d), and 10m average wind speed from the ECMWF forecasts (e,f).The black boxes in (a) delimit the sub-basin regions.

3.3 Uncoupled ocean forecast skills

The forecast skills of the two uncoupled SEAS configurations were evaluated using the satellite SST of the L4-SAT dataset. According to the dataset specifications, the post-processed SST refers to night time, so the SST average of three hours, from midnight to 3 AM, of each day was extracted from the forecasts. The basin-averaged statistical indices for the SST difference (model-observations) described in (2-3) were calculated and the time series are shown in Figure 3.2.

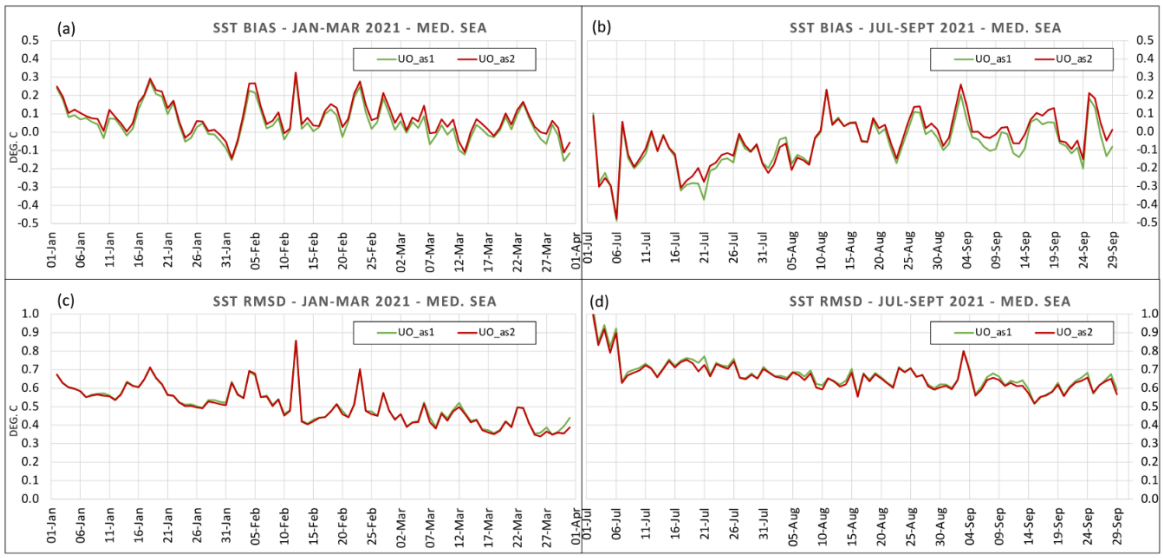

Figure 3.2: SST BIAS (a,b) and RMSD (c,d) respectively for the winter (left column) and summer period (right column) of 2021.

It is evident that *SEAS_UO_as1* and *SEAS_UO_as2* have the same performance without significant difference, which means that the empirical formulations of the downward radiative fluxes of Rosati and Miyakoda (1988) and Bignami et al. (1995) together with the climatological albedo values of Payne (1972) still provide a good estimate. With respect to BIAS, *SEAS_UO_as1* seems to perform better than *SUAS_UO_as2* during the winter season with a lower warm deviation, while in the summer the initial cold bias decreases and oscillates toward zero by the end of the period.

In terms of the mean square of the SST differences, the two experiments perform equally. During the winter season, the RMSD shows a decreasing trend toward spring, while the RMSD is largest during the summer period (corresponding to the largest negative BIAS), but shows a slightly decreasing trend toward fall. This suggests that the best ocean model results are obtained in the interseasonal periods. This trend and the magnitude of the RMSD are confirmed in the 2019 validation assessment for the MFS (Clementi et al., 2021).

It is difficult to argue about the origin of the large cold bias during the summer season. This obviously does not depend on the estimate of radiative fluxes, as it is shown in both *SEAS_UO_as1* and *SEAS_UO_as2*. It also does not depend on the albedo values, which are almost the same in the three months (0.06, 0.06, 0.065). One source of uncertainty could be an overestimation of the exchange coefficients for the turbulent heat fluxes at low wind speeds (in the summer) in the formulation of Kondo (1975). Another source of uncertainty could be a different representation of SST. The seawater temperature is calculated in the first model layer (1 m depth), while the observed temperature is the so-called foundation temperature, which is almost free from the diurnal cycle that in summer is more relevant.

The Table 3.2 summarizes the time averages statistics. The Mean Absolute Error has also been calculated, given N is the total number of valid grid points:

$$MAE = \frac{\sum_{i=1}^{N} |SST_{mod,i} - SST_{obs,i}|}{N} \quad (3\text{-}1)$$

Table 3.2: Spatial and temporal averages of the statistical indexes for each experiment.

	SEAS_UO_as1		SEAS_UO_as2	
	jan-mar 21	jul-sep 21	jan-mar 21	jul-sep 21
BIAS	0.05	-0.07	0.08	-0.05
MAE	0.38	0.49	0.37	0.48
RMSD	0.51±0.10	0.68±0.08	0.50±0.10	0.66±0.08

All values confirm better performance in the cold period, and the RMSD of both periods is very close to the MFS RMSD for the year 2019 (0.57±0.11 °C, Clementi et al., 2021). We see an interesting pattern: in winter, *SEAS_UO_as2* has twice the BIAS than *SEAS_UO_as1* while in summer it is better. We argue that a correction factor should be considered if the ECMWF radiative forcing is to be used in future MFS forecasting. The problem is probably related to uncertainties in cloud cover in winter.

The mean SST of both periods was compared to the mean SST of the MFS analyses which do not have problems in filling the cloud cover gaps as for the L4 SST (Figure 3.3).

The second finding concerns the large SST differences in the Atlantic Box. Although temperature profiles are not assimilated in that area, the problem of initializing the dynamics is not present in the operational MFS analyses. Conversely, only one day spin-up was considered in the SEAS model, and the SST still adjusts for the dynamics at higher horizontal resolution, suggesting that one day spin-up may be too short for the Atlantic SST.

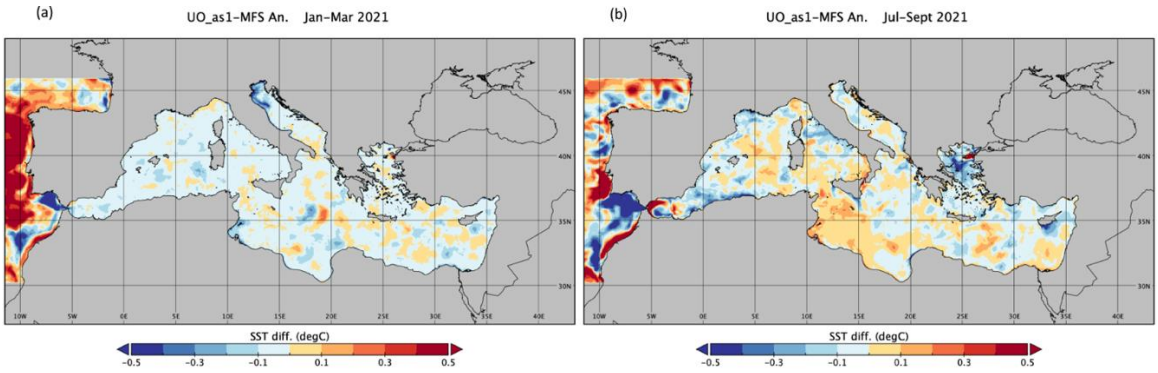

Figure 3.3: SST average difference between the uncoupled SEAS model (UO_as1 setup) and the MFS Analyses, in the winter period (a) and summer period (b) of 2021.

3.4 Heat fluxes in the uncoupled ocean forecast

In this section, the results of the uncoupled ocean predictions for the two seasonal periods are presented, with emphasis on the heat fluxes.

Here the *SEAS_UO_as1* and *SEAS_UO_as2* experiments are again compared. Table 3.3 shows that the net heat flux difference between the two model configurations (8 Wm^{-2}) is due mainly to the longwave radiation (15 Wm^{-2}), with a larger negative value in absolute value in *SEAS_UO_as1* experiment than in *SEAS_UO_as2*, and to the shortwave radiation (-6 Wm^{-2}). This is only due to the differences in the downward longwave components, which in turn lead to different time-averaged net heat losses. As noted, *SEAS_UO_as1* appears to have a negative net heat flux balance, which is well-known to be specific to the Mediterranean Sea (Castellari et al., 1998; Pettenuzzo et al., 2010), even if on decadal time scales, while *SEAS_UO_as2* does not.

Overall, it can be concluded that the prescribed ECMWF solar radiation is the same as that calculated using the MFS bulk formulae, while the prescribed ECMWF longwave radiation is very different from that calculated using Bignami et al. (1995) formulation. As previously noted, a correction factor should be computed if the ECMWF longwave downward heat flux is used in the future SEAS system.

Table 3.3: Basin averaged heat fluxes for both periods, units are Wm^{-2}

Variable description (Wm^{-2})	**SEAS_UO_as1**	**SEAS_UO_as2**	**SEAS_UO_as2-SEAS_UO_as1**
Net short wave radiation	206	200	-6
Net long wave radiation	-100	-85	15
Latent Heat	-101	-101	0
Sensible Heat	-14	-15	-1
Net heat flux	-9	-1	8

Figure 3.4 shows the monthly SST of *SEAS_UO_as1*. It is evident that the Mediterranean Sea continues to lose heat from January to March. The coldest areas of the SEAS are the northern Adriatic Sea due to its shallow depth and the Black Sea, where it cools rapidly in September. In 2021, the Mediterranean Sea reached its

maximum temperature in August with average values larger than 30°C in the Levantine Sea and values between 29-30°C in the central Mediterranean Sea.

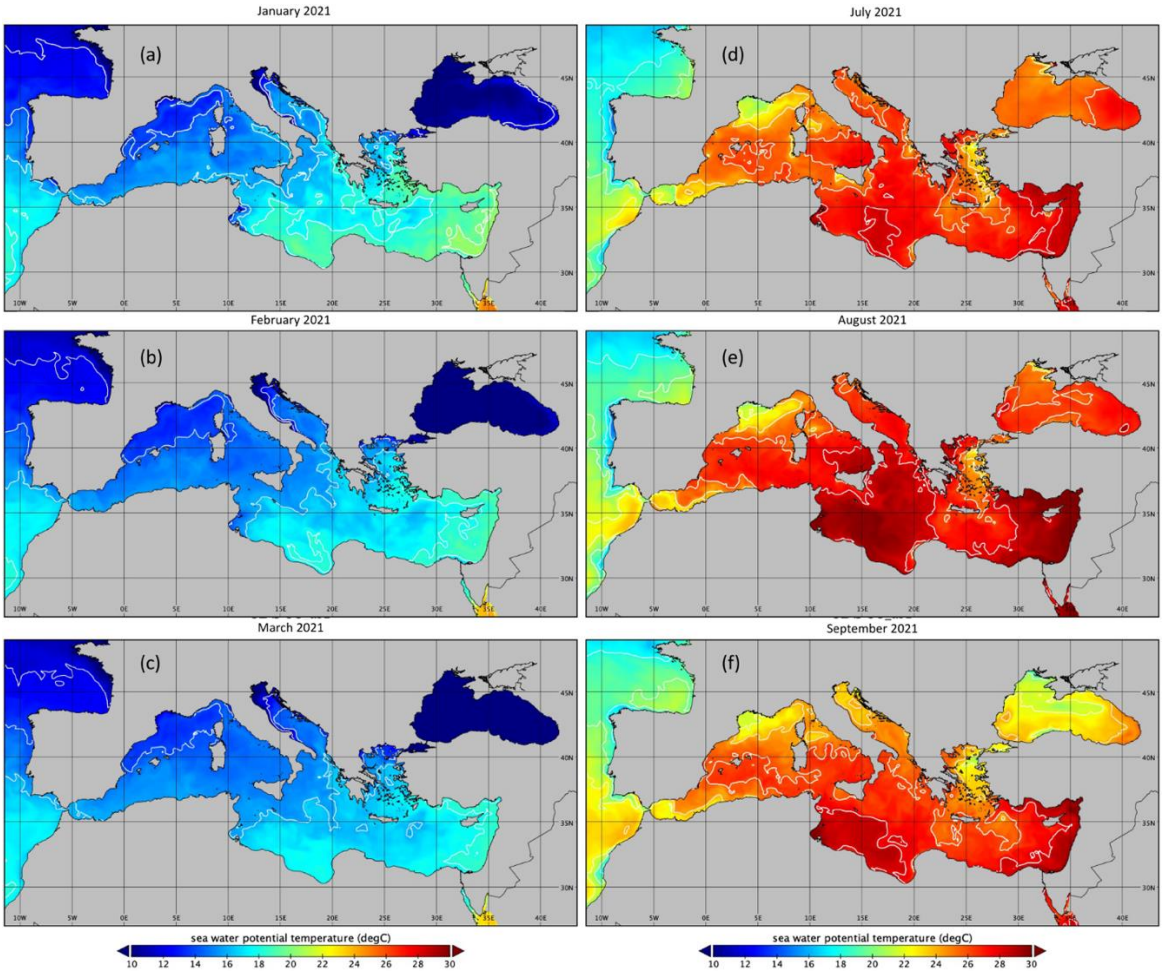

Figure 3.4: SST monthly mean calculated by the uncoupled SEAS model (UO_as1 setup) in the winter period (a,b,c) and summer period (d,e,f) of 2021. Isolines are every 2 degC.

To partially interpret the SST in Figure 3.4, we can now consider the heat fluxes shown in Figure 3.5 and Figure 3.6, the latter as a time series of the basin-averaged values.

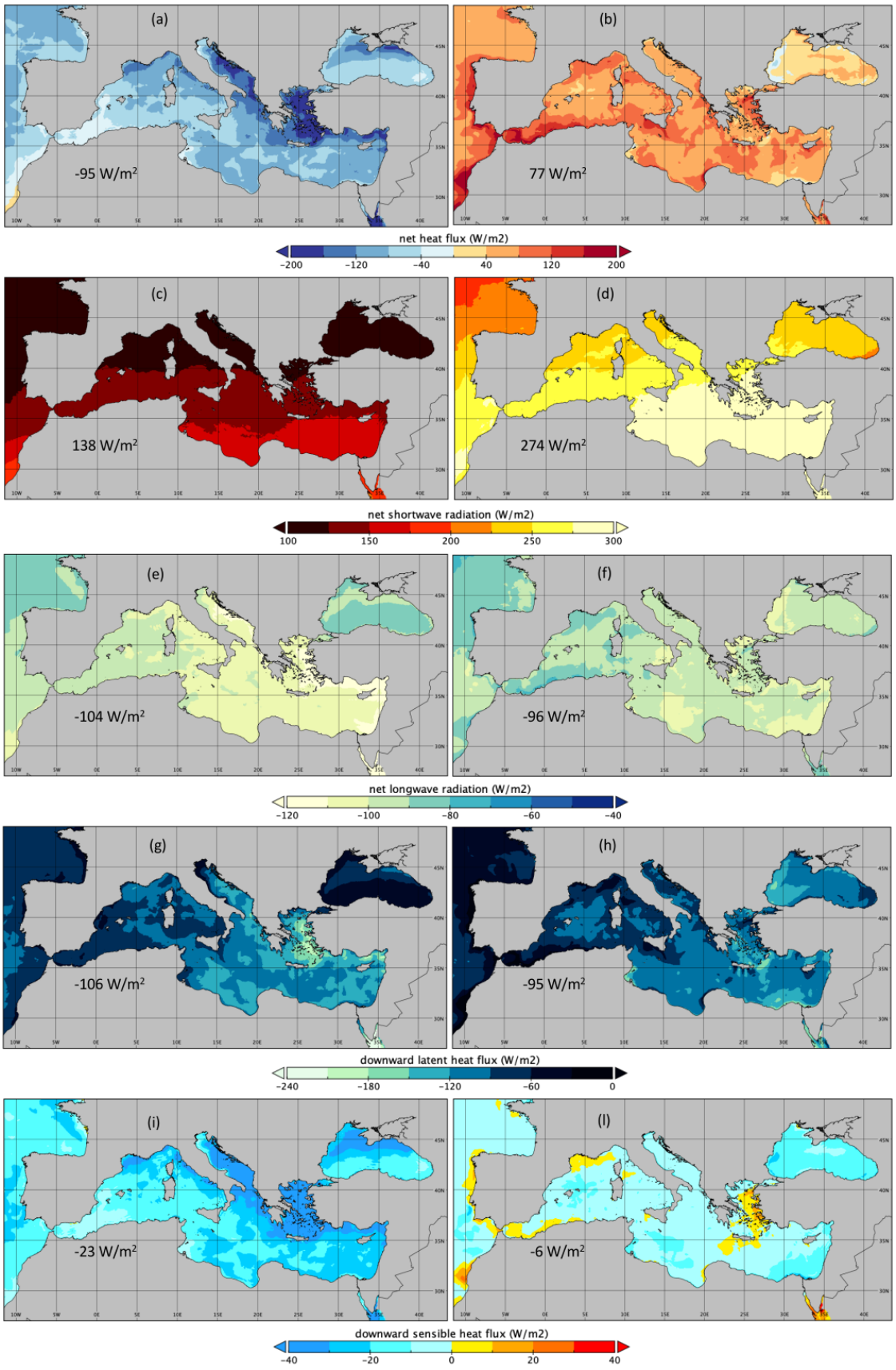

Figure 3.5: Average heat fluxes from the uncoupled SEAS model (UO_as1 setup) in the winter period (left column) and summer period (right column) of 2021.

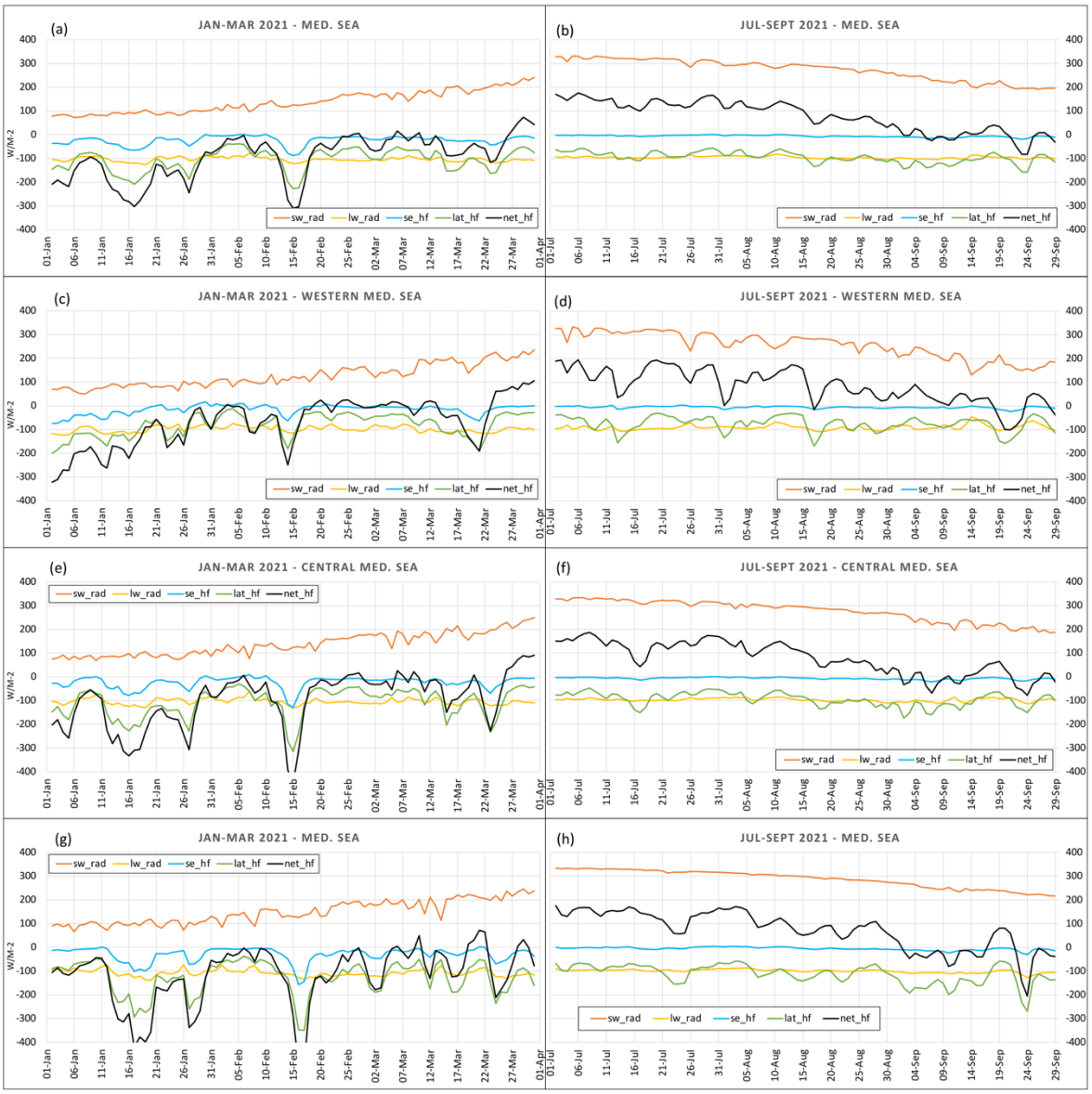

Figure 3.6: Time series of the basin-averaged heat fluxes for the Mediterranean Sea (first row), for the Western Med. Sea, (second row), for the Central Med. Sea (third row) and for the Eastern Med. Sea (fourth row) and left and right column respectively for the winter and summer period of 2021.

The average net heat budget for SEAS (Figure 3.5a,b) is negative in the first three months of the year and positive in summer period, and the time series (Figure 3.6a,b) shows that the Mediterranean Sea starts to gain heat at the end of March to the beginning of September, with minor differences in timing and values among sub-basins.

The heat source for the ocean is solar radiation (Figure 3.5c,d), which is also responsible for the trend in net heat flux trend (Figure 3.6a,b, black line). During winter, this balance is largely modified by variations in latent heat and secondarily by sensible heat caused by intense meteorological events. The net longwave radiation flux (i.e., the difference between downward longwave radiation from the atmosphere and upward from the ocean) is almost the same in both periods (Figure 3.5e,f) and shows no seasonal trend (Figure 3.6a,b).

The large values of latent heat (Figure 3.5g,h) confirm that the Mediterranean Sea is an evaporative basin and this process is more intense in winter when the average wind speed over the basin is greater (Figure 3.1e). In addition, large amounts of latent heat are extracted, especially in particular in the central and eastern Mediterranean, during intense meteorological events (Figure 3.6e,g). This point will be discussed in more detail later.

The sensible heat depends on the temperature difference between the sea surface temperature and the temperature in atmospheric boundary layer and on average, reaches smaller values than the other fluxes. The positive temperature difference is larger in winter when northerly cold air masses are advected over the central and eastern Mediterranean (Figure 3.7a) causing the ocean to lose heat (Figure 3.5i). During summer, this difference is smaller but still positive, mainly because of the diurnal cycle of air temperature, absent in the SST. However in upwelling regions, such as along the Aegean coast of Turkey, the temperature difference reverses (Figure 3.7b), and the sensible heat flux is downward from the atmosphere to the ocean (Figure 3.5l). A more detailed analysis is needed for the other regions in summer.

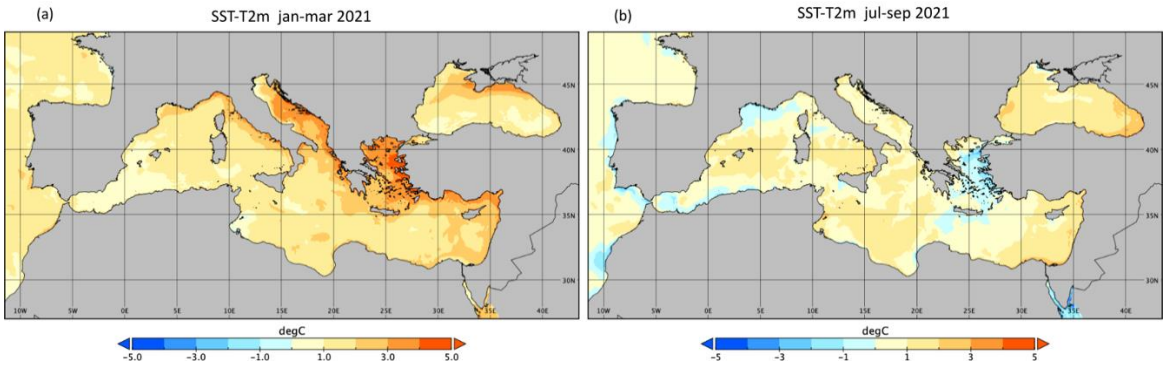

Figure 3.7: Average difference between forcasted SST and prescribed 2 meters air temperature in the period January-March 2021 (a) and July-September 2021 (b).

The heat fluxes during two intense events were analysed in more detail (Figure 3.8).

In the first case, from 12 to 20 January 2021, the atmospheric conditions showed intense Mistral winds in the Gulf of Lion that extended to the central Mediterranean Sea. In the second case, from 14 to 17 February 2021, the atmospheric circulation was northerly and intense in the central and eastern Mediterranean Sea. The wind speed in Figure 3.8a,e is calculated from the wind components at each forecast time step and then averaged for the above periods.

In the first period, when the strongest winds are in the Gulf of Lion, most of the net heat flux (Figure 3.8b) is lost in the Aegean Sea, mainly by latent heat (Figure 3.8c) and secondarily by sensible heat (Figure 3.8d). This is because the latent heat is related to the specific humidity of the air and the specific humidity of air saturated at the water temperature, which differ between the Gulf of Lion and the Aegean Sea.

In the second event (14-17 February 2021) the intense northerly winds in the Aegean Sea (Figure 3.8e) had different characteristics than in the first event. In this event, a larger amount of heat (700-750 Wm^{-2}) was extracted from the sea (Figure 3.8f), due to the latent heat component reaching values of about 400-450 Wm^{-2}, and the sensible heat component up to 250-300 Wm^{-2}(Figure 3.8g,h), which is due to large temperature differences between air and sea.

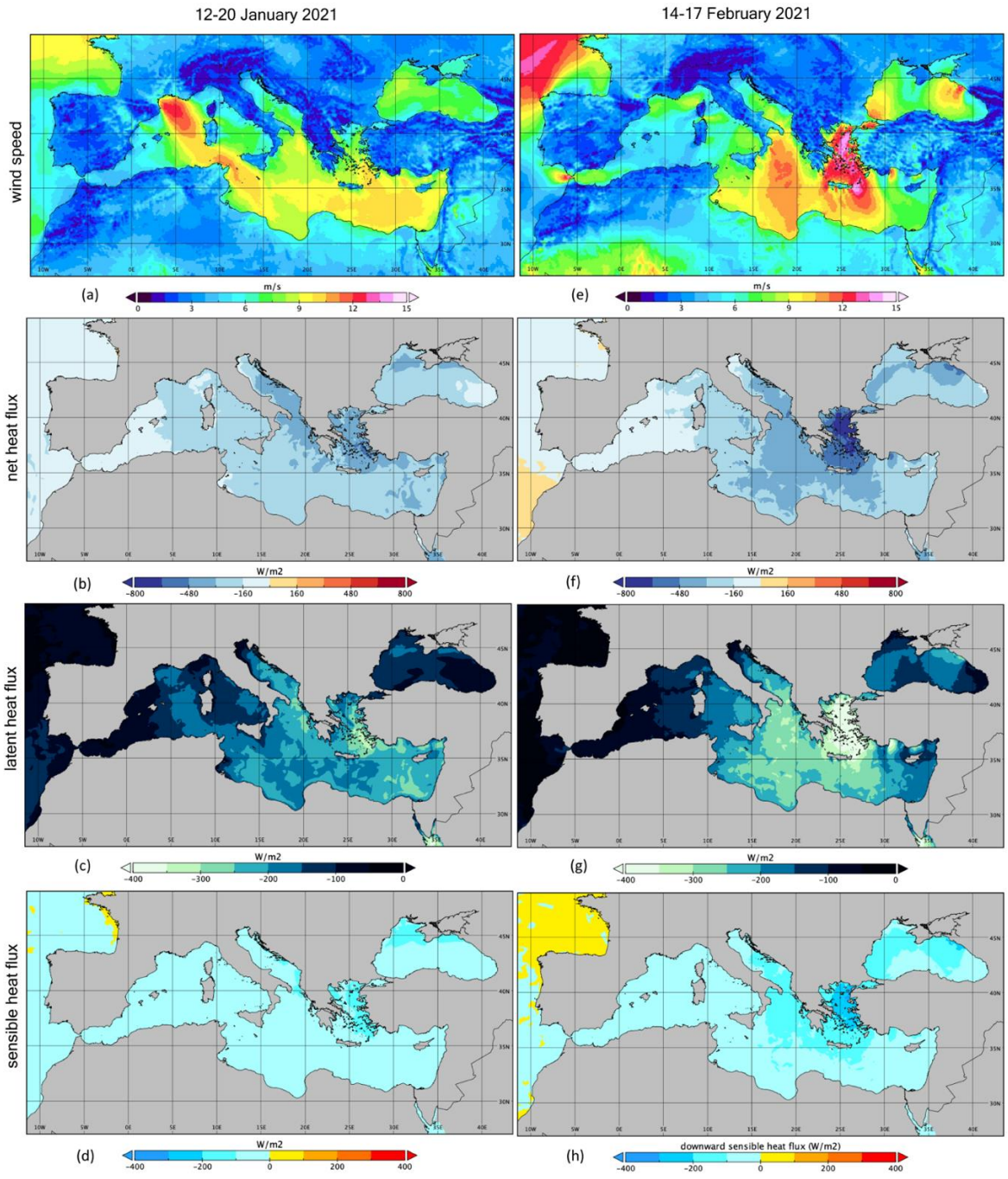

Figure 3.8: Wind speed, net, latent and sensible heat fluxes averaged in the period 12-20 Jnuary 2021 in the first column, and in the period 14-17 February 2021 in the secound column.

3.5 Conclusions

Short-term forecasting experiments were conducted with the SEAS uncoupled ocean model for two seasonal periods from January to March 2021 and from July to September 2021. In these experiments the forecast skills were evaluated as a function of the air-sea physics parametrizations, particularly the radiative components of the surface heat flux. The forecasts for the two seasons are useful to understand to the statistics of the scores and try to relate them to the different heat fluxes.

Each forecast is initialized every 5 days from a merging of analyses from three different operational systems. Each model run consists of one day of spin-up time and 5 predicted days, so that the forecast of each period is a concatenation of multiple 5-days forecasts. Two different configurations for the heat fluxes were tested: *SEAS_UO_as1* uses the MFS bulk formulae described in 1.1.1.1, while *SEAS_UO_as2* uses the downward radiative fluxes (solar and longwave) prescribed from the ECMWF forecasts.

Briefly, the main results are:

- The two SEAS configurations show similar results, and the forecast skills are close to those of MFS. This means that the formulations of the radiative fluxes in the MFS bulk formulae are still a valid approximation. The main difference between the MFS and ECMWF prescribed radiative fluxes arises from the longwave downward component, which on average produces a net heat flux 22 Wm^{-2} greater than that calculated with the MFS bulk formulae. The use of this radiative component directly from ECMWF should be carefully considered before operational implementation.
- The net longwave radiative flux is negative (-90 Wm^{-2}) at the basin scale and does not vary relevantely between seasons, an issue that should be investigated further in the future.
- The comparison with MFS analyses shows that a longer spin-up time would be required for better performances in the Atlantic, since the initial conditions of the parent domain are only half-resolved.

- In 2021, the Mediterranean Sea lost heat from the beginning of the year until the end of March, when SST was at its lowest, and began losing heat again in mid-September after the SST reached its maximum in August.
- Large heat flux anomalies can last for several (4-10) days and are determined by meteorological events that first increase latent heat and second increase sensible heat. The SST change depends on the duration of the event, which determines the total amount of heat lost, and on the initial SST.
- The turbulent heat fluxes depend on the characteristics of the air masses blowing over the ocean. We have found that in the Aegean Sea a combination of latent and sensible heat fluxes can result in a net loss of 700 Wm^{-2}, similar to that normally experienced during deep-water events in the western Mediterranean Sea.

With respect to the SEAS coupled system, an important insight emerges from the analysis of the magnitude of the heat fluxes. It is argued that the prescription of the radiative components of the heat flux by the atmospheric model still requires careful calibration and investigation. In the Mediterranean Sea, where the water vapor content of the air is large in the summer, it is recommended that the longwave radiative flux be evaluated and probably corrected during coupling.

Considering the SST validation results and the time series of turbulent heat fluxes, it is reasonable to calculate these fluxes in the ocean model, even in the coupled system. The feedback to the atmosphere can be either indirect and delayed by the SST exchange or direct by the transfer of the turbulent fluxes.

Chapter 4

Preliminary coupled modelling for the simulation of an extreme event

In the second chapter, the results of the uncoupled ocean and atmospheric models were shown for the simulation of Medicane Ianos. In this chapter, the SEAS coupled model is presented and used to simulate the dynamics of the atmosphere and ocean during the same extreme event. A preliminary coupling setup is used and described in section 4.1, the comparison of some dynamical variables with the uncoupled experiments is shown in section 4.2, and finally the simulation skills of both components in the coupled configuration are discussed in section 4.3.

For clarity, it should be noted that this experiment is not a forecast because the lateral boundary conditions are forced by both atmospheric and oceanic analyses.

In what follows, the ocean and atmospheric models described in the past chapters are referred to as components of the SEAS coupled system, and OASIS3-MCT will be referred to as the coupler for brevity. The name of the experiment is *SEAS_COUPLED* and the results of the ocean and atmospheric components are called *SEAS_COUPLED_OCE* and *SEAS _COUPLED_ ATM*, respectively.

4.1 The coupling framework and the variables exchange

The models are coupled using the OASIS3-MCT library described in 1.1.3, which is already implemented in the NEMO and WRF codes and has been used in several recent works (Samson et al., 2015, 2017, Renault et al., 2019, Jullien et al., 2020). In this work, the same computational grid is used by the atmosphere and ocean components on the domain of Figure 4.1, a condition that ensures the conservation of the exchanged variables since no re-gridding is required.

The coupling performed in this work should be considered preliminary because, for now, the traditional data exchange between ocean and atmospheric models, as described in Table 4.1, was used. This coupling framework uses an atmosphere-driver approach, i.e., the turbulent heat fluxes and wind stress are calculated in the atmospheric model and then transferred to the ocean, which in turn returns the modified SST and currents to the atmospheric model.

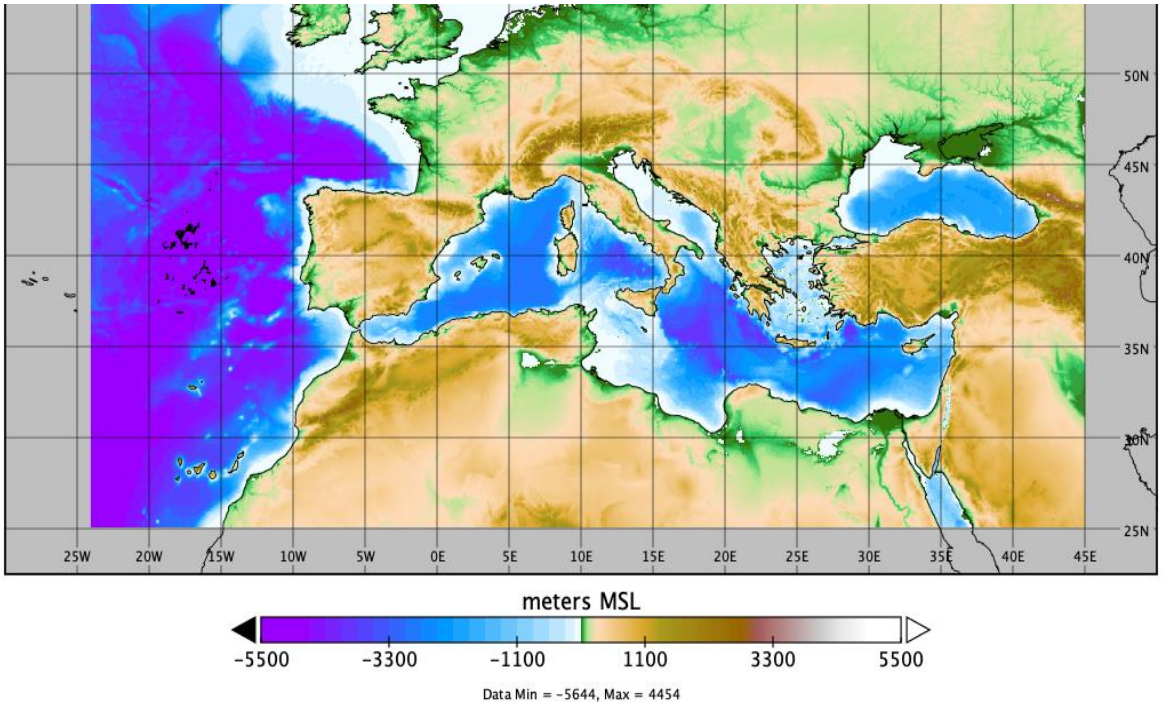

Figure 4.1: SEAS topo-bathymetry

Table 4.1: exchanged variables in the SEAS coupled model.

OCE→ATM Coupling freq.: 30mins	SST Surface ocean currents
ATM→OCE Coupling freq.: 30mins	Net solar radiation Net non-solar heat flux, sum of: • downward longwave radiation emitted by the atmosphere • upward longwave radiation emitted by the ocean • upward latent heat • sensible heat Net mass flux: evaporation-precipitation Wind stress components

Pullen et al. (2017a) propose an *ocean-driver* coupling strategy in which the turbulent heat fluxes and wind stress are calculated in the ocean model and transferred to the atmospheric model. The reason is that in the atmospheric models, the turbulent heat fluxes are calculated by the boundary layer scheme (BL), which often uses complicated non-local PBL parameterizations along with stability functions that are specifically derived over land instead of water in most cases. In addition, the development of the oceanic models over the past 30 years has led to the implementation of bulk formulae that include parameterizations for marine boundary processes not represented in many atmospheric BL (Rosati and Miyakoda 1988, Bignami et al., 1995) These include the effects of sea spray, skin temperature effects, or rainfall effects on surface fluxes and changes in drag coefficients in strong and weak wind regimes (Kondo, 1975, Fairall et al., 1996, 2003, Large, 2006).

The ocean-driver approach may have problems with enthalpy and mass conservation. This can be addressed with specific modifications to the BL schemes to account the turbulent heat fluxes from the ocean model and change the vertical heat transfer in the atmospheric column accordingly. It should be noted that without these changes, the SST feedback to the atmosphere reduces the enthalpy imbalance with some delay, which can be further reduced by increasing the coupling frequency. This assumption can be considered and tested in future coupled ocean-atmosphere short-

term forecasts, keeping in mind that the energy imbalance is restored at each forecast initialization.

The atmospheric model setup is the same as *UA_as5_UO* described in **Error! Reference source not found.**, i.e., the one that calculated the net heat flux closest to that of the ocean model one in the uncoupled simulations of medicane Ianos.

The fluxes of momentum (τ), sensible (*SH*) and latent heat (*LH*) are calculated in the surface boundary layer as follows:

$$\tau = \rho u_*^2 = \rho C_d U^2 \quad (4\text{-}1)$$

$$SH = -\rho c_p u_* \theta_* = -\rho c_p C_h U(\theta_a - \theta_s) \quad (4\text{-}2)$$

$$LH = \rho L_e u_* q_* = \rho L_e M C_q U(q_s - q_a) \quad (4\text{-}3)$$

where θ_* and q_* are the potential temperature and moisture scales respectively, u_* is the friction velocity, c_p is the specific heat capacity, U is the wind speed in the first model layer increased by a convective velocity (Beljaars, 1995), L_e is the latent heat of vaporization, M is the available moisture at the surface, θ_a and θ_s are the first layer and surface potential temperature respectively, q_s and q_a are the saturated specific humidity at the surface and the first layer specific humidity respectively. Over the ocean M=1, $\theta_s = SST$ and U is the wind speed relative to the ocean. The dimensionless bulk transfer coefficients C_d, C_h, C_q are calculated using the Monin-Obukov similarity theory and the details of the empirical stability functions can be found in Jiménez et al., (2012).

4.1.1 Initialization

At the initial time of the simulation (2020-09-15:00:00) both components of the coupled system must be initialized, as well as the exchanged variable in the coupler.

The oceanic component is initialized with T/S, currents and SSH from the three-hourly outputs (average 00:00-03:00) of the uncoupled experiment *UO_as1* which also provides the initial fields of SST and surface currents for the coupler. The atmospheric component is initialized from ECMWF analyses as in *UA_as5_UO*.

A special coupled experiment was performed to generate the initial fields of the variables sent to the ocean component, specifically the heat fluxes and net longwave

radiation, since the shortwave radiation is zero throughout the domain at 00UTC. In this experiment the exchanged fields were initialized to zero, the coupling frequency was set to 2 minutes and the ocean time step was reduced from 180 to 60 seconds, while the atmospheric model time step remained at 20 seconds. The simulation lasted 1 hour and after several coupling time steps, the exchanged fields stabilized and the values of the last coupling time step (+1h) were used to initialize the atmospheric fields.

4.2 Results and comparison with the uncoupled experiments

In this section, the results of the coupled ocean-atmosphere simulation SEAS_COUPLED of the medicane Ianos are presented and compared with the uncoupled experiments presented in the Chapter 1.

Specifically, the results of *SEAS _COUPLED_ ATM* are compared with the uncoupled experiment *UA_as5_UO*, which has the same physical setup (**Error! Reference source not found.**). This is done to only identify the differences due to the updating of the SST and the ocean current. Similarly, the results of *SEAS _COUPLED_OCE* are compared to the uncoupled experiment *UO_as3* forced with an uncoupled WRF experiment, to determine the differences due to the wind stress and surface fluxes updates.

4.2.1 SEAS coupled ocean simulation

The average SST in the simulated period from 15 to 18 September 2020, is shown in Figure 4.2a where the footprint of Ianos is still visible despite the 4-day average, where the SST is lower than in the surrounding areas. Later, its path toward the island of Crete contributed to further reduce the SST in the Aegean Sea. The SST differences from the uncoupled experiment *UO_as3* (Figure 4.2b) are large in the central Mediterranean Sea, which is associated with the Ianos medicane development, but they are not the only ones.

A negative SST difference is observed in a large area near the Gulf of Sidra where Ianos developed, suggesting that the coupled model extracts more heat from the ocean than the uncoupled experiment during the early phase of the cyclone. In the Ionian Sea, where Ianos reached its maximum intensity on days +3 and +4, the difference is alternating positive and negative in small areas, suggesting that the interaction with the atmosphere was larger in the coupled experiment. These temperature differences can be explained by the map of the net heat flux from the atmosphere to the ocean and its difference from the uncoupled *UO_as3* experiment (Figure 4.2c,d). In general, the coupled experiment extracts more heat from the ocean than the uncoupled simulation over the entire Mediterranean Sea.

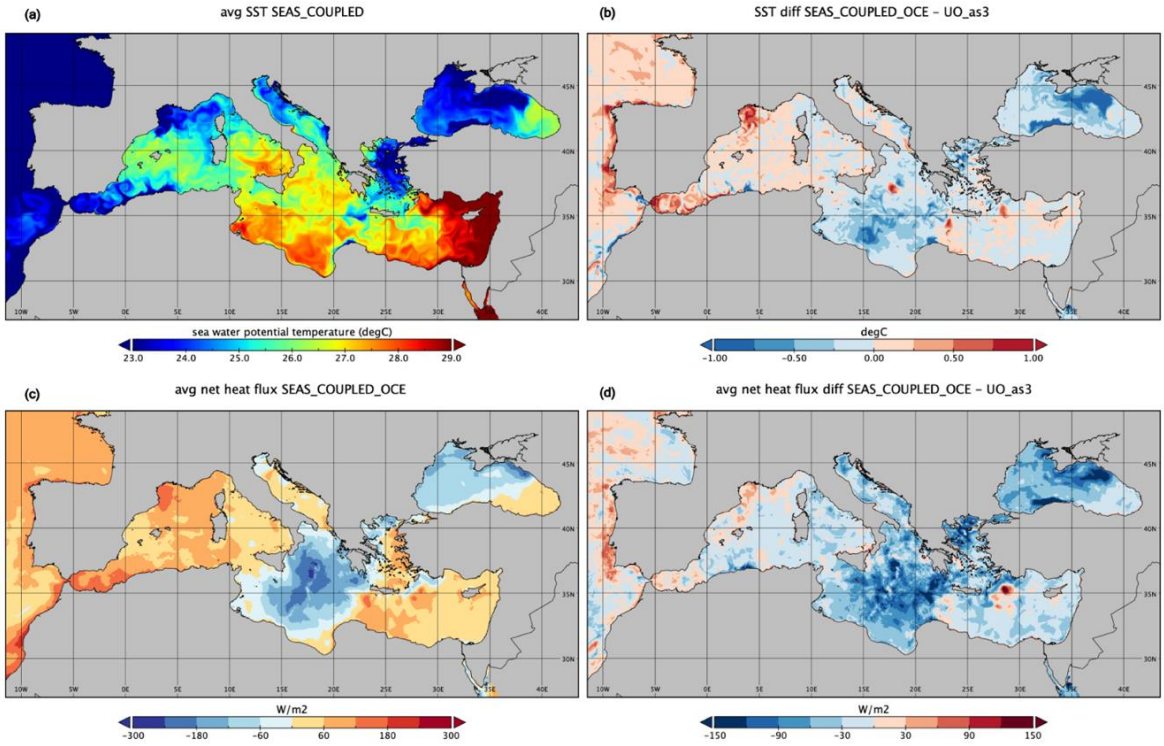

Figure 4.2: in the first column the average SST (a) and net heat flux (c) of the SEAS_COUPLED_OCE experiment and differences (b), (d) with the uncoupled experiments UO_as1 in the second column.

The positive SST differences in the Guld of Lion and in the Alboran Sea indicate that the warmer SST is due to a larger positive net heat flux (heat enters the ocean), while in the central Mediterranean and Black Sea the areas of colder SST correspond to larger heat losses. The average net heat flux of the Mediterranean basin during this period for the coupled experiment is about 10 Wm^{-2}, which is lower than the net heat flux of 44 $Wm^{-2}$of the uncoupled experiment *UO_as3* (Table 2.2). Therefore, the SST is lower in the coupled model in a large part of the basin with respect to the uncoupled simulation. This is because in *UO_as3* the larger radiative fluxes (from *UA_as5_UO*) are not balanced by a larger heat loss due to the turbulent heat fluxes.

The wind stress caused by the cyclone alters the average surface current field mainly in the Ionian Sea during the three days with the highest intensity of the event (16-18 September 2020), after which the circulation returns to its climatology. Outside this area, the most common features of the average circulation (Pinardi et al., 2015) persist during the event: the Atlantic-Ionian Stream, the Gulf of Lion Gyre, the Western Adriatic Coastal Current, the Southward Cyclades Current and the western flank of the Rhodes Gyre (Figure 4.3a,b).

Comparison of Figure 4.3a and Figure 4.3b shows the difference in surface circulation only for September 17, when Ianos strengthened over the Ionian Sea before landfall on the Ionian Islands. The south-westward intense circulation results from the effects of the wind stress of the previous day and the cyclonic pattern of September 17 (Figure 4.3c) and shows a divergent asymmetric pattern that develops in the calm eye of the cyclone aloft.

The differences between the surface circulation and the uncoupled *UO_as3* experiment (Figure 4.3b) are very small because the wind forcing is very similar (Figure 4.3d), and this means that *UA_as5_UO* is a good approximation of a coupled system for this intense event.

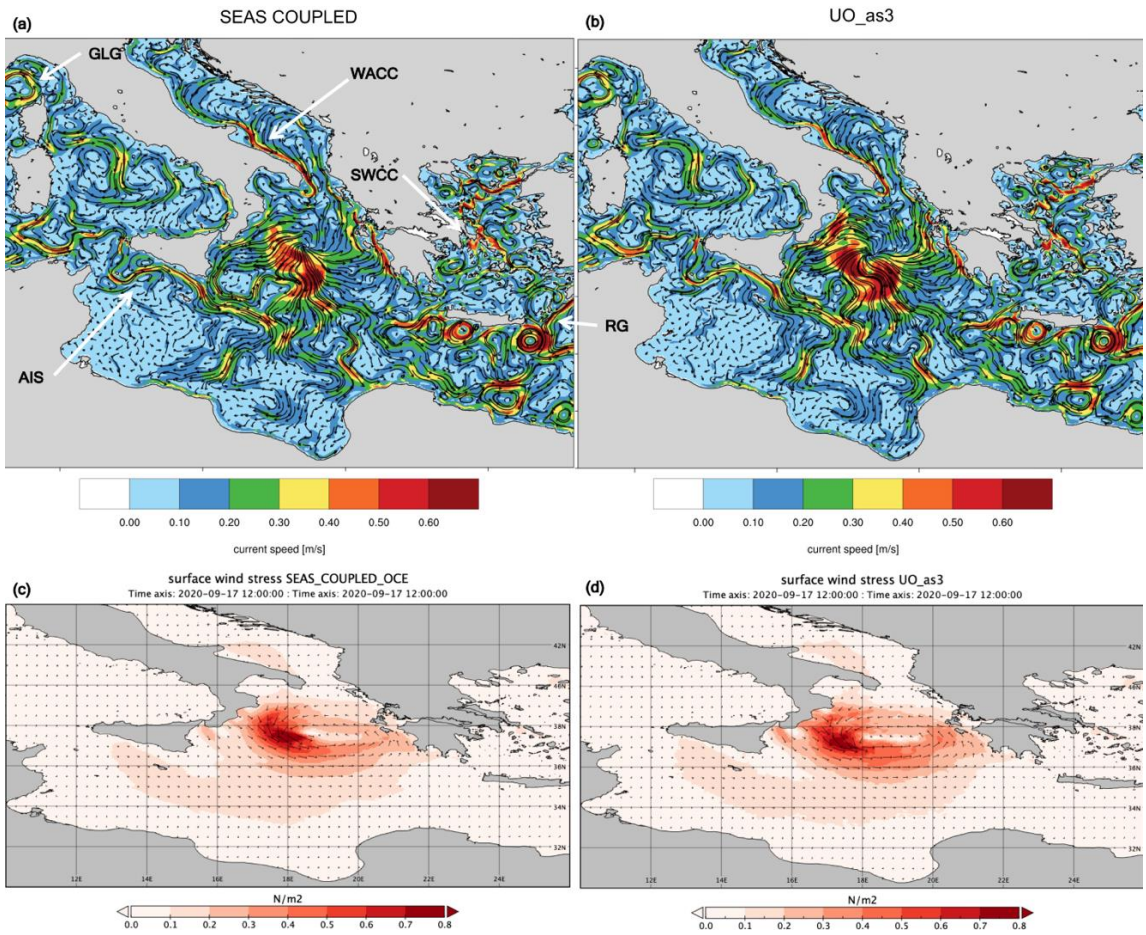

Figure 4.3: Upper row the average surface circulation of the day 17 September 2020 in the SEAS_COUPLED_OCE experiment (a) and UO_as1 experiment (b). GLS is the Gulf of Lion Gyre, AIS is the Atlantic-Ionian Stream, WACC is the Western Adriatic Coastal Current, SWCC is the Southward Cyclades Current and RG is the western flank of the Rhodes Gyre. In the second row the wind stress module for the same day and experiments.

The wind stress averaged over the Mediterranean basin is 0.067 N/m^2, which is about 6% less than 0.071 N/m^2 in *UO_as3* while the wind speed between the two experiments is almost the same at 5.5 m/s. The reasons for this are, first, the nonlinearity of the relationship between wind speed and stress, and second, the different methods used to calculate the wind stress: the similarity theory in the atmospheric boundary layer in *SEAS_COUPLED_ATM* and the Hellerman & Rosenstein (1983) formulation in the MFS bulk formulae in *UO_as3*.

It is reasonable to assume that the different formulation of the wind stress may lead to a different magnitude of the mean Mediterranean circulation. For this reason, longer and more robust statistics are needed to determine whether the coupling changes the predicted magnitude of the surface circulation in the long term.

4.2.2 SEAS coupled atmosphere simulation

The results of *SEAS_COUPLED_ATM* are compared with the uncoupled experiment *UA_as5_UO*, which has the same physics setup, to determine the differences due to the update of SST and ocean current. The simulations are validated by comparing the model with ECMWF analyses surface pressure (Figure 4.4a,b), the 10m wind field from scatterometers data (Figure 4.4c,d), and accumulated precipitation from in situ data (Figure 4.4e,f). The wind fields are from the Global Ocean Hourly Sea Surface Wind and Stress from Scatterometer and Model dataset for September 18 at 00 UTC (+72h), before Ianos landfall in the Ionian Islands. Precipitation is analysed at the end of the simulation (19 September 00 UTC, +96h) and compared with the total precipitation map produced by Lagouvardos et al. (2022).

The coupled ocean model simulation does not enhance the pressure minima (Figure 4.4a,b,c) in the core of the cyclone, which is larger (998 hPa) than the uncoupled experiment (993 hPa) and the best estimate (995 hPa). Looking at the evolution of the surface pressure minima (not shown) the coupling do not affect the cyclone track in the Ionian Sea as much as choosing two different physics setup in the uncoupled runs (Figure 2.6), and this finding is also confirmed in Bouin and Lebeaupin Brossier (2020). Conversely, the positioning and timing of the cyclone landfall has improved, and at 2020-09-18 00UTC it is located over the island of Zakynthos, slightly further south (less than one degree) with respect to the position in the ECMWF data.

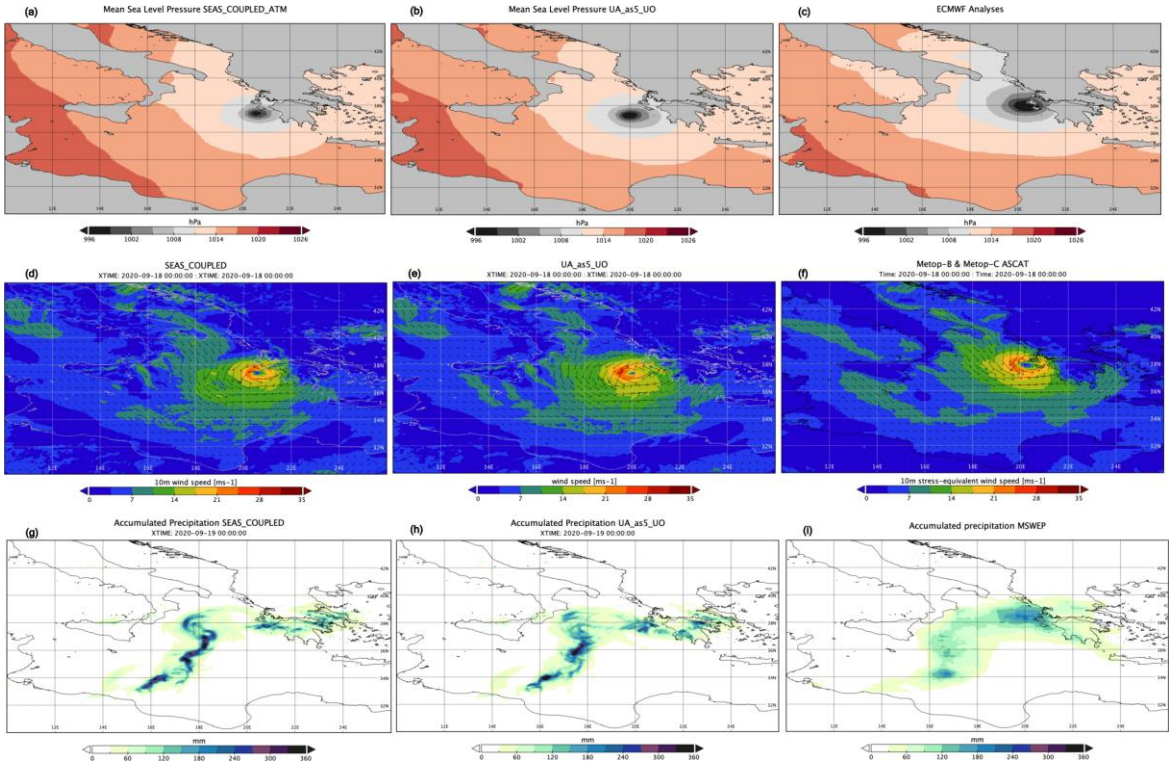

Figure 4.4: Mean sea level pressure (a,b), 10m wind (d,e) and cumulated rainfall (g,h) fields in the SEAS_COUPLED and UA_as5_UO experiments, respectively in the first and second column. In the third column the best estimates of the reality: ECMWF analyses (c), blended scatterometer data(f) and MSWEP merged data (i).

In the *UA_as5_UO* experiment, the cyclone is at the same position three hours later. Due to the higher value of the mean sea level pressure minimum, the magnitude of the wind field is slightly smaller in the coupled run (Figure 4.4d,e), but agrees well with the ECMWF analyses in magnitude and shape of the cyclone (Figure 4.4f).

The pattern of the accumulated precipitation does not change between the two experiments (Figure 4.4g,h) because the path of the cyclone core is very similar and agrees with the spatial distribution of the MSWEP reference dataset (Beck et al. 2019, Figure 4.4i), although over the ocean the values are larger. Over the land, if we consider the observations reported in Lagouvardos et al. (2022), both experiments fail in reproducing the heavy rainfall in the Central Greece, because the calculated trajectory of the cyclone is slightly southward displaced, although the values have comparable magnitude.

As regards the heat fluxes, the *SEAS_COUPLED* experiment has the same basin-averaged values on the *UA_as5_UO* uncoupled experiment listed in Table 2.2, since the

SST prescribed in *UA_as5_UO* is very close to that in SEAS_COUPLED_OCE. Some differences in the shortwave and latent heat fluxes occur locally in the Ionian Sea (Figure 4.5b,f), but are compensated at the basin scale. The differences in the latent heat flux are related to the different wind speed: the red areas in Figure 4.5f indicate lower upward (negative) latent heat loss in *SEAS_COUPLED*, which correspond to the blue areas in Figure 4.6 where the average 10m wind speed is lower than in *UA_as5_UO*. The decrease of the average wind magnitude in *SEAS_COUPLED* with respect to *UA_as5_UO* can be attributed to the lower intensity of the cyclone due to a lower heat loss from the ocean. This a well-known effect of the ocean-atmosphere coupling (Pullen et al., 2006, 2007; Rainaud et al. 2017, Ricchi et al., 2019). A slab ocean behaves like an infinite source of heat for the atmosphere, whereas in an interactive ocean the SST cooling is more rapid and intense due to the coupled atmospheric fluxes. In turns, the lower ocean-atmosphere temperature difference reduces the heat fluxes, thus the cyclone intensity. Regarding the differences in the shortwave radiation, the cloud fraction (%) was calculated for the low-clouds (300-2000m), the mid-clouds (2000-10000m) and the high-clouds (>10000m). The differences between the two experiments in the mid and high clouds fraction (where the cloud cover is larger) partially explain the differences in the shortwave radiation, so this aspect should be further investigated with respect to any differences in the water content in the atmospheric column.

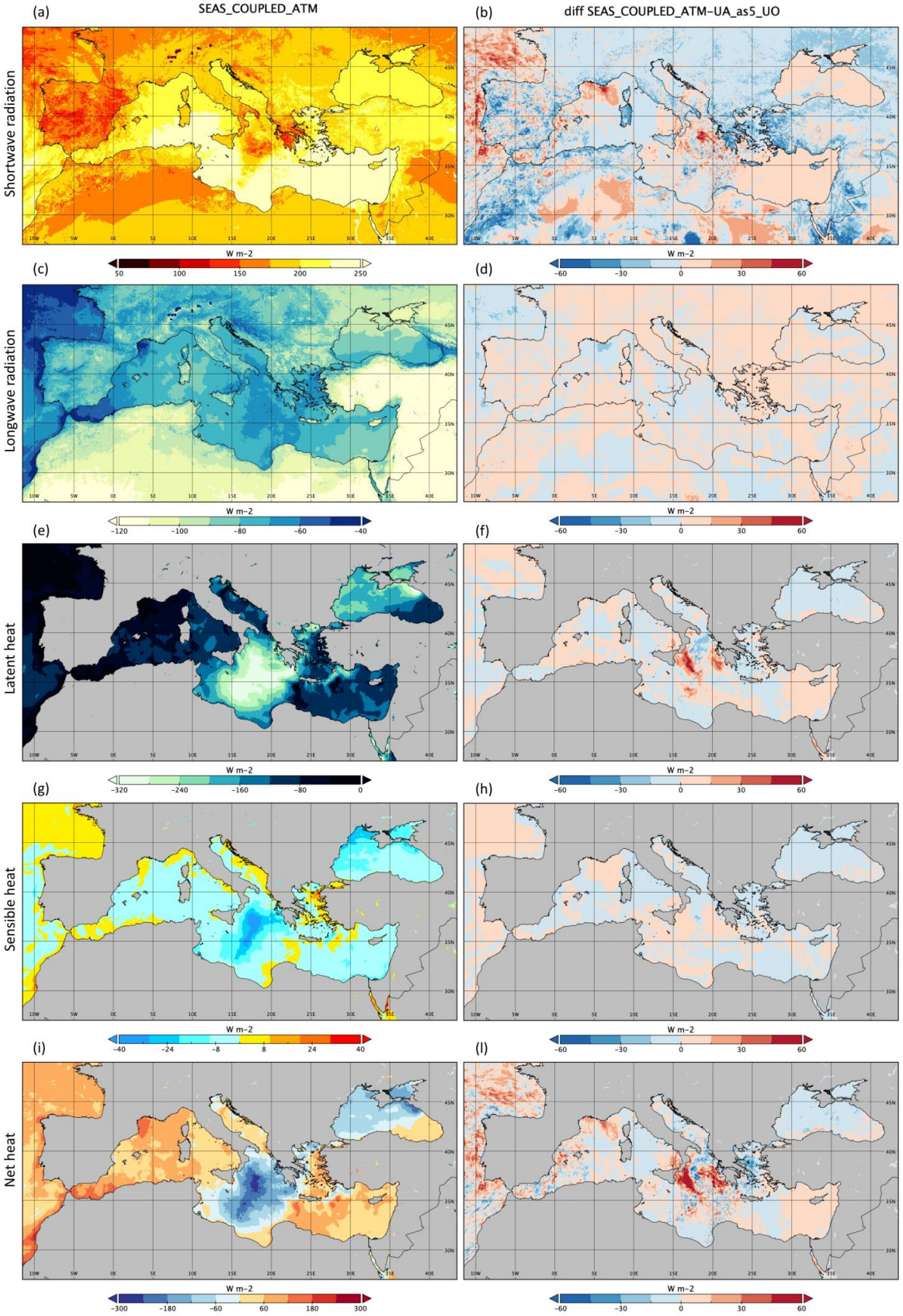

Figure 4.5: First column the heat fluxes and the net one for the SEAS_COUPLED experiment, and the difference with the UA_as5_UO experiment in the second column.

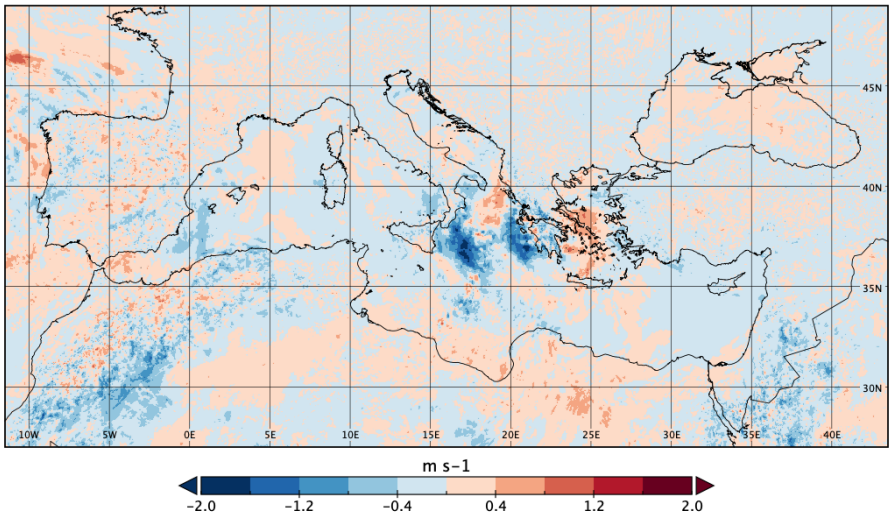

Figure 4.6: average 10m wind speed difference SEAS_COUPLED_ATM-UA_as5_UO

4.3 Skills of the coupled experiment

The skills of the coupled experiment *SEAS_COUPLED* have been evaluated quantitatively for the SST and the 10m wind speed. The reference datasets are the same as those used to evaluate the skills of the uncoupled experiments, i.e., the remotely sensed multisensors SST_MED_SST_L4_NRT_OBSERVATIONS_010_004 and WIND_GLO_PHY_L4_NRT_012_004 which were regridded to the model target grid with a bilinear interpolation.

The statistical metrics are:

$$BIAS = \frac{\sum_{i=1}^{N}(X_{mod,i} - X_{obs,i})}{N} \qquad RMSD = \sqrt{\frac{\sum_{i=1}^{N}(X_{mod,i} - X_{obs,i})^2}{N}} \qquad (4\text{-}4)$$

where X is alternatively the SST and the 10m wind speed and N is the total number of valid grid points in the Mediterranean basin from the Strait of Gibraltar to the Strait of Dardanelles.

4.3.1 SEAS_COUPLED_OCE

It is well known that the introduction of feedbacks between the atmosphere and the ocean, together with different parametrizations of the heat fluxes, generally leads to a degradation of the predictive capabilities of a coupled model compared to a long-tested and robustly calibrated uncoupled model. The same happens with *SEAS_COUPLED_OCE*, but this degradation is not so large, considering also the fact that the experiment is driven by atmospheric and oceanic analyses, and has a relatively short duration. The SST BIAS at the basin scale is negative of the order ot -0.10°C (Figure 4.7a) which is similar to the *UO_as1* which uses the MFS bulk formulae validated over long period of time in the MFS, but slightly worse than *UO_as3,* which is forced with the same atmospheric model. Interestingly, the BIAS, compared to the uncoupled experiments, is lower in the area of the medicane development where the interaction with the atmosphere is more intense than the rest of the basin and oscillates around zero (Figure 4.7b). This is due to both lower deviations from the SST

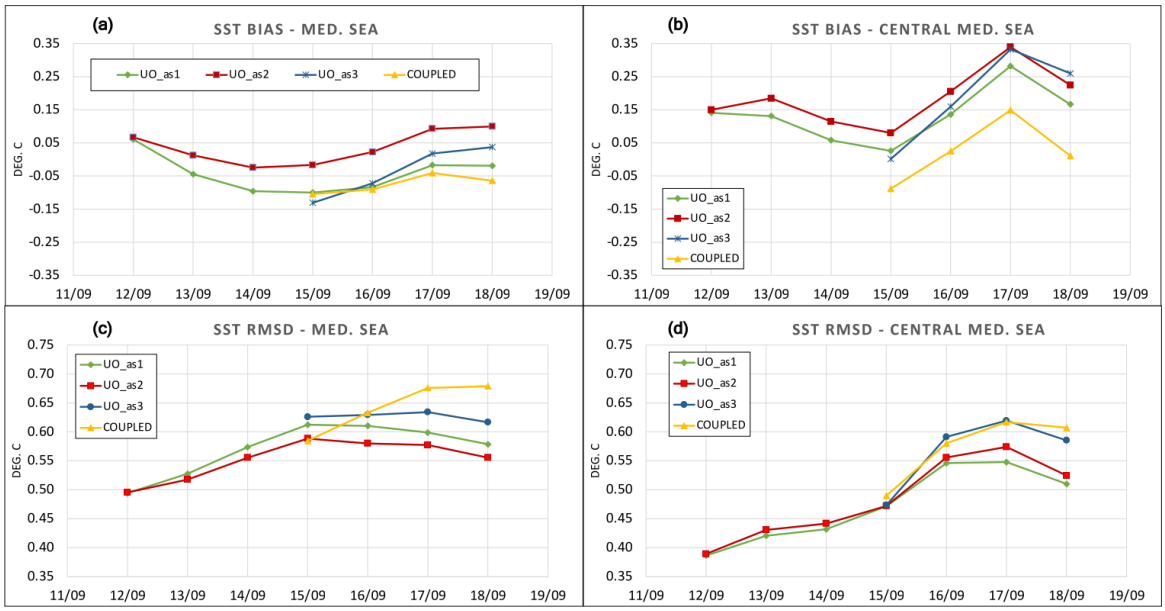

Figure 4.7: BIAS and RMSD in the Mediterranean Sea basin and in the Central Mediterranean Sea (black box inFigure 4.8) respectively in the first and second row

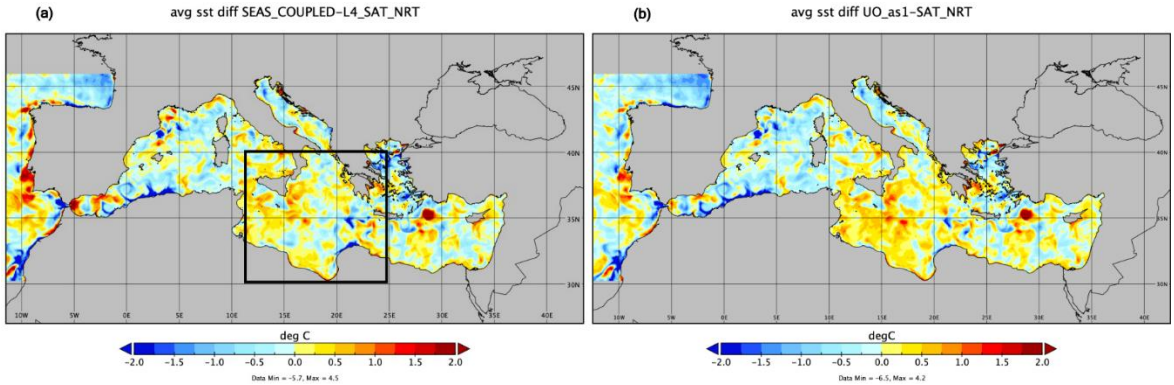

Figure 4.8: SST difference between SEAS_COUPLED_OCE (a) or UO_as1 (b) and remote sensed SST

observed field and the simultaneous presence of regions of positive and negative bias showed in Figure 4.8a,b.

This cannot be considered a real improvement since it is not supported by a reduction of the RMSD in the same area, which has the same magnitude and evolution as *UO_as3* (Figure 4.7d).

In summary, the deterioration of the skill of the *SEAS_COUPLED_OCE* becomes more evident with the RMSD at basin scale (Figure 4.7c) implying that larger positive

and negative SST differences (which compensate each other in BIAS) occur throughout the basin (mainly in the western Mediterranean), as shown in Figure 4.8a. It is worth noting that this degradation occurs outside the Ionian Sea, where the atmospheric forcing is not as strong. This point is crucial for the performance of the SEAS coupled system and draws the attention to the evaluation of the heat fluxes calculated under normal atmospheric conditions, which could affect the predictive capability of the system in the long-term period.

4.3.2 SEAS_COUPLED_ATM

The degradation of the skills of *SEAS_COUPLED_ATM* compared to the uncoupled experiment *UA_as5_UO* when simulating the medicane IANOS is comparatively small. In analyzing this comparison, it is important to note that the reference dataset WIND_GLO_PHY_L4_NRT_012_004 is a blended product between ECMWF and METOP B-C ASCAT scatterometers (Trindade et al., 2020), so this comparison may be slightly

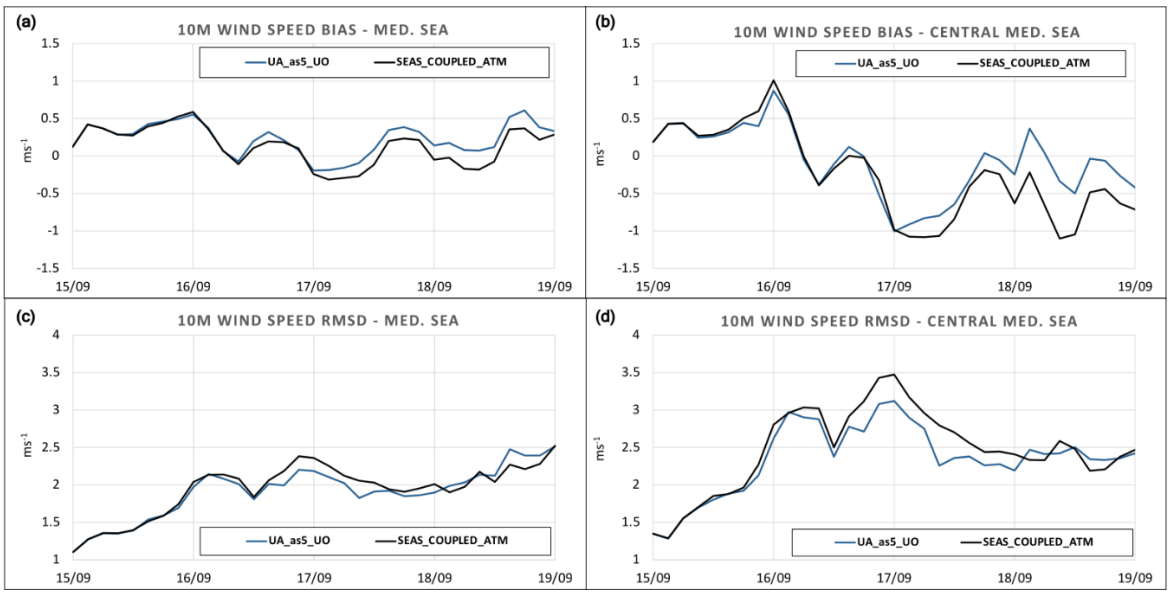

Figure 4.9: 10m wind speed BIAS and RMSD in the Mediterranean Sea basin and in the central Mediterranean Sea respectively in the first and second row

biased because it is somehow a model-to-model comparison.

At the basin scale, the BIAS of wind speed is small and oscillates around zero (Figure 4.9a), *SEAS_COUPLED* has a slightly lower BIAS compared to *UA_as5_UO* and almost identical RMSD. The alternating positive and negative BIAS is determined by the development of Ianos in the central Mediterranean (Figure 4.9b). In that area the BIAS decreases and changes sign from September 16 when Ianos intensifies because both the experiments underestimate the magnitude and extension of the cyclone (not shown). The BIAS of the two experiments in the medicane area diverge significantly starting from 2021-09-18 due both to the different timing and dynamics of the cyclone landfall, which causes in *UA_as5_UO* compensation errors that reduces the BIAS value.

The RMSD increases to the largest values (Figure 4.9d) at the time of the largest negative BIAS and then decreases again. It is interesting to note that the RMSD in the central Mediterranean region starts to decrease when the medicane reaches its mature stage with the maximum intensity. This means that equally both models seem to perform better under these extreme conditions than under normal or moderate intensity meteorological conditions. This is related to the increased predictability that is an intrinsic characteristic of the extreme events (Vitart and Molteni, 2010; Belanger et al., 2012; Lavers et al., 2014; Vitart and Robertson, 2018; Robertson et al., 2020; Domeisen et al., 2022).

4.4 Conclusions

In this chapter the SEAS coupled system was presented and the results were discussed.

The coupling framework is the traditional atmospheric approach, where the ocean is driven by the momentum, mass, and heat fluxes calculated in the atmospheric component and transferred at each coupling time step. Given the horizontal spatial scale of the models (3.8 to 2.6 km), some feedbacks relevant to the atmosphere and ocean may develop on an hourly time scale, so the coupling frequency was set at 30 minutes.

This is a preliminary coupling exercise because, first it is a simulation of an extreme event forced with parent models analyses. Second, due to time constraints, it was not possible to fully implement the coupling strategy proposed by Pullen et al. (2017a). It is recommended that the heat fluxes are computed in the ocean model using the long-term validated bulk formulae, rather than using the atmospheric surface boundary layer parametrizations which are not derived for the ocean surface.

The *SEAS_COUPLED* experiment correctly reproduced the evolution of the medicane Ianos with a short-term simulation from September 15 to September 19, 2020. The limited duration and the intensity of the event required a proper initialization of both model components and the coupler. The oceanic model was initialized with data from a longer uncoupled experiment (*UO_as1*), while the atmospheric model was initialized from ECMWF analyses, and the exchanged fields on 15 Sep 2020 00 UTC were taken at the end of one-hour coupled simulation with a coupling frequency of 5 minutes, when the values were correctly obtained.

The coupled heat fluxes lead to an increase in the SST BIAS compared to the satellite's observations at the scale of the Mediterranean basin, and more so than in the Ionian Sea, where the medicane developed. In this area, the coupling seems to perform better and reduces the positive SST BIAS of the uncoupled experiments. This is because in the coupled experiment a larger amount of latent heat is calculated in the atmospheric model compared to the case of the MFS bulk formulae experiment. At the basin scale, the degradation of the SST BIAS is due to larger positive and negative anomalies that compensate each other but determine a larger value of the RMSD. The

fact that this occurs mainly in the western Mediterranean, where the atmospheric forcing is not as intense, draws the attention to the assessment of atmospheric heat fluxes under normal or moderately intense meteorological conditions and their implications for the long-term ocean forecasting.

The surface ocean currents do not change much between the coupled and uncoupled experiments because the wind pattern and magnitude are nearly the same in both experiments. The coupled experiment also confirms that the cyclone changes the mean surface circulation only in the Ionian Sea and only during the period of its development and transit. Throughout the basin, the climatological features of the Mediterranean circulation are found and reproduced in *SEAS_COUPLED_OCE*.

The mean wind stress turns out to be slightly larger than in the uncoupled experiments, despite the same mean wind speed. This is the result of calculating the momentum transfer coefficient in the atmospheric boundary layer by the Monin-Obukov similarity theory. This aspect needs further investigation with more robust statistics to identify possible long-term trend in the intensity of the surface circulation.

The coupling improves the representation of the medicane Ianos. The surface pressure minimum is only 3 hPa larger than in the ECMWF analyses and its position and timing are improved. It turns out that the magnitude and pattern of the 10m wind field is also very similar to the observational satellite dataset.

Unfortunately, this positive skill is limited only to the Ianos development area, since the positive trend of the RMSD at the basin scale is not reduced by the coupling. In other words, this means that the coupled atmospheric model performs better in representing the extreme event than in less intense meteorological conditions. This positive bias in wind speed can, in turn, affect the magnitude of the surface current, and, furthermore, affect the mass and heat balance by increasing latent heat and evaporation.

This is confirmed by the analysis of the heat fluxes. The only two fluxes that show some differences from the uncoupled experiments are the latent heat and solar radiation. Compared to the *UA_as5_UO* experiment, which uses the same physics setup, the basin averaged values are the same, and the differences are only locally relevant. In the case of latent heat, the reason is the different pattern and magnitude of wind

speed, while in the case of solar radiation, it is not clear whether the different cloud cover or water vapor content in the atmosphere is more effective.

In terms of the heat budget, the *SEAS_COUPLED* experiment is not significantly different from the MFS reference setup in the uncoupled ocean experiments, as *UO_as1* because the net heat flux is 12 Wm^{-2} compared to 16 Wm^{-2}. The *SEAS_COUPLED* experiment shows a larger loss of latent heat, which is compensated by a larger downward solar and thermal radiation. Finally, looking at the *UO_as3* experiment (radiative fluxes from WRF and turbulent fluxes from MFS bulk formulae), the difference in net heat flux is relevant (12 Wm^{-2} vs. 44 Wm^{-2}) because the larger downward radiative fluxes are not counterbalanced by larger turbulent heat fluxes.

Chapter 5

Conclusions and perspectives

This thesis has started the development of a coupled ocean-atmosphere modelling framework for short-term ocean forecasting in the Southern European Seas, including the Mediterranean, Marmara and Black Sea (SEAS). Such a coupled modelling system should realistically account for the complexity of the processes at the air-sea interface and thus improve long-term predictive capabilities. Of course, the predictability of a system is determined by both the initial conditions (Type I predictability) and external forcings (Type II predictability). In this work, we try to improve the air-sea coupling to enhance our capability to exploit the predictability of the coupled ocean and atmospheric system, thus it is a contribution to Type II predictability. Another aspect of Type II predictability lies in the feedbacks between hydrology, ocean, and atmosphere, but is not considered in this work, which focuses on open ocean dynamics.

Understanding the air-sea interaction processes and their feedbacks on the ocean-atmosphere dynamics is a challenge for the forecasting community and more generally for the numerical modelling community. The coupled ocean-atmosphere model implemented in this thesis considers all air-sea interaction fluxes in different pseudo-empirical formulations and attempts to find the most appropriate solutions for short-term forecasting. This goal has been partially achieved, as we will explain later.

The main contribution of this thesis is the development of a coupled numerical modelling system for short-term forecasting that combines two state-of-the-art numerical models, NEMO for the oceanic and WRF for the atmospheric components and implements them with an appropriate resolution in a well-defined domain. The choice of the domain resolution of 1/24° was determined by the Mediterranean

Forecasting System analysis system, which provides accurate initial conditions. Both the atmospheric and oceanic models have the same horizontal resolution, which avoids contamination of surface fluxes from the land during regridding. In addition, the atmospheric model is non-hydrostatic due to its high horizontal resolution, allowing simulation of intense and rapidly evolving phenomena such as medicanes.

The development and evaluation of SEAS has been pursued in two different directions: first, it focused on reproducing an intense Medicane event with and without coupling, and second, it estimated for the first time the predictive capability of the uncoupled ocean component of the system for two seasons to establish the reference matrix for evaluation capability.

Using the Medicane extreme event, we were able to examine the importance of the domain extension, lateral boundary conditions, and initialization. The initial definition of the domain required a southward shift of the boundary from the core of the cyclone. In addition, it has been shown that the model forced with coarse boundary conditions (1/4°) does not develop the cyclone, most likely because it either does not have a proper initial field of potential vorticity or because the resolution gap filters out some important meteorological signals from the area. Another important result is that forecast lead time for this extreme event is about 48 hours for an assimilated and high-resolution initial condition.

The definition of the domain of the coupled system goes beyond the need to reproduce such extreme events. The implementation of the SEAS coupled forecast system must take into account that the atmospheric variability over the Southern European Seas is determined by the large-scale perturbations that develop in the North Atlantic. For this reason, the domain extends over a large part of the Atlantic (to -24°E and north to 58°N).

Following the recommendation of Pullen et al. (2017a), it was decided to use a computational grid for both components to avoid loss of accuracy due to either to data regridding or merging different datasets, which is usually the case when the models do not match domain and resolution.

As mentioned earlier, the quality of the initial conditions (IC) is crucial. For this reason, an ad hoc procedure was implemented to merge the analyses of several models and determine the IC for SEAS. Since the IC for the Mediterranean Sea comes from the

MFS analyses (same resolution, 1/24°) and the Strait of Gibraltar isolates the short-period Atlantic interaction (half resolution, 1/12°), the spin-up time for the slowly evolving ocean model can be reduced to one day.

After this work on the model configuration, the first step toward the coupled ocean-atmosphere simulation of Medicane Ianos was to perform uncoupled experiments to test various physical air-sea parametrizations. The heat fluxes are divided into radiative and turbulent components and are calculated either by the atmospheric model or using different bulk formulae, calibrated for ocean modelling in the 1990s (Pettenuzzo et al., 2010).

First, it has been shown that the SST simulation skills slightly improve for this extreme event when the two downward radiative fluxes (shortwave and longwave downward) calculated with the MFS bulk formulae are replaced with the ECMWF analyses equivalent fluxes. Second, the skills deteriorate slightly when both the above radiative fluxes and the atmospheric forcing from an uncoupled atmospheric experiment are used. This is because in the first case the net heat flux increases only by 8 Wm^{-2} due to the larger downward longwave radiation, while in the second case the net heat flux increases by 28 Wm^{-2} because the turbulent components do not adequately balance the radiative ones.

The WRF setup for the SEAS uncoupled atmospheric experiments showed that the simulated winds and surface pressure are better than the ECMWF forecasts if compared to satellite scatterometer data. The WRF setup uses the MM5 model parametrizations of the surface and planetary boundary layers (Jiménez et al., 2012) and interestingly calculates a net heat flux averaged over the basin of 14 Wm^{-2}, which is closest to the value calculated in the uncoupled ocean experiment (16 Wm^{-2}). This is an important point to consider in the coupling. Transferring heat fluxes to the ocean component that are as close as possible to those of the uncoupled validated model prevents the coupled model from introducing incorrect feedbacks between the components and preserves the energy balance.

The newly implemented ocean component of the SEAS system and its air-sea physics must first be validated in the uncoupled configuration to assess its forecast's skills before becoming part of the operational coupled model SEAS. For this reason, 5-days forecasts were performed for two seasonal periods and two different air-sea flux

configurations: one experiment used the MFS parametrizations (Pettenuzzo et al., 2010), while the second used the ECMWF downward radiative fluxes.

The satellite observed SST and the statistical metrics computed over the Mediterranean Sea (BIAS almost zero and RMSE ≈ 0.6±0.1°C) show equal skills in the two experiments, confirming that ECMWF downward radiative fluxes could be used to replace the MFS formula. Analysis of the basin average heat fluxes shows that the downward longwave radiation of ECMWF is ≈15 Wm^{-2} larger, increasing the net heat flux from negative to almost zero, consistent with the slightly larger SST and the positive BIAS.

The net heat flux is driven by the downward solar radiation flux which has a predominant seasonal cycle, but large fluctuations occur that can last for several (4-10) days, i.e., the synoptic weather over the region The anomalies are determined by intense meteorological events that increase first the latent heat and second the sensible heat fluxes. and can extract more than 700 W/m^2 per day in specific areas. The balance of thermal radiation is negative (-100 W/m^2) at the basin scale and does not show any seasonal trend. With respect to the SEAS coupled system, it appears that the computation of the net longwave radiation balance could be improved by calculating the longwave downward radiation in the atmospheric component.

Finally, the Medicane Ianos was reproduced using the SEAS coupled model. This can be considered as a first test of the coupled system, since it was limited to the simulation of one extreme event and only one coupling strategy was used. This is the traditional way of coupling the ocean and atmosphere, where the ocean is driven by momentum, mass, and heat fluxes, all of which are computed in the atmospheric component, which in turn receives the SST and surface ocean currents.

The results show that the coupled ocean-atmosphere model increases the SST RMSD compared to the uncoupled system at the basin scale, but interestingly not in the Ionian Sea under extreme conditions. At the basin scale, the largest discrepancies occur in the western Mediterranean Sea, where the atmospheric forcing is not as intense, so more attention would be needed in a future assessment of atmospheric heat fluxes under normal or moderately intense meteorological conditions for long-term ocean forecasting.

Compared to the uncoupled ocean experiments forced with ECMWF atmospheric fields, the average wind stress turns out to be slightly larger, although the average wind speed is almost the same. This is the result of the momentum transfer coefficient calculated in the atmospheric boundary layer according to the Monin-Obukov similarity theory. This aspect needs further investigation with more robust statistics to identify a possible long-term trend in the intensification of the surface circulation. In the central Mediterranean region, where Ianos developed, the coupled atmospheric model performs slightly better than the uncoupled model in term on magnitude and pattern of the wind field, positioning, and timing of the cyclone core. Unfortunately, the RMSD of the wind speed at the basin scale is not reduced by the coupling.

The last comment refers to the heat fluxes in the coupled experiment. The coupling does not change the net heat balance, compared to the uncoupled atmospheric experiment, but the components are different, and balance each other in a different way. The shortwave radiation and latent heat components show noticeable changes, but with unchanged values at the basin average. The changes in latent heat can be easily attributed to different wind speed patterns, and the changes in shortwave radiation patterns should be explained by differences in cloud cover. This implies that a more detailed analysis of evaporative fluxes and water vapor content in the atmosphere should be undertaken.

This work leaves open issues that need to be addressed in the future. The most important is the implementation and testing of the "ocean driver" coupling strategy as proposed by Pullen et al. (2017a). The turbulent heat fluxes and wind stress should be computed using the oceanic bulk formulae developed by the MFS service, with some specific parameterizations for marine boundary processes that are not included in many atmospheric BL schemes. Another open question concerns the atmospheric model. The first model layer is 50 m high, which is the value at which the stability functions were considered reliable over land, but this should be investigated further over the ocean. Finally, an extensive period of validation, typically several years, needs to be performed to obtain statistically significant skill scores

Overall, this work has shown that a coupled ocean-atmosphere model is feasible for the short-term forecasting over the Southern European Seas and reproduces the skills of the uncoupled system. The initial conditions for both the ocean and the

atmospheric components are important elements for predictability. Currently, they are taken from separate oceanic and atmospheric data assimilation systems: here we verified that the net heat flux exchanged at the surface is consistent between the coupled and uncoupled system, suggesting that uncoupled data assimilation analyses could be used for some more years to initialize the system.

Acronyms and Abbreviations

BS-PHY NRT	Black Sea Physical Analysis and Forecast System
CERFACS	Centre Européen de Recherche et de Formation Avancée en Calcul Scientifique (Toulouse, France)
CMEMS-GLO	Copernicus Marine Environment Monitoring Service Global Ocean Analysis and Forecasting System
CNRS	Centre National de la Recherche Scientifique (Paris, France)
ECMWF IFS HRES	European Center for Medium range Weather Forecast Integrated Forecast System High RESolution
ERA5	ECMWF Reanalysis version 5
IC	Initial Conditions
L4_SAT	Mediterranean Sea High Resolution and Ultra High Resolution Sea Surface Temperature Analysis: SST_MED_SST_L4_NRT_OBSERVATIONS_010_004
LOBC	Lateral Open Boundary Conditions
MCT	Modelling Coupling Toolkit
MFS/MedFS	Mediterranean Forecasting System
MYJ	Mellor Yamada Janic
MUSCL	Monotone Upstream Scheme for Conservative Laws scheme
NCAR	National Center for Atmospheric Research (Boulder, CO,. U.S.A.)
NCEP	National Center for Environmental Prediction
NEMO	Nucleus for European Modelling of the Ocean
PBL	Planetary Boundary Layer
RRTMG	Rapid Radiative Transfer Model for GCMs
SEAS	Southern European Seas
SBC	Surface Boundary Conditions
SCRIP	Spherical Coordinates Remapping and interpolation Package
SURF	Structured and Unstructured grid Relocatable ocean platform for Forecasting
SST	Sea Surface Temperature

T2m	Air temperature at 2 meters
UTSS	Unstructured Turkish Strait Systems
WISHE	Wind Intensification Surface Heat Exchange
WPS	WRF Preprocessing System
WRF	Weather Research and Forecast

References

Aluie, H., Hecht, M., & Vallis, G. K. (2018). Mapping the Energy Cascade in the North Atlantic Ocean: The Coarse-Graining Approach. *Journal of Physical Oceanography*, *48*(2), 225–244. https://doi.org/10.1175/JPO-D-17-0100.1

Akhtar, N., Brauch, J. & Ahrens, B. Climate modeling over the Mediterranean Sea: impact of resolution and ocean coupling. Clim Dyn 51, 933–948 (2018). https://doi.org/10.1007/s00382-017-3570-8

ARAKAWA, A., & LAMB, V. R. (1977). *Computational Design of the Basic Dynamical Processes of the UCLA General Circulation Model* (pp. 173–265). https://doi.org/10.1016/B978-0-12-460817-7.50009-4

Artale, V., Calmanti, S., Carillo, A., Dell'Aquila, A., Herrmann, M., Pisacane, G., Ruti, P. M., Sannino, G., Struglia, M. V., Giorgi, F., Bi, X., Pal, J. S., & Rauscher, S. (2010). An atmosphere-ocean regional climate model for the Mediterranean area: Assessment of a present climate simulation. *Climate Dynamics*, *35*(5), 721–740. https://doi.org/10.1007/s00382-009-0691-8

Aydoğdu, A., Pinardi, N., Özsoy, E., Danabasoglu, G., Gürses, Ö., & Karspeck, A. (2018). Circulation of the Turkish Straits System under interannual atmospheric forcing. *Ocean Science*, *14*(5), 999–1019. https://doi.org/10.5194/os-14-999-2018

Beck, H. E., E. F. Wood, M. Pan, C. K. Fisher, D. G. Miralles, A. I. J. M. van Dijk, T. R. McVicar, and R. F. Adler (2019). MSWEP V2 Global 3-Hourly 0.1° Precipitation: Methodology and Quantitative Assessment. Bull. Amer. Meteor. Soc., 100, 473–500, https://doi.org/10.1175/BAMS-D-17-0138.1

Belanger, J. I., P. J. Webster, J. A. Curry, and M. T. Jelinek, (2012). Extended Prediction of North Indian Ocean Tropical Cyclones. Wea. Forecasting, 27, 757–769, https://doi.org/10.1175/WAF-D-11-00083.1

Beljaars, A. C. M. (1995). The parametrization of surface fluxes in large-scale models under free convection. *Quarterly Journal of the Royal Meteorological Society*, *121*(522), 255–270. https://doi.org/https://doi.org/10.1002/qj.49712152203

Bignami, F., Marullo, S., Santoleri, R., & Schiano, M. E. (1995). Longwave radiation budget in the Mediterranean Sea. *Journal of Geophysical Research*, *100*(C2), 2501–2514. https://doi.org/10.1029/94JC02496

Billing, H., Haupt, I., & Tonn, W. (1983). *Evolution of a hurricane-like cyclone in the Mediterranean Sea*.

Booij, N., Ris, R. C., & Holthuijsen, L. H. (1999). A third-generation wave model for coastal regions: 1. Model description and validation. *Journal of Geophysical Research: Oceans*, *104*(C4), 7649–7666. https://doi.org/10.1029/98JC02622

Bouin, M. N., & Lebeaupin Brossier, C. (2020a). Surface processes in the 7 November 2014 medicane from air-sea coupled high-resolution numerical modelling. *Atmospheric Chemistry and Physics*, *20*(11), 6861–6881. https://doi.org/10.5194/acp-20-6861-2020

Bouin, M. N., & Lebeaupin Brossier, C. (2020b). Impact of a medicane on the oceanic surface layer from a coupled, kilometre-scale simulation. *Ocean Science*, *16*(5), 1125–1142. https://doi.org/10.5194/os-16-1125-2020

Brown, A., Milton, S., Cullen, M., Golding, B., Mitchell, J., & Shelly, A. (2012). Unified Modeling and Prediction of Weather and Climate: A 25-Year Journey. *Bulletin of the American Meteorological Society*, *93*(12), 1865–1877. https://doi.org/10.1175/BAMS-D-12-00018.1

Bryan, K., Manabe, S., & Pacanowski, R. C. (1975). A Global Ocean-Atmosphere Climate Model. Part II. The Oceanic Circulation. *Journal of Physical Oceanography*, *5*(1), 30–46. https://doi.org/10.1175/1520-0485(1975)005<0030:AGOACM>2.0.CO;2

Buongiorno Nardelli, B., Tronconi, C., Pisano, A., & Santoleri, R. (2013a). *Mediterranean Sea High Resolution and Ultra High Resolution Sea Surface Temperature Analysis*.

Buongiorno Nardelli, B., Tronconi, C., Pisano, A., & Santoleri, R. (2013b). High and Ultra-High resolution processing of satellite Sea Surface Temperature data over Southern European Seas in the framework of MyOcean project. *Remote Sensing of Environment*, *129*, 1–16. https://doi.org/10.1016/j.rse.2012.10.012

Businger, S., & Reed, R. J. (1989). Cyclogenesis in Cold Air Masses. *Weather and Forecasting*, *4*(2), 133–156. https://doi.org/10.1175/1520-0434(1989)004<0133:CICAM>2.0.CO;2

Carniel, S., Benetazzo, A., Bonaldo, D., Falcieri, F. M., Miglietta, M. M., Ricchi, A., & Sclavo, M. (2016). Scratching beneath the surface while coupling atmosphere, ocean and waves: Analysis of a dense water formation event. *Ocean Modelling*, *101*, 101–112. https://doi.org/10.1016/j.ocemod.2016.03.007

Castellari, S., Pinardi, N., & Leaman, K. (1998). A model study of air-sea interactions in the Mediterranean Sea. In *Journal of Marine Systems* (Vol. 18) https://doi.org/10.1016/S0924-7963(98)90007-0.

Cavicchia, L., & von Storch, H. (2012). The simulation of medicanes in a high-resolution regional climate model. *Climate Dynamics*, *39*(9–10), 2273–2290. https://doi.org/10.1007/s00382-011-1220-0

Cavicchia, L., von Storch, H., & Gualdi, S. (2014). A long-term climatology of medicanes. *Climate Dynamics*, *43*(5–6), 1183–1195. https://doi.org/10.1007/s00382-013-1893-7

Chen, F., & Dudhia, J. (2001). Coupling an Advanced Land Surface–Hydrology Model with the Penn State–NCAR MM5 Modeling System. Part I: Model Implementation and Sensitivity. *Monthly Weather Review*, *129*(4), 569–585. https://doi.org/10.1175/1520-0493(2001)129<0569:CAALSH>2.0.CO;2

Ciliberti, S., Jansen, E., Martins, D., Gunduz, M., Ilicak, M., & Stefanizzi, L. (2021). *Black Sea Physical Analysis and Forecast*. https://doi.org/https://doi.org/10.25423/cmcc/blksea_analysisforecast_phy_007_001_eas4

Clementi, E., Aydogdu, A., Goglio, A., Pistoia, J., Escudier, R., Drudi, M., Grandi, A., Mariani, A., Lyubartsev, V., Lecci, R., Creti', S., Coppini, G., Masina, S., & Pinardi,

N. (2021). Mediterranean Sea Physics Analysis and Forecast. In *Copernicus Monitoring Environment Marine Service (CMEMS).*

Clementi, E., Oddo, P., Drudi, M., Pinardi, N., Korres, G., & Grandi, A. (2017). Coupling hydrodynamic and wave models: first step and sensitivity experiments in the Mediterranean Sea. *Ocean Dynamics*, *67*(10), 1293–1312. https://doi.org/10.1007/s10236-017-1087-7

Craig, A., Valcke, S., & Coquart, L. (2017). Development and performance of a new version of the OASIS coupler, OASIS3-MCT-3.0. *Geoscientific Model Development*, *10*(9), 3297–3308. https://doi.org/10.5194/GMD-10-3297-2017

Delworth, T. L., & Zeng, F. (2016). The Impact of the North Atlantic Oscillation on Climate through Its Influence on the Atlantic Meridional Overturning Circulation. *Journal of Climate*, *29*(3), 941–962. https://doi.org/10.1175/JCLI-D-15-0396.1

Demirov, E. K., & Pinardi, N. (2007). On the relationship between the water mass pathways and eddy variability in the Western Mediterranean Sea. *Journal of Geophysical Research*, *112*(C2), C02024. https://doi.org/10.1029/2005JC003174

Domeisen, D. I. V., and Coauthors, 2022: Advances in the Subseasonal Prediction of Extreme Events: Relevant Case Studies across the Globe. Bull. Amer. Meteor. Soc., 103, E1473–E1501 https://doi.org/10.1175/BAMS-D-20-0221.1

Donelan, M. A., Haus, B. K., Reul, N., Plant, W. J., Stiassnie, M., Graber, H. C., Brown, O. B., & Saltzman, E. S. (2004). On the limiting aerodynamic roughness of the ocean in very strong winds. *Geophysical Research Letters*, *31*(18). https://doi.org/10.1029/2004GL019460

Drobinski, P., Anav, A., Lebeaupin Brossier, C., Samson, G., Stéfanon, M., Bastin, S., Baklouti, M., Béranger, K., Beuvier, J., Bourdallé-Badie, R., Coquart, L., D'Andrea, F., de Noblet-Ducoudré, N., Diaz, F., Dutay, J. C., Ethe, C., Foujols, M. A., Khvorostyanov, D., Madec, G., … Viovy, N. (2012). Model of the Regional Coupled Earth system (MORCE): Application to process and climate studies

in vulnerable regions. *Environmental Modelling and Software*, *35*, 1–18. https://doi.org/10.1016/j.envsoft.2012.01.017

Dubois, C., Somot, S., Calmanti, S., Carillo, A., Déqué, M., Dell'Aquilla, A., Elizalde, A., Gualdi, S., Jacob, D., L'Hévéder, B., Li, L., Oddo, P., Sannino, G., Scoccimarro, E., & Sevault, F. (2012). Future projections of the surface heat and water budgets of the Mediterranean Sea in an ensemble of coupled atmosphere-ocean regional climate models. *Climate Dynamics*, *39*(7–8), 1859–1884. https://doi.org/10.1007/s00382-011-1261-4

Emanuel, K. A. (1986). An Air-Sea Interaction Theory for Tropical Cyclones. Part I: Steady-State Maintenance. *Journal of the Atmospheric Sciences*, *43*(6), 585–605. https://doi.org/10.1175/1520-0469(1986)043<0585:AASITF>2.0.CO;2

Ernst, J. A., & Matson, M. (1983). A MEDITERRANEAN TROPICAL STORM? *Weather*, *38*(11), 332–337. https://doi.org/10.1002/j.1477-8696.1983.tb04818.x

Fairall, C. W., E. F. Bradley, J. E. Hare, A. A. Grachev, and J. B. Edson, 2003: Bulk Parameterization of Air–Sea Fluxes: Updates and Verification for the COARE Algorithm. J. Climate, 16, 571–591, https://doi.org/10.1175/1520-0442(2003)016<0571:BPOASF>2.0.CO;2.

Fairall, C. W., Bradley, E. F., Rogers, D. P., Edson, J. B., & Young, G. S. (1996). Bulk parameterization of air-sea fluxes for tropical oceanglobal atmosphere coupled-ocean atmosphere response experiment. *Journal of Geophysical Research: Oceans*, *101*(C2), 3747–3764. https://doi.org/10.1029/95JC03205

Federico, I., Pinardi, N., Coppini, G., Oddo, P., Lecci, R., & Mossa, M. (2017). Coastal ocean forecasting with an unstructured grid model in the southern Adriatic and northern Ionian seas. *Natural Hazards and Earth System Sciences*, *17*(1), 45–59. https://doi.org/10.5194/nhess-17-45-2017

Garratt, J. (1992). The atmospheric boundary layer. Cambridge University Press ISBN 0 521 38052 9. Q.J.R. Meteorol. Soc., 120: 1428-1429. https://doi.org/10.1002/qj.49712051919

González-Alemán, J. J., Pascale, S., Gutierrez-Fernandez, J., Murakami, H., Gaertner, M. A., & Vecchi, G. A. (2019). Potential Increase in Hazard From Mediterranean Hurricane Activity With Global Warming. *Geophysical Research Letters*, *46*(3), 1754–1764. https://doi.org/10.1029/2018GL081253

Good, S., Fiedler, E., Mao, C., Martin, M. J., Maycock, A., Reid, R., Roberts-Jones, J., Searle, T., Waters, J., While, J., & Worsfold, M. (2020). The Current Configuration of the OSTIA System for Operational Production of Foundation Sea Surface Temperature and Ice Concentration Analyses. *Remote Sensing*, *12*(4), 720. https://doi.org/10.3390/rs12040720

Gualdi, S., Somot, S., Li, L., Artale, V., Adani, M., Bellucci, A., Braun, A., Calmanti, S., Carillo, A., Dell'Aquila, A., Déqué, M., Dubois, C., Elizalde, A., Harzallah, A., Jacob, D., L'Hévéder, B., May, W., Oddo, P., Ruti, P., … Navarra, A. (2013). THE circe simulations: Regional climate change projections with realistic representation of the mediterranean sea. *Bulletin of the American Meteorological Society*, *94*(1), 65–81. https://doi.org/10.1175/BAMS-D-11-00136.1

Gualdi Silvio Andrea Borrelli, Antonio Cantelli, Guido Davoli, Simona Masina, Antonio Navarra, Antonella Sanna, & Stefano Tibaldi. (2020). *The new CMCC Operational Seasonal Prediction System*. https://doi.org/10.25424/CMCC/SPS3.5

Hasselmann, K. (1976). Stochastic climate models Part I. Theory. *Tellus*, *28*(6), 473–485. https://doi.org/10.1111/j.2153-3490.1976.tb00696.x

Hellerman, S., & Rosenstein, M. (1983). Normal Monthly Wind Stress Over the World Ocean with Error Estimates. *Journal of Physical Oceanography*, *13*(7), 1093–1104. https://doi.org/10.1175/1520-0485(1983)013<1093:NMWSOT>2.0.CO;2

Hodur, R. M. (1997). The Naval Research Laboratory's Coupled Ocean/Atmosphere Mesoscale Prediction System (COAMPS). *Monthly Weather Review*, *125*(7), 1414–1430. https://doi.org/10.1175/1520-0493(1997)125<1414:TNRLSC>2.0.CO;2

Hogan, R. & Bozzo, A. (2016). ECRAD: A new radiation scheme for the IFS. ECMWF Technical Memoranda, 787. 10.21957/whntqkfdz

Hong, S.-Y., Noh, Y., & Dudhia, J. (2006). A New Vertical Diffusion Package with an Explicit Treatment of Entrainment Processes. *Monthly Weather Review*, *134*(9), 2318–2341. https://doi.org/10.1175/MWR3199.1

Iacono, M. J., Delamere, J. S., Mlawer, E. J., Shephard, M. W., Clough, S. A., & Collins, W. D. (2008). Radiative forcing by long-lived greenhouse gases: Calculations with the AER radiative transfer models. *Journal of Geophysical Research*, *113*(D13), D13103. https://doi.org/10.1029/2008JD009944

Ilicak, M., Federico, I., Barletta, I., Mutlu, S., Karan, H., Ciliberti, S. A., Clementi, E., Coppini, G., & Pinardi, N. (2021). Modeling of the turkish strait system using a high resolution unstructured grid ocean circulation model. *Journal of Marine Science and Engineering*, *9*(7). https://doi.org/10.3390/jmse9070769

Janjic, Z. (2001). *Nonsingular implementation of the Mellor-Yamada level 2.5 scheme in the NCEP Meso model*.

Jiménez, P. A., Dudhia, J., González-Rouco, J. F., Navarro, J., Montávez, J. P., & García-Bustamante, E. (2012). A revised scheme for the WRF surface layer formulation. *Monthly Weather Review*, *140*(3), 898–918. https://doi.org/10.1175/MWR-D-11-00056.1

Jullien, S., Masson, S., Oerder, V., Samson, G., Colas, F., & Renault, L. (2020). Impact of Ocean–Atmosphere Current Feedback on Ocean Mesoscale Activity: Regional Variations and Sensitivity to Model Resolution. *Journal of Climate*, *33*(7), 2585–2602. https://doi.org/10.1175/JCLI-D-19-0484.1

Kondo, J. (1975). *AIR-SEA BULK TRANSFER COEFFICIENTS IN DIABATIC CONDITIONS*.

Lagouvardos, K., Karagiannidis, A., Dafis, S., Kalimeris, A., & Kotroni, V. (2022). Ianos-A Hurricane in the Mediterranean. *Bulletin of the American Meteorological Society*, *103*(6), E1621–E1636. https://doi.org/10.1175/BAMS-D-20-0274.1

Lagouvardos, K., Kotroni, V., Nickovic, S., Jovic, D., Kallos, G., & Tremback, C. J. (1999). Observations and model simulations of a winter sub-synoptic vortex over the central Mediterranean. *Meteorological Applications*, *6*(4), 371–383. https://doi.org/10.1017/S1350482799001309

Large, W. B. (2006). *SURFACE FLUXES FOR PRACTITIONERS OF GLOBAL OCEAN DATA ASSIMILATION*.

Lavers, D., Pappenberger, F. & Zsoter, E., (2014). Extending medium-range predictability of extreme hydrological events in Europe. Nat Commun 5, 5382. https://doi.org/10.1038/ncomms6382

Lebeaupin Brossier, C. L., & Drobinski, P. (2009). Numerical high-resolution air-sea coupling over the Gulf of Lions during two tramontane/mistral events. *Journal of Geophysical Research Atmospheres*, *114*(10). https://doi.org/10.1029/2008JD011601

Lebeaupin Brossier, C., Léger, F., Giordani, H., Beuvier, J., Bouin, M. N., Ducrocq, V., & Fourrié, N. (2017). Dense water formation in the north-western Mediterranean area during HyMeX-SOP2 in 1/36° ocean simulations: Ocean-atmosphere coupling impact. *Journal of Geophysical Research: Oceans*, *122*(7), 5749–5773. https://doi.org/10.1002/2016JC012526

Lengaigne, M., Neetu, S., Samson, G., Vialard, J., Krishnamohan, K. S., Masson, S., Jullien, S., Suresh, I., & Menkes, C. E. (2019). Influence of air–sea coupling on Indian Ocean tropical cyclones. *Climate Dynamics*, *52*(1–2), 577–598. https://doi.org/10.1007/S00382-018-4152-0/FIGURES/16

Lewis, H., Manuel Castillo Sanchez, J., Arnold, A., Fallmann, J., Saulter, A., Graham, J., Bush, M., Siddorn, J., Palmer, T., Lock, A., Edwards, J., Bricheno, L., Martínez-De La Torre, A., & Clark, J. (2019). The UKC3 regional coupled environmental prediction system. *Geoscientific Model Development*, *12*(6), 2357–2400. https://doi.org/10.5194/gmd-12-2357-2019

Li, D., Bou-Zeid, E., Barlage, M., Chen, F., & Smith, J. A. (2013). Development and evaluation of a mosaic approach in the WRF-Noah framework. *Journal of Geophysical Research: Atmospheres*, *118*(21), 11,918-11,935. https://doi.org/10.1002/2013JD020657

Licer, M., Smerkol, P., Fettich, A., Ravdas, M., Papapostolou, A., Mantziafou, A., Strajnar, B., Cedilnik, J., Jeromel, M., Jerman, J., Petan, S., Malačič, V., & Sofianos, S. (2016). Modeling the ocean and atmosphere during an extreme bora event in northern Adriatic using one-way and two-way atmosphere-ocean coupling. *Ocean Science*, *12*(1), 71–86. https://doi.org/10.5194/os-12-71-2016

Loglisci, N., Qian, M. W., Rachev, N., Cassardo, C., Longhetto, A., Purini, R., Trivero, P., Ferrarese, S., & Giraud, C. (2004). Development of an atmospheric-ocean coupled model and its application over the Adriatic Sea during a severe weather event of Bora wind. *Journal of Geophysical Research D: Atmospheres*, *109*(1). https://doi.org/10.1029/2003jd003956

Lorenz, E. N. (1975) Climatic predictability. *The Physical Basis of Climate and Climate Modelling,* B. Bolin et al., Eds., GARP Publication Series, Vol. 16, World Meteorological Organization, 132–136

Madec, G. (2017). *Nemo Ocean Engime*.

Manabe, S., Bryan, K., & Spelman, M. J. (1975). A Global Ocean-Atmosphere Climate Model. Part I. The Atmospheric Circulation. *Journal of Physical Oceanography*, *5*(1), 3–29. https://doi.org/10.1175/1520-0485(1975)005<0003:AGOACM>2.0.CO;2

Mantua, N. J., Hare, S. R., Zhang, Y., Wallace, J. M., & Francis, R. C. (1997). A Pacific Interdecadal Climate Oscillation with Impacts on Salmon Production. *Bulletin of the American Meteorological Society*, *78*(6), 1069–1079. https://doi.org/10.1175/1520-0477(1997)078<1069:APICOW>2.0.CO;2

Mellor, G. L., & Yamada, T. (1982). Development of a turbulence closure model for geophysical fluid problems. *Reviews of Geophysics*, *20*(4), 851. https://doi.org/10.1029/RG020i004p00851

Miglietta, M. M., Mastrangelo, D. & Conte, D. (2015). Influence of physics parameterization schemes on the simulation of a tropical-like cyclone in the Mediterranean Sea. *Atmospheric Research*, 153, 360-375. https://doi.org/10.1016/j.atmosres.2014.09.008

Miglietta, M. M., & Rotunno, R. (2019). Development mechanisms for Mediterranean tropical-like cyclones (medicanes). *Quarterly Journal of the*

Royal Meteorological Society, *145*(721), 1444–1460. https://doi.org/10.1002/qj.3503

Miller, A. J., Collins, M., Gualdi, S., Jensen, T. G., Misra, V., Pezzi, L. P., Pierce, D. W., Putrasahan, D., Seo, H., & Tseng, Y.-H. (2017). Coupled ocean-atmosphere modeling and predictions. In *THE SEA: THE SCIENCE OF OCEAN PREDICTION Journal of Marine Research* (Vol. 75).

Mylonas MP, Douvis KC, Polychroni ID, Politi N, Nastos PT. Analysis of a Mediterranean Tropical-Like Cyclone. Sensitivity to WRF Parameterizations and Horizontal Resolution. *Atmosphere*. 2019; 10(8):425. https://doi.org/10.3390/atmos10080425

Newman, M., Alexander, M. A., Ault, T. R., Cobb, K. M., Deser, C., di Lorenzo, E., Mantua, N. J., Miller, A. J., Minobe, S., Nakamura, H., Schneider, N., Vimont, D. J., Phillips, A. S., Scott, J. D., & Smith, C. A. (2016). The Pacific decadal oscillation, revisited. *Journal of Climate*, *29*(12), 4399–4427. https://doi.org/10.1175/JCLI-D-15-0508.1

Oddo, P., Adani, M., Pinardi, N., Fratianni, C., Tonani, M., and Pettenuzzo, D.: A nested Atlantic-Mediterranean Sea general circulation model for operational forecasting, Ocean Sci., 5, 461–473, https://doi.org/10.5194/os-5-461-2009, 2009

Olabarrieta, M., Warner, J. C., Armstrong, B., Zambon, J. B., & He, R. (2012). Ocean–atmosphere dynamics during Hurricane Ida and Nor'Ida: An application of the coupled ocean–atmosphere–wave–sediment transport (COAWST) modeling system. *Ocean Modelling*, *43–44*, 112–137. https://doi.org/10.1016/j.ocemod.2011.12.008

Payne, R. E. (1972). Albedo of the Sea Surface. *Journal of the Atmospheric Sciences*, *29*(5), 959–970. https://doi.org/10.1175/1520-0469(1972)029<0959:AOTSS>2.0.CO;2

Pettenuzzo, D., Large, W. G., & Pinardi, N. (2010). On the corrections of ERA-40 surface flux products consistent with the Mediterranean heat and water budgets and the connection between basin surface total heat flux and NAO.

Journal of Geophysical Research: Oceans, *115*(6). https://doi.org/10.1029/2009JC005631

Petterssen, S. (1956). *Weather Analysis and Forecasting* (2nd ed.). McGraw-Hill.

Pinardi, N., Zavatarelli, M., Adani, M., Coppini, G., Fratianni, C., Oddo, P., Simoncelli, S., Tonani, M., Lyubartsev, V., Dobricic, S., & Bonaduce, A. (2015). Mediterranean Sea large-scale low-frequency ocean variability and water mass formation rates from 1987 to 2007: A retrospective analysis. *Progress in Oceanography*, *132*, 318–332. https://doi.org/10.1016/j.pocean.2013.11.003

Pullen, J., Allard, R., Seo, H., Miller, A. J., Chen, S., Pezzi, L. P., Smith, T., Chu, P., Alves, J., & Caldeira, R. (2017a). Coupled ocean-atmosphere forecasting at short and medium time scales. In *THE SEA: THE SCIENCE OF OCEAN PREDICTION Journal of Marine Research* (Vol. 75).

Pullen, J., Caldeira, R., Doyle, J. D., May, P., & Tomé, R. (2017b). Modeling the air-sea feedback system of Madeira Island. *Journal of Advances in Modeling Earth Systems*, *9*(3), 1641–1664. https://doi.org/10.1002/2016MS000861

Pullen, J., Doyle, J. D., Haack, T., Dorman, C., Signell, R. P., & Lee, C. M. (2007). Bora event variability and the role of air-sea feedback. *Journal of Geophysical Research: Oceans*, *112*(3). https://doi.org/10.1029/2006JC003726

Pullen, J., Doyle, J. D., Hodur, R., Ogston, A., Book, J. W., Perkins, H., & Signell, R. (2003). Coupled ocean-atmosphere nested modeling of the Adriatic Sea during winter and spring 2001. *Journal of Geophysical Research: Oceans*, *108*(10). https://doi.org/10.1029/2003jc001780

Pullen, J., Doyle, J. D., & Signell, R. P. (2006). Two-Way Air–Sea Coupling: A Study of the Adriatic. *Monthly Weather Review*, *134*(5), 1465–1483. https://doi.org/10.1175/MWR3137.1

Pytharoulis I, Kartsios S, Tegoulias I, Feidas H, Miglietta MM, Matsangouras I, Karacostas T. Sensitivity of a Mediterranean Tropical-Like Cyclone to Physical Parameterizations. *Atmosphere*. 2018; 9(11):436. https://doi.org/10.3390/atmos9110436

Rainaud, R., Brossier, C. L., Ducrocq, V., & Giordani, H. (2017). High-resolution air–sea coupling impact on two heavy precipitation events in the Western Mediterranean. *Quarterly Journal of the Royal Meteorological Society*, *143*(707), 2448–2462. https://doi.org/10.1002/qj.3098

Rainaud, R., Lebeaupin Brossier, C., Ducrocq, V., Giordani, H., Nuret, M., Fourrié, N., Bouin, M. N., Taupier-Letage, I., & Legain, D. (2016). Characterization of air–sea exchanges over the Western Mediterranean Sea during HyMeX SOP1 using the AROME–WMED model. *Quarterly Journal of the Royal Meteorological Society*, *142*, 173–187. https://doi.org/10.1002/qj.2480

Reed 1977 On Estimating Insolation over the Ocean.

Renault, L., Masson, S., Oerder, V., Jullien, S., & Colas, F. (2019). Disentangling the Mesoscale Ocean-Atmosphere Interactions. *Journal of Geophysical Research: Oceans*, *124*(3), 2164–2178. https://doi.org/10.1029/2018JC014628

Ricchi, A., Bonaldo, D., Cioni, G., Carniel, S., & Miglietta, M. M. (2021). Simulation of a flash-flood event over the Adriatic Sea with a high-resolution atmosphere–ocean–wave coupled system. *Scientific Reports*, *11*(1). https://doi.org/10.1038/s41598-021-88476-1

Ricchi, A., Miglietta, M. M., Barbariol, F., Benetazzo, A., Bergamasco, A., Bonaldo, D., Cassardo, C., Falcieri, F. M., Modugno, G., Russo, A., Sclavo, M., & Carniel, S. (2017). Sensitivity of a Mediterranean tropical-like Cyclone to different model configurations and coupling strategies. *Atmosphere*, *8*(5). https://doi.org/10.3390/atmos8050092

Ricchi, A., Miglietta, M. M., Bonaldo, D., Cioni, G., Rizza, U., & Carniel, S. (2019). Multi-Physics ensemble versus atmosphere-ocean coupled model simulations for a tropical-like cyclone in the Mediterranean Sea. *Atmosphere*, *10*(4). https://doi.org/10.3390/ATMOS10040202

Robertson, A. W., Vitart, F., & Camargo, S. J. (2020). Subseasonal to seasonal prediction of weather to climate with application to tropical cyclones. Journal of Geophysical Research: Atmospheres, 125, e2018JD029375. https://doi.org/10.1029/2018JD029375

Romera, R., Gaertner, M. Á., Sánchez, E., Domínguez, M., González-Alemán, J. J., & Miglietta, M. M. (2017). Climate change projections of medicanes with a large multi-model ensemble of regional climate models. *Global and Planetary Change*, *151*, 134–143. https://doi.org/10.1016/j.gloplacha.2016.10.008

Rosati and Miyakoda 1988 A General Circulation Model for Upper Ocean Simulation.

Rotunno, R., & Emanuel, K. A. (1987). An Air–Sea Interaction Theory for Tropical Cyclones. Part II: Evolutionary Study Using a Nonhydrostatic Axisymmetric Numerical Model. *Journal of the Atmospheric Sciences*, *44*(3), 542–561. https://doi.org/10.1175/1520-0469(1987)044<0542:AAITFT>2.0.CO;2

Samson, G., Masson, S., Durand, F., Terray, P., Berthet, S., & Jullien, S. (2017). Roles of land surface albedo and horizontal resolution on the Indian summer monsoon biases in a coupled ocean–atmosphere tropical-channel model. *Climate Dynamics*, *48*(5–6), 1571–1594. https://doi.org/10.1007/s00382-016-3161-0

Samson, G., Masson, S., Lengaigne, M., Keerthi, M. G., Vialard, J., Pous, S., Madec, G., Jourdain, N. C., Jullien, S., Menkes, C., & Marchesiello, P. (2015). The NOW regional coupled model: Application to the tropical Indian Ocean climate and tropical cyclone activity. *Journal of Advances in Modeling Earth Systems*, *6*(3), 700–722. https://doi.org/10.1002/2014MS000324

Sanchez-Gomez, E., Somot, S., Josey, S. A., Dubois, C., Elguindi, N., & Déqué, M. (2011). Evaluation of Mediterranean Sea water and heat budgets simulated by an ensemble of high resolution regional climate models. *Climate Dynamics*, *37*(9–10), 2067–2086. https://doi.org/10.1007/S00382-011-1012-6/FIGURES/6

Sanna, A., Lionello, P., & Gualdi, S. (2013). Coupled atmosphere ocean climate model simulations in the Mediterranean region: Effect of a high-resolution marine model on cyclones and precipitation. *Natural Hazards and Earth System Sciences*, *13*(6), 1567–1577. https://doi.org/10.5194/nhess-13-1567-2013

Sauvage, C., Lebeaupin Brossier, C., & Bouin, M. N. (2021). Towards kilometer-scale ocean-atmosphere-wave coupled forecast: A case study on a Mediterranean heavy precipitation event. *Atmospheric Chemistry and Physics*, *21*(15), 11857–11887. https://doi.org/10.5194/acp-21-11857-2021

Seity, Y., Brousseau, P., Malardel, S., Hello, G., Bénard, P., Bouttier, F., Lac, C., & Masson, V. (2011). The AROME-France Convective-Scale Operational Model. *Monthly Weather Review*, *139*(3), 976–991. https://doi.org/10.1175/2010MWR3425.1

Seo, H., Miller, A. J., & Norris, J. R. (2016). Eddy-wind interaction in the California Current System: Dynamics and impacts. *Journal of Physical Oceanography*, *46*(2), 439–459. https://doi.org/10.1175/JPO-D-15-0086.1

Seo, H., Miller, A. J., & Roads, J. O. (2007). The Scripps Coupled Ocean–Atmosphere Regional (SCOAR) Model, with Applications in the Eastern Pacific Sector. *Journal of Climate*, *20*(3), 381–402. https://doi.org/10.1175/JCLI4016.1

Seo, H., & Xie, S. P. (2011). Response and impact of equatorial ocean dynamics and tropical instability waves in the tropical Atlantic under global warming: A regional coupled downscaling study. *Journal of Geophysical Research: Oceans*, *116*(3). https://doi.org/10.1029/2010JC006670

Sevault, F., Somot, S., Alias, A., Dubois, C., Lebeaupin-Brossier, C., Nabat, P., Adloff, F., Déqué, M., & Decharme, B. (2014). A fully coupled Mediterranean regional climate system model: design and evaluation of the ocean component for the 1980–2012 period. *Tellus A: Dynamic Meteorology and Oceanography*, *66*(1), 23967. https://doi.org/10.3402/tellusa.v66.23967

Seyfried, L., Marsaleix, P., Richard, E., & Estournel, C. (2017). Modelling deep-water formation in the north-west Mediterranean Sea with a new air-sea coupled model: Sensitivity to turbulent flux parameterizations. *Ocean Science*, *13*(6), 1093–1112. https://doi.org/10.5194/os-13-1093-2017

Shapiro, R. (1970). Smoothing, filtering, and boundary effects. *Reviews of Geophysics*, *8*(2), 359. https://doi.org/10.1029/RG008i002p00359

Shchepetkin, A. F., & McWilliams, J. C. (2005). The regional oceanic modeling system (ROMS): a split-explicit, free-surface, topography-following-

coordinate oceanic model. *Ocean Modelling*, *9*(4), 347–404. https://doi.org/10.1016/j.ocemod.2004.08.002

Skamarock, W. C., J. B. Klemp, J. Dudhia, D. O. Gill, Z. Liu, J. Berner, W. Wang, J. G. Powers, M. G. Duda, D. M. Barker, and X.-Y. Huang, 2019: A Description of the Advanced Research WRF Version 4. *NCAR Tech. Note NCAR/TN-556+STR*, 145 pp. doi:10.5065/1dfh-6p97

Somot, S., Sevault, F., Déqué, M., & Crépon, M. (2008). 21st century climate change scenario for the Mediterranean using a coupled atmosphere-ocean regional climate model. *Global and Planetary Change*, *63*(2–3), 112–126. https://doi.org/10.1016/j.gloplacha.2007.10.003

Strajnar, B., Cedilnik, J., Fettich, A., Ličer, M., Pristov, N., Smerkol, P., & Jerman, J. (2019). Impact of two-way coupling and sea-surface temperature on precipitation forecasts in regional atmosphere and ocean models. *Quarterly Journal of the Royal Meteorological Society*, *145*(718), 228–242. https://doi.org/10.1002/qj.3425

Thompson, G., & Eidhammer, T. (2014). A Study of Aerosol Impacts on Clouds and Precipitation Development in a Large Winter Cyclone. *Journal of the Atmospheric Sciences*, *71*(10), 3636–3658. https://doi.org/10.1175/JAS-D-13-0305.1

Thompson, G., Field, P. R., Rasmussen, R. M., & Hall, W. D. (2008). Explicit Forecasts of Winter Precipitation Using an Improved Bulk Microphysics Scheme. Part II: Implementation of a New Snow Parameterization. *Monthly Weather Review*, *136*(12), 5095–5115. https://doi.org/10.1175/2008MWR2387.1

Tiedtke, M. (1989). A Comprehensive Mass Flux Scheme for Cumulus Parameterization in Large-Scale Models. *Monthly Weather Review*, *117*(8), 1779–1800. https://doi.org/10.1175/1520-0493(1989)117<1779:ACMFSF>2.0.CO;2

Tolman, H. L., Balasubramaniyan, B., Burroughs, L. D., Chalikov, D. v., Chao, Y. Y., Chen, H. S., & Gerald, V. M. (2002). Development and Implementation of Wind-Generated Ocean Surface Wave Modelsat NCEP*. *Weather and Forecasting*,

17(2), 311–333. https://doi.org/10.1175/1520-0434(2002)017<0311:DAIOWG>2.0.CO;2

Trenberth, K. E., J. T. Fasullo, and J. Kiehl (2009). Earth's Global Energy Budget. Bull. Amer. Meteor. Soc., 90, 311–324, https://doi.org/10.1175/2008BAMS2634.1.

Trindade, A., Portabella, M., Stoffelen, A., Lin, W., & Verhoef, A. (2020). ERAstar: A High-Resolution Ocean Forcing Product. *IEEE Transactions on Geoscience and Remote Sensing*, *58*(2), 1337–1347. https://doi.org/10.1109/TGRS.2019.2946019

Trotta, F., Fenu, E., Pinardi, N., Bruciaferri, D., Giacomelli, L., Federico, I., & Coppini, G. (2016). A Structured and Unstructured grid Relocatable ocean platform for Forecasting (SURF). *Deep-Sea Research Part II: Topical Studies in Oceanography*, *133*, 54–75. https://doi.org/10.1016/j.dsr2.2016.05.004

Valcke, S. (2013). The OASIS3 coupler: a European climate modelling community software. *Geoscientific Model Development*, *6*(2), 373–388. https://doi.org/10.5194/GMD-6-373-2013

Vallis, G. K. (2006). *Atmospheric and Oceanic Fluid Dynamics*. Cambridge University Press. https://doi.org/10.1017/CBO9780511790447

Vázquez Proveyer, L., Sierra Lorenzo, M., Cruz Rodríguez, R. C., & Warner, J. C. (2022). Analysis of ocean dynamics during the impact of Hurricane Matthew using ocean-atmosphere coupling. *Cuban Journal of Meteorology (Revista Cubana de Meteorología)*, *28*(1). https://doi.org/2377/v28n1e05

Vitart, F. and Molteni, F. (2010), Simulation of the Madden– Julian Oscillation and its teleconnections in the ECMWF forecast system. Q.J.R. Meteorol. Soc., 136: 842-855. https://doi.org/10.1002/qj.623

Vitart, F., Robertson, A.W. The sub-seasonal to seasonal prediction project (S2S) and the prediction of extreme events. npj Clim Atmos Sci 1, 3 (2018). https://doi.org/10.1038/s41612-018-0013-0

von Storch, H., & Zorita, E. (2019). The history of ideas of downscaling-from synoptic dynamics and spatial interpolation. In *Frontiers in Environmental*

Science (Vol. 7, Issue FEB). Frontiers Media S.A. https://doi.org/10.3389/fenvs.2019.00021

Warner, J. C., Armstrong, B., He, R., & Zambon, J. B. (2010). Development of a Coupled Ocean–Atmosphere–Wave–Sediment Transport (COAWST) Modeling System. *Ocean Modelling*, *35*(3), 230–244. https://doi.org/10.1016/j.ocemod.2010.07.010

Wicker, L. J., & Skamarock, W. C. (2002). Time-Splitting Methods for Elastic Models Using Forward Time Schemes. *Monthly Weather Review*, *130*(8), 2088–2097. https://doi.org/10.1175/1520-0493(2002)130<2088:TSMFEM>2.0.CO;2

Zambon, J. B., He, R., & Warner, J. C. (2014). Investigation of hurricane Ivan using the coupled ocean–atmosphere–wave–sediment transport (COAWST) model. *Ocean Dynamics*, *64*(11), 1535–1554. https://doi.org/10.1007/s10236-014-0777-7

Zambon, J. B., He, R., Warner, J. C., & Hegermiller, C. A. (2021). Impact of SST and Surface Waves on Hurricane Florence (2018): A Coupled Modeling Investigation. *Weather and Forecasting*. https://doi.org/10.1175/WAF-D-20-0171.1

Zhang, C., Wang, Y., & Hamilton, K. (2011). Improved Representation of Boundary Layer Clouds over the Southeast Pacific in ARW-WRF Using a Modified Tiedtke Cumulus Parameterization Scheme*. *Monthly Weather Review*, *139*(11), 3489–3513. https://doi.org/10.1175/MWR-D-10-05091.1

Zimbo, F., Ingemi, D., & Guidi, G. (2022). The Tropical-like Cyclone “Ianos” in September 2020. Meteorology, 1(1), 29–44. https://doi.org/10.3390/meteorology1010004